From the Neuro- and Sensory Physiology Institute
at Heinrich Heine University Düsseldorf

Cardiac Electrophysiology post-Ischemia: Unmasking Arrhythmogenic Substrates by Optical Mapping

Dissertation

to obtain the academic title of Doctor of Philosophy (PhD) in Medical Sciences
from the Faculty of Medicine at Heinrich Heine University Düsseldorf

Submitted by
Seyed Erfan Moussavi Torshizi
2024

As an inaugural dissertation printed by permission of the Faculty of Medicine at Heinrich Heine University Düsseldorf

signed:
Dean: Prof. Dr. med. Nikolaj Klöcker
Examiners: Prof. Dr. med. Nikolaj Klöcker
Prof. Dr. rer. nat. Axel Gödecke

Dedication

to my wonderful wife, Bahardokht, whose unwavering support and boundless love have been the guiding light through this challenging path. Her encouragement, patience, and understanding have not only eased the difficulties but also infused joy into every step. Also, to my loving sister Arghavan whose steadfast presence in moments of triumph and challenges alike, have been a source of strength. She has been not only a sibling but also a constant source of inspiration and support on this journey of life.

List of publications

Parts of this work have been published:

Moussavi-Torshizi SE, Amin E, Klöcker N. Sex-specific repolarization heterogeneity in mouse left ventricle: Optical mapping combined with mathematical modeling predict the contribution of specific ionic currents. Physiol Rep [Internet]. 2023 Jun 1 [cited 2023 Oct 5];11(11):e15670. Available from: https://onlinelibrary.wiley.com/doi/full/10.14814/phy2.15670

Zusammenfassung

Die kardiale Ischämie birgt ein erhebliches Risiko für den plötzlichen Herztod, insbesondere durch Auslösung ventrikulärer Arrhythmien (VA). Trotz vieler Fortschritte in der kardiovaskulären Forschung bleiben zugrundeliegende ionale Mechanismen, u.a. das zeitlich-räumliche *Remodeling* der Ionenkanalfunktion in der Frühphase nach Ischämie-Reperfusionsverletzung des Herzen (I/R), weiterhin rätselhaft. Um diesen Fragen nachzugehen, wurde eine multimodale optische Kartierung am horizontalen Schnittpräparat des Mausherzen durchgeführt. Die Studie visualisierte die zeitlich-räumliche Signalausbreitung und nutzte die 2,3,5-Triphenyltetrazoliumchlorid (TTC)-Färbung sowie die in-situ-Hybridisierung, um elektrische Informationen direkt mit strukturellen Veränderungen und der Regulation der Ionenkanalexpression 24 h nach I/R-Verletzung zu korrelieren. Unter Kontrollbedingungen zeigten murine linksventrikuläre Schnitte eine gleichmäßige AP-Ausbreitung mit einem gering ausgeprägten transmuralen Repolarisationsgradienten. Nach I/R-Verletzung waren nahe der infarzierten Region Verzögerungen der frühen Repolarisation zu beobachten. Diese wurde von einer Umkehrung des transmuralen Gradienten der AP-Dauer (APD) begleitet. Die in-situ-Hybridisierung enthüllte die *de-novo*-Expression von Cacna1D in Regionen mit früher Nachdepolarisation (EADs), was auf eine Beteiligung des spannungsgesteuerten L-Typ Calciumkanals $Ca_V1.3$ an der Bildung eines arrhythmogenen Substrats hinweist.

Da das biologische Geschlecht einen Einfluss auf die Genese von VA nach Myokardischämie (MI) beim Menschen hat, untersuchte die Studie auch geschlechtsspezifische Unterschiede der kardialen Repolarisation in Mäusen. Die Ergebnisse zeigen u.a. eine längere und variablere APD im weiblichen Tier. Mathematische Modellierung deutete auf eine bedeutende Rolle von Kaliumströmen wie $I_{to,f}$ und I_{Kur} bei der AP-Verbreiterung bei weiblichem Geschlecht hin. Darüber hinaus zeigte die Reaktion auf die verstärkte Aktivierung von L-Typ-Calciumkanälen (LTCC) bei weiblichem Geschlecht einen sehr viel größeren Effekt, der möglicherweise mit der geschlechtsspezifischen Expression von I_{NaL} zusammenhängt. Schließlich wurde der Einfluss von Insulin-ähnlichem Wachstumsfaktor 1 (IGF-1), der bekanntermaßen nach einem Herzinfarkt hochreguliert wird, auf den Sinusknoten (SAN) untersucht. Bemerkenswerterweise erhöhte IGF-1 die spontane Schlagfrequenz des SAN, was auf eine regulatorische Rolle in der post-MI Kardioelektrophysiologie hinweisen könnte. Überraschenderweise induzierte der AKT-Aktivator SC79 keinen ähnlichen Effekt, was die angenommene ausschließliche Rolle des AKT-Wegs in der IGF-1-Signalgebung hinterfragt.

Zusammenfassend liefert diese Studie wichtige Einblicke in die post-I/R-Kardioelektrophysiologie, indem sie transmurale AP-Variationen, die Regulation von Ionenkanälen und geschlechtsspezifische Unterschiede aufdeckt. Sie betont die entscheidende Rolle von IGF-1 in der Kardioelektrophysiologie post-MI und unterstreicht die Notwendigkeit weiterer Forschung zur Signaltransduktion von IGF-1. Insgesamt tragen diese Erkenntnisse erheblich zum Verständnis arrhythmogener Mechanismen nach MI bei, um letztlich die Prädiktion und Prävention von VA zu verbessern.

Summary

Myocardial ischemia poses a significant risk of sudden cardiac death, particularly due to ventricular arrhythmias (VA). Despite advances in cardiac research, the underlying ionic mechanisms, especially the spatiotemporal remodeling of ion channel function in the early phase after ischemia-reperfusion (I/R) injury, remain elusive. In order to address this challenge, a multi-modal optical mapping approach was employed in transversely sectioned mouse heart slices. The study visualized spatiotemporal signal propagation through slices and used 2,3,5-Triphenyltetrazolium chloride (TTC) staining and in situ hybridization to directly relate electrical information with structural alterations and ion channel regulations 24 hours after I/R injury. Under control conditions, murine left ventricular slices displayed a uniform AP distribution with a slight transmural repolarization gradient. Post-I/R injury, an early repolarization shoulder emerged near the infarcted area, signifying a malfunction in AP repolarization. This phenomenon was accompanied by the reversal of the transmural gradient in AP duration (APD). In situ hybridization unveiled de novo expression of Cacna1D in regions presenting with early afterdepolarizations (EADs), implicating the L-type voltage-gated calcium channel CaV1.3 in the formation of an arrhythmogenic substrate.

As there is known sex-specific differences in VA susceptibility after myocardial infarction (MI) in humans, the study further explored sex-specific differences in murine cardiac repolarization, revealing longer and more variable APD in females. Mathematical modeling suggested a significant role of potassium currents such as $I_{to,f}$ and I_{Kur} in AP broadening in females. Additionally, the response to enhanced L-type calcium channel (LTCC) activation showed a more pronounced effect in females, potentially linked to sex-specific INaL expression. Moreover, driven by the documented upregulation of insulin-like growth factor 1 (IGF-1) subsequent to MI, the impact of IGF-1 on the sinoatrial node (SAN) was investigated. Notably, IGF-1 significantly increased the spontaneous beating frequency of the SAN, suggesting a regulatory role in post-MI cardiac electrophysiology. Surprisingly, the AKT activator SC79 did not induce a similar effect, challenging the assumed exclusive role of the AKT pathway in IGF-1 signaling.

In summary, this study provides critical insights into post-I/R cardiac electrophysiology, unraveling transmural AP variations, ion channel regulation, and sex-specific differences. It also highlights the crucial role of IGF-1 in post-MI cardiac electrophysiology, challenging existing assumptions and emphasizing the need for further research into its specific molecular pathways. Overall, these findings contribute significantly to understanding arrhythmogenic mechanisms in cardiac pathology, with implications for VA prediction and prevention.

List of abbreviations

ACS	Acute coronary syndrome
AF	Atrial fibrillation
AMI	Acute myocardial infarction
AP	Action potential
APD	Action potential duration
AVN	Atrioventricular node
BCL	Basic cycle length
bpm	Beats per minute
CPR	Cardiopulmonary resuscitation
CV	Conduction velocity
Cx43	Connexin43
DMSO	Dimethylsulfoxid
EAD	Early afterdepolarizations
ECG	Electrocardiogram
FFPE	Formalin-fixed paraffin-embedded
HCN4	Hyperpolarization-activated cyclic nucleotide-gated channel 4
$\mathbf{I_f}$	Funny current
$\mathbf{IF_{Na}}$	Fast-inactivated state
$\mathbf{I_{K1}}$	Inward rectifier K^+current
$\mathbf{I_{KSS}}$	Steady-state K^+ current
$\mathbf{I_{Kur}}$	Ultrarapid delayed-rectifier K^+ current
$\mathbf{I_{Na}}$	Inward Na^+ current
$\mathbf{I_{NaL}}$	Late sodium current
$\mathbf{I_{sus}}$	Sustained outward K^+ current
$\mathbf{I_{to,s}}$	Slow transient outward K^+ current
$\mathbf{I_{to,f}}$	Fast transient outward K^+ current
IGF-1	Insulin-like growth factor 1

IL-1β	Interleukin-1β
I/R	Ischemia/reperfusion
I/V	Current-voltage
k	Rate constant
LAD	Left anterior descending coronary artery
LED	Light emitting diode
LQTS	Long-QT syndrome
LTCC	L-type calcium channels
LV	Left ventricle
MMP-7	Matrix metalloproteinase-7
MI	Myocardial infarction
O_{Na}	Sodium channel open state
PBS	Phosphate buffer saline
PCI	Percutaneous coronary intervention
PCL	Pacing cycle length
PFA	Paraformaldehyde
PTM	Posttranslational modification
PVC	Premature ventricular contractions
ROS	Reactive oxygen species
RA	Right atrium
RAA	Right atrial appendage
RT	Room temperature
SAN	Sinoatrial node
SCA	Sudden cardiac arrest
SCD	Sudden cardiac death
SD	Standard deviation
SVC	Superior vena cava
TdP	Torsades de pointes
TTC	2,3,5-triphenyltetrazolium chloride

TV	Tricuspid valve
$V_{1/2}$	Voltage at half-maximum channel activation
VA	Ventricular arrhythmia
VF	Ventricular fibrillation
V_m	Membrane potential
VT	Ventricular tachycardia
WT	Wild type

List of Figures

List of tables

Table of contents

1. Introduction

1.1. Myocardial Infarction

1.1.1. Overview of MI as a major cardiovascular event

Myocardial infarction (MI), commonly known as heart attack, is a major cardiovascular event with profound implications for public health and individual well-being. It is the leading cause of death and disability worldwide and requires concerted efforts to tackle its substantial impact on global health (1). It arises from the sudden occlusion of one or more coronary arteries, leading to the disruption of blood flow to a specific region of the heart. Consequently, the affected myocardial region experiences an irreversible injury due to the deprivation of oxygen and essential nutrients, necessitating prompt medical intervention to prevent severe complications and mortality (2).

Prolonged myocardial ischemia triggers a progressive spread of cardiomyocyte death, extending from the endocardium to the epicardium, with mitochondrial alterations playing a prominent role in the apoptosis and necrosis of cardiomyocytes within the infarcted heart (Fig.1) (3).

Although encouraging reductions in the age-standardized incidence of acute MI (AMI) and prevalence of angina pectoris have been observed since the early 1990s, the growing population of aging individuals with heightened cardiovascular risk factors contributes to the escalating global burden of ischemic heart disease (4).

Fig. 1. The progressive spread of ischemic necrosis. *As the ischemic event duration increases in canine models of reperfused infarction, the necrosis of cardiomyocytes advances from the endocardium to the epicardium. The shown cardiac slice is a schematic transverse section of the canine heart, depicting the right ventricle (RV) and left ventricle (LV). The black box outlines the area at risk, and the purple shading the extent of ischemic necrosis.*

Over the past 30 years, significant progress in coronary care, early reperfusion strategies, and novel pharmacologic approaches has led to a remarkable 60 % reduction in mortality within the first 30 days after AMI. However, improved survival during the acute event has resulted in an expansion of the patient pool at risk of developing heart failure. Studies suggest a concerning rise in the incidence of post-infarction heart failure, paralleling the decline in acute mortality rates (5,6).

1.1.2. The pathophysiological mechanisms of MI

MI arises from an imbalance between oxygen supply and demand. The gradual accumulation of plaques in severe atherosclerotic disease, causing at least 75 % luminal narrowing, does not impede blood flow at rest. However, when myocardial demand increases, such as during exercise or tachyarrhythmia, the flow restriction hinders the necessary increase in oxygen supply, leading to the development of ischemia and triggering angina pectoris. The majority of AMI occur due to coronary atherosclerotic disease, which becomes further complicated by the occurrence of superimposed thrombosis (7). Thrombosis is most commonly triggered by plaque rupture, which happens when a gap forms in the fibrous cap of a vulnerable plaque, exposing the necrotic core to the bloodstream. The necrotic core is rich in thrombogenic substances, which then trigger a cascade of events that lead to the formation of a blood clot (8).

Cardiomyocytes possess high-energy phosphate reserves, sufficient to sustain contractility for a brief period of total ischemia. However, in experimental models, contractile force diminishes within 60 seconds of ischemia despite the availability of energy reserves (9). Several mechanisms collaboratively induce such immediate functional depression. Firstly, the generation of inorganic phosphate from the breakdown of creatine phosphate reserves inhibits contractile protein function (10,11). Secondly, intracellular acidosis reduces calcium binding to troponin-C, further impairing contractility (12,13). Despite preserved calcium transients and action potentials (AP) during early ischemia, the dysfunction appears to be primarily linked to the inhibition of contractile proteins. The rapid cessation of contractile function may at the same time prolong the survival of ischemic cardiomyocytes as the limited stores of high-energy phosphates are used up slowly, enabling cardiomyocytes to endure longer in the absence of perfusion (14).

Early reversible functional depression in the ischemic heart can be fully restored, if blood flow is promptly re-established within 4-5 minutes of coronary occlusion. Prolonged coronary ischemia, even without cardiomyocyte death, however, leads to extended dysfunction despite flow restoration. When function fails to recover after 10-20 minutes of occlusion, it is termed "myocardial stunning", lasting up to 24 hours post-reperfusion (15). Stunned myocardium eventually regains normal function. The pathogenesis of myocardial stunning is believed to be a result of two interconnected mechanisms: the production of reactive oxygen species (ROS) during the initial stages of reperfusion and perturbations in cardiomyocyte calcium homeostasis. ROS can lead to the oxidation of contractile proteins, which in turn delays functional recovery. Studies with ROS scavengers have demonstrated a significant reduction in post-ischemic dysfunction, providing further evidence for the involvement of ROS in the pathophysiology of myocardial stunning (16). Perturbations in calcium homeostasis can also lead to the dysfunction in stunned myocardium. Specific mechanisms involved in systolic dysfunction include reduced responsiveness of sarcomeric proteins to calcium and calcium overload-induced protease activation, which leads to the proteolysis of troponins and α-actinin (17,18). ROS may also contribute to myocardial stunning by inducing alterations in calcium homeostasis, leading to calcium overload and reduced responsiveness of sarcomeric proteins to calcium (19).

In addition to systolic dysfunction, MI also impairs diastolic function by reducing the compliance of the ventricle. This is due to the generation of metabolic byproducts, such as lactate, which create a hyperosmolar environment and lead to increased interstitial water (20). Relaxation is also an energy-requiring process, as high energy phosphates are needed to pump calcium back into the sarcoplasmic reticulum, against a concentration gradient (21). Therefore, the energetic imbalance can impair relaxation and diastolic filling.

Ischemia causes a sudden cessation of oxidative phosphorylation, which is the main source of ATP in the heart. As a result, cardiomyocytes switch to anaerobic glycolysis to generate ATP. However, anaerobic glycolysis is much less efficient than oxidative phosphorylation, causing ATP depletion, accumulation of lactate, and intracellular acidosis. All this may lead to irreversible changes in the cardiomyocytes as they are unable to maintain homeostasis without sufficient ATP (22).

In the early stages of MI, ultrastructural changes include depletion of cytoplasmic glycogen granules, distortion of the transverse tubular system, and mitochondrial swelling. If the duration of ischemia is < 15-20 minutes, these alterations are fully reversible upon restoration of coronary flow. However, longer periods of ischemia can lead to irreversible damage to the heart muscle (23). Irreversibly injured cardiomyocytes exhibit sarcolemmal disruption, perturbations of mitochondrial architecture, and necrosis. Necrosis releases danger signals, triggering an intense inflammatory reaction characterized by leukocyte infiltration into the myocardium. This inflammatory response helps remove dead cardiomyocytes and promote healing (24).

After the inflammatory phase has subsided, the proliferative phase of infarct healing begins. During this phase, fibroblasts and endothelial cells proliferate and produce new extracellular matrix. This process helps to repair the damaged heart tissue. The proliferative phase is characterized by the debridement of dead cells and matrix debris, the infiltration of activated myofibroblasts and vascular cells, and the secretion of growth factors and cytokines by reparative macrophage and lymphocyte subsets (25). The extracellular matrix is enriched by the deposition of matricellular proteins, which modulate the reparative response. Angiogenesis is also triggered to provide oxygen and nutrients to the healing infarct (26). The maturation phase follows, characterized by

cross-linking collagen (27), decreased expression of matricellular proteins, a reduced number of activated myofibroblasts (28), and inhibition of neovascularization (29). Proper regulation of these processes is essential for optimal cardiac repair and prevention of adverse remodeling after myocardial infarction (14).

1.1.3. Consequences of MI on cardiac structure and function

Depending on its severity and extent, MI may cause the shape of the ventricle to shift dramatically. The chamber may expand and take on a more spherical form, while the infarcted segments become thinner. In contrast, the surviving myocardial segments undergo hypertrophy, increasing in size. These changes are collectively termed "ventricular remodeling" (30). Ventricular remodeling exerts significant functional consequences, with chamber dilation being closely linked to the progression of systolic dysfunction, potentially leading to heart failure. Additionally, ventricular remodeling raises the risk of arrhythmias and is associated with increased mortality (31,32). Post-infarction remodeling is a multifaceted process encompassing alterations in both the infarcted and non-infarcted areas of the heart. In the non-infarcted regions, remodeling is marked by hypertrophy, fibrosis, and inflammation, with the extent of these changes influenced by the size of the infarction (33). The pathophysiology of post-infarction remodeling is not fully understood, but it is thought to be due to a combination of factors. These include the loss of functional myocardium following MI, which places an overload on the non-infarcted myocardium leading to hypertrophy and fibrosis. Additionally, defective containment and impaired negative regulation of inflammatory and fibrogenic cascades may also contribute to the remodeling process (34,35).

1.2. Introduction to Ventricular Arrhythmias

1.2.1. Heart's Rhythm and Arrhythmias: A Primer

The heart's optimal rhythm, which is vital for its proper functioning and facilitates the efficient pumping of blood throughout the entire body, relies on the coordinated electrical activity originating from a specialized group of cells called the sinoatrial node

(SAN), often referred to as the heart's natural pacemaker. The SAN generates an electrical signal that spreads through the heart's electrical system, causing the heart muscles to contract and pump blood efficiently. This process repeats with each heartbeat, maintaining a regular and coordinated rhythm (36). However, disruptions in the heart's electrical system and compromised function of the SAN can lead to conditions known as arrhythmia. These conditions may cause the heart to beat too fast (tachycardia), too slow (bradycardia), or irregularly, significantly affecting its ability to effectively pump blood.

Arrhythmias are divided into two main categories based on their location of generation. The first category is supraventricular arrhythmias, which originate in the atria, the upper chambers of the heart. These arrhythmias are caused by disruptions of the electrical signals in the atria and can lead to irregular heartbeats or rapid heart rates. On the other hand, ventricular arrhythmias (VAs) are the second category and are generated in the ventricles, the lower chambers of the heart, which will be the focus in this chapter.

1.2.2. VA and their impact on cardiovascular health

VAs, abnormal heart rhythms affecting the lower chambers of the heart known as ventricles, constitute a significant cause of morbidity and sudden death in various heart diseases (37). In Europe and North America, an alarming number of 50 to 100 sudden unexpected cardiac deaths per 100,000 population occur annually, with about half attributed to ventricular tachycardia (VT) or ventricular fibrillation (VF) (38). Despite remarkable progress in prevention, diagnostics, and treatment, cardiovascular diseases remain the leading global causes of mortality, with sudden cardiac death (SCD) accounting for approximately 10 to 20 % of all deaths (39).

VAs can lead to reduced cardiac output, disrupting the heart's normal pumping pattern and diminishing its ability to efficiently circulate blood, causing symptoms like dizziness, shortness of breath, and organ dysfunction (40,41). Furthermore, the most serious consequence of VAs is sudden cardiac arrest (SCA), particularly when it progresses to VF. During SCA, the heart's pumping function comes to a halt,

necessitating immediate cardiopulmonary resuscitation (CPR) and defibrillation to restore a normal heart rhythm (37).

Additionally, certain VAs, notably those associated with atrial fibrillation (AF), may elevate the risk of blood clots forming in the heart, which can lead to stroke if a clot dislodges and travels to the brain (42). Moreover, frequent or prolonged VAs can strain the heart muscle, potentially causing cardiomyopathy and heart failure over time (43,44). These adverse outcomes highlight the importance of understanding and managing VAs to minimize their impact on cardiovascular health and reduce the incidence of sudden cardiac death.

1.2.3. Types of VA

VAs represent a diverse array of abnormal heart rhythms, which can be classified into three pivotal groups: VF, premature ventricular contractions (PVC), and VT, which we are going to explain them in more detail:

Ventricular Fibrillation (VF):

VF is a critical and life-threatening heart rhythm disorder characterized by irregular and chaotic electrical activity within the ventricles. This abnormal electrical activity leads to ineffective and uncoordinated contractions, impairing the heart's ability to pump blood effectively. As a result, VF causes sudden cardiac arrest, requiring immediate and decisive intervention.

Traditionally, VF has been defined as turbulent cardiac electrical activity, which results in irregularities in the electrical waves responsible for ventricular excitation. During VF, the heart rate becomes too rapid, exceeding 300 excitations per minute, which prevents proper blood circulation (45). On an electrocardiogram (ECG), VF is identified by completely aperiodic and irregular beat-to-beat changes in the ventricular electrical complexes. If VF is left untreated or not promptly managed, it can lead to a severe decrease in arterial pressure, resulting in death within a few minutes due to inadequate oxygen delivery to vital organs. Thus, timely intervention is imperative to improve the chances of survival in cases of VF (42,46).

Premature Ventricular Contractions (PVC):

PVCs are abnormal heartbeats originating from the ventricles, occurring prematurely and resulting in early depolarization of the myocardium. PVCs can manifest as extra beats on an ECG and may be experienced as a skipped or fluttering sensation in the chest. They can occur in individuals with or without underlying heart disease.

PVCs are quite common and can be found even in the absence of identifiable heart disease. While they have been traditionally considered relatively benign, recent evidence has shown that they may be associated with structural heart disease, increasing the risk of sudden death. In some cases, PVCs can lead to troubling and incapacitating symptoms, such as palpitations, chest pain, presyncope, syncope, and heart failure (47,48).

It is important to note that frequent or sustained PVCs warrant further evaluation due to their potential link to more serious VAs. Over the past decade, PVC-induced cardiomyopathy has gained significant interest, highlighting the need for careful monitoring and management of PVCs (48).

Overall, PVCs represent a common form of cardiac arrhythmia, and their association with structural heart disease and the risk of more severe arrhythmias requires ongoing research and attention (47).

Ventricular Tachycardia (VT):

VT is a rapid and potentially dangerous heart rhythm originating within the ventricles. It involves repetitive, three or more consecutive premature heartbeats at a rate typically exceeding 100 beats per minute (bpm) in adults (49). VT can occur in individuals with or without structural heart disease, but it poses a higher risk in those with pre-existing cardiac conditions. There are two main types of VT: monomorphic and polymorphic.

a) Monomorphic VT: In this form, all ventricular beats on an ECG have a uniform shape and duration. It is often associated with heart disease, scar tissue from a previous heart attack, or cardiomyopathy. The key feature of monomorphic VT is the identical morphology of successive ventricular contractions, which gives it a stable and repetitive

pattern on the ECG. This regularity indicates that the VT circuit follows a fixed pathway within the ventricles.

Monomorphic VT may have various underlying causes, and they are often associated with structural heart disease, such as coronary artery disease, myocardial infarction, cardiomyopathy, or prior cardiac surgery. The presence of scar tissue in the heart due to previous injury or damage can create abnormal electrical pathways, leading to the development of monomorphic VT (37,50).

b) Polymorphic VT: This type is more unpredictable and life-threatening. Unlike monomorphic VT, where the ventricular beats have a consistent shape and duration, polymorphic VT displays varying shapes and sizes, indicating different origins of the electrical impulses (49). Polymorphic VT is commonly linked to an increased risk of progressing to VF (51,52).

One of the well-known forms of polymorphic VT is Torsades de pointes (TdP). In TdP, the QRS complexes twist around the baseline, giving it a characteristic appearance resembling a ribbon or ribbon-like pattern (53). The prolonged QT interval disrupts the normal electrical repolarization process of the heart, making it more susceptible to the development of TdP. In TdP, the heart rhythm becomes significantly irregular, resulting in QRS complexes with varying shapes and sizes. These irregularities arise from different origins of the electrical impulses within the ventricles. Consequently, TdP can give rise to various pathophysiological situations, including palpitations and syncope. In some cases, the episodes may be sustained and escalate into VF that can lead to cardiac arrest (49).

1.2.4. Cardiac arrhythmias: differences between sexes

Clinical and experimental investigations have identified sex-specific distinctions in electrocardiographic characteristics, notably concerning ventricular repolarization properties. Females typically exhibit prolonged QT intervals under baseline conditions (54,55). These differences become especially pronounced when comparing the prevalence of cardiac arrhythmias between sexes. Females are significantly more

susceptible to symptomatic Long-QT Syndrome (LQTS) and TdP than males (56,57). It is widely postulated that differences in ion channel expression and function underlie these sex-specific phenotypic variations. Nevertheless, prior studies investigating sex-related disparities in murine left ventricular ionic current expression and function have yielded conflicting results (Table 1). Key repolarizing currents, such as the fast transient outward K^+ current ($I_{to,f}$) and the ultrarapid delayed-rectifier K^+ current (I_{Kur}), have been observed to be either up-regulated, down-regulated, or unaltered in female versus male mice (58–60). Attempts to explain these inconsistencies have linked the regulation of ionic currents to fluctuations in sex hormone levels. Androgens have been shown to enhance I_{Kur} density and subsequently shorten AP duration (APD) in male mice (61). while elevated levels of estrogen may down-regulate $I_{to,f}$ and I_{Kur} densities, leading to prolonged APD in female mice (58). Furthermore, an elevated late sodium current (I_{NaL}) component in the AP may elevate the susceptibility of female mice to arrhythmias associated with LQTS (60). However, whether a heightened I_{NaL} function merely reflects a diminished repolarization reserve due to K^+ channel down-regulation remains unresolved.

Table 1 Comparison of ion channel currents and expression between female and male mice of different strains

Strain	Location	Ionic Current	Method	Age	Reference
CD1	RV/LV (Epi)	I_{Kur}(↓) $I_{to,f}$ (≈) I_{to} (≈) I_{Kss} (≈) I_{Ks} (≈) I_{K1} (≈) $I_{Ca,L}$ (≈) $I_{Na(peak)}$(≈)	isolated cardiomyocyte (patch-clamp, RNase Protection Assay)	2-3 mo	(58)
C57BL/6 H/H	LV	I_{NaL} (↑) I_{Na} (≈)	isolated cardiomyocyte (patch-clamp)	-	(62)
C57BL/6	RV	$I_{K,total}$(↓) I_{Kur} (↓) I_{Ks} (≈) I_{K1} (≈) I_{Kss} (↓)	isolated cardiomyocyte (patch-clamp, RT-PCR)	-	(63)
C57BL/6	LV	I_{kur} (↑) I_{to} (↓)	isolated cardiomyocyte (patch-clamp)	10-12 mo	(60)

C57BL/6	septum	$I_{K,total}(\downarrow)$	isolated cardiomyocyte (Patch-clamp, RT-PCR)	10 mo	(64)
C57BL6, FVB,Sv129	RV/LV (Epi,Endo)	$I_{to,f}(\approx)$ $I_{Kur}(\approx)$ $I_{Kss}(\approx)$ $I_{K1}(\approx)$	isolated cardiomyocyte (patch-clamp, Western blot)	2–3 mo	(59)
C57BL6, FVB,Sv129, CD1	septum	$I_{to,f}(\downarrow)$ $I_{to}(\downarrow)$ $I_{Kur}(\downarrow)$ $I_{Kss}(\downarrow)$ $I_{K1}(\approx)$	isolated cardiomyocyte (patch-clamp, Western blot)	2–3 mo	(59)
CD1	LV	$I_{Kur}(\downarrow)$ $I_{to,f}(\approx)$ $I_{Kss}(\approx)$	isolated cardiomyocyte (patch-clamp, Western blot)	2–3 mo	(59)

Abbreviations: $I_{K,total}$, total outward K^+ current; I_{K1}, inward rectifier K^+ current; I_{Kss}, the steady-state K^+ current; I_{Kur}, ultrarapid delayed rectifier K^+ current;I_{Na}, inward Na^+ current; I_{NaL}, late inward Na^+ current; I_{sus}, sustained outward K^+ current; $I_{to,f}$, fast transient outward K^+ current; $I_{to,s}$, slow transient outward K^+ current.

1.3. Ventricular Arrhythmogenesis Following Acute MI (AMI)

1.3.1. The Increased Risk of VA Following AMI

The risk of SCD after AMI has decreased in recent years thanks to advances in early reperfusion therapy, such as thrombolysis and primary percutaneous coronary intervention (PCI). These interventions have also reduced the incidence of sustained VT or VF occurring within 48 hours after the onset of an acute coronary syndrome (ACS) over the past decades (65,66). Although prompt revascularization and drug therapy have significantly reduced the incidence of VAs after a heart attack, about 10 % of survivors remain at high risk of SCD in the months and years following discharge from the hospital (67). This is because VAs can still occur in the early post-heart attack period, and they can be fatal. In fact, VAs account for about 50 % of all deaths in these high-risk patients (68–71).

There is a distinct temporal distribution of VAs post-AMI. The very early phase, which is up to 48–72 hours after the event, is a time of very dynamic ischemia and reperfusion.

VAs in this phase are often complex and can change quickly, making them difficult to treat. In contrast, late-stage VAs after MI, which occur from 72 hours to a few weeks up to a month post event, are often more stable and may be treated with defibrillation or ablation (68,72). This emphasizes the critical need for timely and targeted interventions to address the dynamic nature of VAs during the early post-MI phase. Approaches such as anti-arrhythmic medications and vigilant monitoring are essential components of managing these complex Vas (73). Given the rapid changes and intricate patterns observed during the early post-infarction period, healthcare providers must carefully balance the benefits and potential risks of different treatment options.

It will be essential to understand the underlying mechanisms of early VAs in order to develop effective treatment strategies. Emerging research suggests that factors such as inflammation, scar tissue formation, and electrical remodeling contribute to the instability of cardiac electrophysiology in the aftermath of AMI (74,75).

1.3.2. Contributing Factors to Arrhythmogenesis after AMI

Following an AMI, the heart experiences various challenges that play a role in the development of arrhythmias.

Ionic perturbations:

MI causes changes in the way that cardiomyocytes use energy, which lead to imbalances in specific intracellular and extracellular ion concentrations. These imbalances have a significant impact on the electrical activity of the heart and may lead to arrhythmias and other heart problems (76). Ischemia causes K^+ to leak out of the cells into the surrounding area. This buildup of K^+ in the extracellular space may weaken the heart's electrical signal, leading to a reduction in the amplitude, rate of rise, and duration of AP (77). After a period of rapid fluctuation in the initial moments of ischemia, the levels of extracellular K^+ stabilize until the point of irreversible damage caused by ischemia. As cardiac muscle cells undergo cell death, an increased amount of K^+ is discharged into the surrounding by necrotic cells (78). This shift has implications in terms of electrophysiology. Specifically, the rise in extracellular K^+ level leads to a state of

unresponsiveness and disruption in electrical conduction from an electrophysiological perspective (14).

As highlighted in the preceding section, ischemia gives rise to both intracellular and extracellular acidosis. These changes stem from heightened proton production and impaired proton removal within the ischemic region. Protonation of ion channels resulting in a reduction of the resting potential, elongation of the AP, and the emergence of early afterdepolarizations (EAD) (79).

Elevations in intracellular Na^+ are likewise detected in ischemic tissues, ascribed to a decrease in the efficiency of outward pumping mechanisms. Furthermore, there is an escalation in cytosolic calcium (Ca^{2+}) levels, which triggers the activation or modulation of numerous channels and carriers. These changes collectively contribute to the emergence of an environment conducive for arrhythmias. Additionally, the levels of free magnesium (Mg^{2+}) rise during ischemia, released from hydrolyzed ATP or from inefficient (energy-dependent) removal processes. Magnesium is recognized for its stabilizing effects on membrane excitability (e.g. by surface charge screening).

Scar formation:

After an AMI, scar tissue forms to repair the damaged heart muscle. However, scar tissue does not have the same electrical properties as healthy heart tissue, which increase the likelihood of arrhythmias (14,80).

Inflammation:

Inflammation is a natural response to injury, but it can also contribute to arrhythmias after an AMI. This impact is mediated through the activities of inflammatory cytokines and proteases, specifically interleukin-1β (IL-1β) and matrix metalloproteinase-7 (MMP-7) (81). These agents have been observed to degrade connexin43 (Cx43) in the aftermath of AMI, resulting in a reduction of conduction velocity and an elevated inclination toward arrhythmogenesis (82,83).

Structural remodeling:

Following MI, the non-infarcted myocardium undergoes adaptive hypertrophy, which may also affect the electrical activity of the heart, making it more likely to develop

arrhythmias (84). Clinical and experimental studies have shown that there is a correlation between the extent of structural post-MI remodeling and the risk of Vas (85,86). This suggests that the structural changes that occur in the heart during remodeling can have a significant impact on its electrical activity. Similar arrhythmogenic potential has been observed in models of hypertrophy that are not caused by a heart attack (87–89). This implies that the arrhythmogenic effects of remodeling are not specific to MI, but are a general consequence of structural heart disease.

1.4. Ion Channel Remodeling in the Context of AMI

1.4.1. The significance of ion channel remodeling in cardiac pathophysiology

Maintaining the synchronized and efficient contraction of the heart hinges upon the precise orchestration of cardiac electrical activity. This orchestration finds its cellular foundation in the AP, a fundamental unit that relies on the precise interplay of specialized proteins, encompassing channels and transporters. These intricate proteins regulate the controlled movement of ions across cardiac cell membranes. Perturbations caused by cardiac ailments disrupt the normal function of these ion channels and transporters, culminating in the emergence of cardiac rhythm irregularities. This phenomenon, termed 'arrhythmogenic remodeling,' entails multifaceted changes in ion channel and transporter behavior. This encompasses shifts in their expression patterns, alterations in regulatory mechanisms, and modifications in their interactions with pivotal protein partners. The implications of arrhythmogenic remodeling are profound, significantly contributing to the landscape of cardiac morbidity and mortality (90).

1.4.2. Ion channels implicated in post-MI remodeling

To gain a deeper understanding of the ion channels involved in post-MI remodeling, it is essential to initially grasp the mechanism of AP generation in cardiomyocytes and the underlying channels involved. The cardiac AP is shaped by ionic currents and

transporters. For a visual depiction and main currents during its phases, refer to Fig. 2. The phases are labeled 0 to 4, starting with initial depolarization (phase 0) and ending at the resting state (phase 4) (91). The resting cellular potential of non-nodal cardiac cells is determined by the high resting conductance of K^+. This is due to the high permeability of inward-rectifier current (I_{K1}) channels during resting phase. The significant I_{K1} conductance maintains the resting potential of non-nodal cardiac muscle cells near the equilibrium potential of K^+, which is approximately -80 to -90 mV. Upon activation, cells undergo depolarization due to the rapid influx of Na^+ through voltage-gated Na^+ channels, generating a large inward-flowing (depolarizing) Na^+ current (I_{Na}). After a brief and rapid phase of repolarization (phase 1) due to the exit of K^+ mediated by a rapidly activating and inactivating channels responsible for transient outward current (I_{to}), cardiac cells transition into a plateau phase (phase 2). During this phase, a balance is achieved between inward currents (primarily L-type Ca^{2+} current, I_{CaL}) and outward K^+ currents. Throughout this phase, there is a gradual increase in delayed-rectifier currents, notably the rapid delayed-rectifier I_{Kr}. These currents combined with Ca^{2+}-dependent inactivation of $I_{Ca,L}$ ultimately conclude the AP by inducing rapid phase 3 repolarization, introducing a suitable delay (90).

Following the onset of MI, a spectrum of K^+ currents, including I_{K1} (92), I_{to} (93), I_{Kr}, and I_{Ks} (94), experiences downregulation within the border-zone and normal zone, which contributes to an increase in APD of the cells (95). This prolongation of APD can cause EAD and related arrhythmias. the L-type calcium current (I_{CaL}) also exhibits a reduction in amplitude, slowed recovery rate (96) and hyperpolarizing shifts in inactivation voltage dependence (97). Moreover, The surviving tissue displays diminished phase 0 amplitude

and upstroke velocity (dV/dt_{max}), indicating a reduction in $I_{Na.}$(98) These irregularities in excitability promote the occurrence of one-way blockage and re-entry (99).

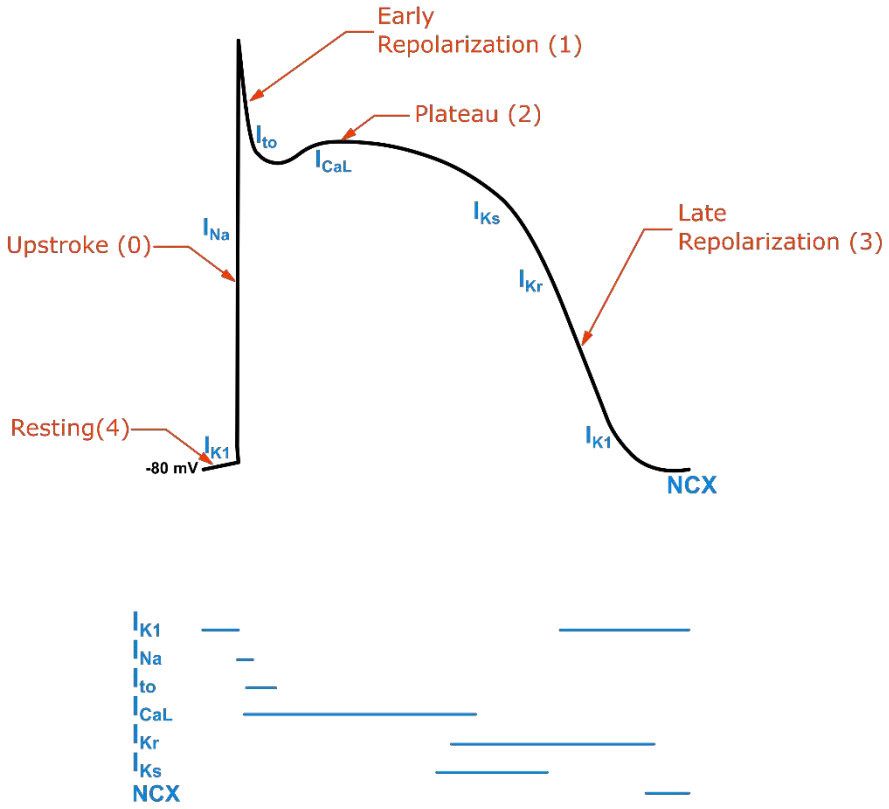

Fig. 2. Schematic representation of the cardiac AP and the principal corresponding ionic currents. *The horizontal lines at the bottom serve as a schematic depiction of the intervals during which each current flows within the AP. Notation included: I_{K1}, inward rectifier K^+ current; I_{Ks}, slow delayed-rectifier current; I_{Kr}, rapid delayed-rectifier current; I_{CaL},L-type Ca^{2+} current I_{Na}, inward Na^+ current; I_{to}, transient outward K^+ current; NCX, Na^+-Ca^{2+} exchanger.*

L-type calcium channels (LTCCs), which are abundant cardiac ion channels, are primarily dominated by two main α-subunits in the heart: $Ca_V1.2$ and $Ca_V1.3$. During early embryonic development, $Ca_V1.3$ is prevalent contributing to automaticity. As development progresses, $Ca_V1.2$ becomes the primary isoform in ventricular myocytes, while $Ca_V1.3$ remains restricted to myocytes in the SAN and atrioventricular node (AVN) (100). Genetic studies have highlighted the role of $Ca_V1.3$ in generating cardiac pacemaker activity, specifically by influencing diastolic depolarization in SANs

pacemaker cells (101). Based on proteomic analysis conducted on both wild-type (WT) and ischemia/reperfusion (I/R) mice, it was observed that the re-expression of $Ca_V1.3$ occurred within one day following MI (102). However, its effect on the electrical activity of the heart and potential arrhythmogenesis is yet unclear.

1.4.3. Insulin-like growth factor 1 (IGF-1) and Posttranslational Modifications (PTMs)

After a MI event, alongside the regulation of ion channels at the transcriptional and translational levels, PTMs also emerge as a crucial layer of control, governing the activity and function of various proteins involved in cardiac health (103). They can rapidly and specifically alter protein function, which is essential for the heart to respond to changes in its environment. PTMs encompass a range of processes, such as phosphorylation, glycosylation, acetylation, and ubiquitination. These modifications can modulate protein structure, interactions, stability, and activity (104). In the context of MI, PTMs play a pivotal role in shaping the heart's response to ischemic injury and its efforts to recover. For example, the phosphorylation state of Ca^{2+} handling proteins, such as phospholamban, is altered after MI, which can contribute to SERCA2a dysfunction and arrhythmias (105). Additionally, due to enhanced oxidative stress following infarction the function of ion channels, such as I_{to} (106) and I_{Na} (107), are also affected. The increased phosphorylation of I_{to} channels can lead to a decrease in I_{to} current, which may contribute to arrhythmias (106).

Another example of PTM in context of MI is modifications induced by IGF-1, a soluble protein of 7.6 kDa and a structural composition comprising 70 amino acid residues (108). Functionally, IGF-1 assumes a pivotal role in the regulation of fundamental cellular processes encompassing proliferation, differentiation, metabolism, and cellular survival (109). Particularly, In the context of cardiac physiology, IGF-1 is known to regulate a great variety of cellular processes including metabolism, apoptosis, autophagy, aging, and growth (110–112). As previously stated, MI induced hypertrophic changes in unaffected tissues. Interestingly, research has demonstrated an increase in IGF-1 levels within hypertrophic tissue (113). Furthermore, as reported by Reiss et al., IGF-1

expression increases in unaffected myocytes of the LV starting 12 hours after infarction, and this elevation persisted for several days.(114) Conversely, existing data emphasize the critical function of IGF-1 in maintaining the normal rhythm of the SAN through its interaction with Hyperpolarization-activated Cyclic Nucleotide-gated channel 4 (HCN4) (115). The latter is mainly responsible for the "funny" (I_f) pacemaker current. Nevertheless, the precise consequences of elevated IGF-1 concentrations resulting from hypertrophy on a potential development of tachycardia or even arrhythmias remain to be elucidated. Moreover, the I_f current is not solely confined to the SAN; in fact, many researchers have proposed an upregulation of HCN channels in hypertrophied ventricles (116–118). According to Hoffman et al., the increased I_f current in hypertrophied myocytes may lead to the extension of the repolarization phase of the ventricular AP and thereby enhance the arrhythmogenic potential (119). Apart from HCN regulation by IGF-1, phosphoproteomics data by Reinartz et al. indicate that AKT activation leads to the phosphorylation of numerous ion channels in HL-1 cells, a cardiac cell model (120). Considering that AKT is a downstream protein in the IGF-1 cascade, (109) it is plausible that elevated levels of IGF-1 could exert regulatory influence over multiple ion channels and proteins responsible for cellular electrical activity, including HCN4, $Ca_V1.3$, and RYR2.

1.4.4. Clinical implications of understanding ion channel remodeling in post-AMI arrhythmogenesis

The emerging understanding of ion channel remodeling in post-AMI arrhythmogenesis holds promising clinical implications. As awareness regarding the significance of ionic current and transporter remodeling in the development of arrhythmic and functional complications associated with cardiac diseases continues to rise, there is a growing interest in utilizing remodeling as a potential therapeutic target. However, it is worth noting that compared to extensively studied conditions like AF and heart failure, there remains a significant gap in research regarding interventions targeting ion-handling processes post-MI. Notable examples include imidapril, an ACE inhibitor, which has shown promise in reducing refractoriness heterogeneity and preventing EAD in unaffected areas of rabbits heart with prior MI (121) as well as

Carvedilol, a combined α1- and β-adrenoceptor antagonist, which effectively counteracted the downregulation of both I_{Na} and I_{CaL} currents post-MI (122,123).

This highlights an opportunity for further investigation and underscores the potential benefits of exploring therapeutic strategies aimed at mitigating ion channel remodeling in post-AMI patients. Such efforts hold the promise of improving the clinical management of these individuals and reducing the incidence of arrhythmias and related complications.

1.5. Aims of the thesis

The central objective of this thesis is to address the existing gaps in our comprehension of the molecular mechanisms underlying VAs subsequent to AMI. In the context of the persisting medical challenge in risk stratification and the absence of evidence-based pharmacological interventions for preventing or treating VAs post-acute MI, the research is framed. The driving hypothesis assumes that alterations in cardiac ion channel and transporter function contribute to abnormal cellular excitability and impulse propagation during the initial days following ischemic injury. To investigate this hypothesis, the thesis focuses on exploring the impact of I/R injury on transmural AP heterogeneity within the LV of adult mice. Traditional research in this field primarily employed models of dissociated cardiomyocytes, which, while valuable for single-cell electrophysiology and molecular analysis, have limitations related to cell isolation, potentially leading to the loss of regional cell origin and disruption of important extracellular components.

To overcome these limitations, the present study employs a high-resolution optical mapping approach in acute slice preparations to accurately visualize transmembrane voltage patterns. This method allows for a precise locoregional analysis of AP features within thin slices of murine ventricular tissue. The primary aim of the research is to investigate the APD and its potential regional intra- and inter-individual variability within the LV of adult mice. This exploration encompasses baseline conditions and, importantly, the response to pharmacological calcium channel activation, simulating a cardiac stress factor. Additionally, the research endeavors to utilize mathematical modeling to estimate the contributions of specific ionic currents to the overall morphology of the AP. This multi-faceted approach is designed to provide a comprehensive understanding of the underlying electrophysiological mechanisms associated with the hypothesis of transmural AP heterogeneity resulting from I/R injury.

The second phase of this research delves into sex-specific repolarization differences within the mouse left ventricle, building upon consistent findings from clinical and experimental studies that highlight varying electrocardiographic patterns between sexes. Notably, women have a higher risk of symptomatic LQTS and TdP tachycardia compared to men, emphasizing the importance of understanding ventricular

repolarization. Amid variations in ion channel expression and function reported in murine left ventricular ionic currents, this study aims to address these differences. The exploration focuses on the regional variability of APD in the LV of adult male and female mice. As discussed earlier, the optical mapping approach serves as a departure from traditional models, providing a means to visualize voltage changes in thin slices of murine ventricular tissue and offering detailed insights into AP features. The investigation spans baseline conditions and responses to pharmacological calcium channel activation, effectively simulating cardiac stress. Augmented by mathematical modeling, the research seeks to understand the contribution of specific ionic currents to AP morphology, thereby shedding light on the nuanced dynamics of sex-specific repolarization in the murine heart. Consequently, this research endeavor is poised to significantly advance our understanding of cardiac electrophysiology, with the potential to inform future therapeutic interventions.

In the third phase, this research aims to unravel the intricate regulatory mechanisms governing cardiac electrophysiology following MI. Specifically, the study seeks to explore the effects of IGF-1 on HCN4 within the SAN and assess the influence of SC79, an AKT activator, on the SAN firing rate. The investigation aims to provide mechanistic insights into how IGF-1 dynamically modulates cardiac activity, focusing on its potential impact on SAN spontaneous beating frequency post-MI. Additionally, by comparing the effects of IGF-1 and SC79, the study aims to delineate the role of the AKT pathway in mediating these responses. This research endeavor contributes to a comprehensive understanding of post-MI cardiac electrophysiology dynamics, with implications for potential therapeutic interventions targeting the IGF-1 and AKT signaling pathways.

In summary, this thesis aims to provide comprehensive insights into cardiac electrophysiological changes post-MI, uncover sex-specific variations in repolarization, and investigate the modulation of HCN4 channels by IGF-1 in the context of cardiac function. These findings may contribute to advancements in cardiovascular research and potential therapeutic strategies.

2. Materials and methods

2.1. Animals

All animal experimentation procedures in this study adhere to the relevant European Union directive 2010/63/EU concerning the ethical treatment of animals employed in scientific research. The research protocols received official approval from both the local animal care and use committee at the University of Düsseldorf (Reference Number: O7/11 and G204/19) and the Animal Ethics Committee of the State Agency for Nature, Environment, and Consumer Protection in North Rhine-Westphalia, Düsseldorf (Approval Numbers: 81-02.04.2019.A204).

Unless explicitly specified otherwise, adult male and female C57BL/6J mice (weighing 20 – 30 g; sourced from Janvier Labs, Le Genest-Saint-Isle, France) were accommodated in a controlled environment with a 12/12-hour light/dark cycle and provided with unrestricted access to both water and standard chow diet.

2.2. Mouse model of I/R

The I/R procedure was performed by Dr. Andre Heinen (Institute of Cardiovascular Physiology, Medical Faculty and University Hospital Düsseldorf), following established protocols (124).

In brief, the surgical procedure involved a left thoracotomy, which was performed on anesthetized mice using a combination of 2% isoflurane and 0.1 mg/kg body weight buprenorphine. The mice were mechanically ventilated to ensure proper oxygenation throughout the procedure. The objective of the surgery was to enable access to the left anterior descending coronary artery (LAD) for occlusion.

To achieve LAD occlusion, a 7-0 prolene thread was carefully placed around the vessel. Body temperature was meticulously maintained at 37.5 ± 0.5°C to ensure physiological stability during the entire procedure. The successful occlusion of the coronary artery was confirmed by monitoring for ST-elevation in the recorded ECG using

equipment from ADInstruments, based in Castle Hill, Australia. Additionally, visual confirmation was obtained through the observation of blanching in the area at risk.

Following a 45-minute period of ischemia, the reperfusion phase was initiated by delicately reopening the LAD. To manage postoperative pain and ensure the well-being of the mice, buprenorphine (0.1 mg/kg body weight, subcutaneous; administered every eight hours) was employed for analgesia. In sham group the period of ischemia was skipped.

After a recovery period of 24 hours, humane euthanasia was performed by cervical dislocation under sedation with 2.5% (v/v) isoflurane. Subsequently, the hearts were carefully excised for further analysis.

2.3. Optical mapping

2.3.1. Tissue slice preparation

Prior to heart harvesting, the procedure was initiated by administering an intraperitoneal injection of heparin at a dosage of 300 IU/kg to the mice, thus achieving effective anticoagulation. After a 15-minutes interval following the administration of heparin, the animals were gently sedated by inhalation of 2.5% (v/v) isoflurane and subsequently euthanized via cervical dislocation.

The cardiac tissues were rapidly excised and submerged into ice-cold, oxygenated extracellular solution buffered with bicarbonate, providing essential nutrition.

Following the tissue excision, retrograde perfusion of the aorta using the same solution was initiated. This process was managed through a peristaltic pump, which regulated a consistent flow rate of 1.5 mL/min. Importantly, this initial perfusion step, maintained for a minimum of 3 minutes, was pivotal to ensure the isolated cardiac tissues resumed rhythmic contractions.

Subsequently, a seamless transition to a modified perfusion medium was made for staining the tissue with fluorescent dyes. This new medium, enriched with Di-8-ANEPPS at a concentration of 3µM, facilitated the dye-loading process. The duration of this

phase extended for 4 minutes. Following successful dye-loading, the cardiac tissues were subjected to a continuous perfusion with a same solution containing 10 µM (-)-blebbistatin. This continued until cardiac contractions ceased, a typical process spanning approximately 5 minutes.

Following precise dissection, which involved the removal of atrial tissue and major vessels, the ventricles were embedded in 4 % low-melt agarose. This was accomplished by dissolving the agarose in PBS, while maintaining a temperature of 37°C. Rapid cooling ensured complete solidification of the agarose blocks. Subsequently, the agarose-embedded ventricles were securely affixed to a specimen holder using tissue adhesive histoacryl. Transversal sectioning was then conducted, resulting in slices at 350 µm in thickness. This sectioning procedure was executed using a vibratome (LEICA VT1200S) equipped with steel blades, operated at a progression speed of 0.03 mm/s and a lateral blade vibration amplitude of 2 mm (125). Throughout this sectioning process, the tissues remained immersed in an ice-cold, bicarbonate-buffered extracellular solution, supplemented with 10 µM (-)-blebbistatin.

Immediately post-sectioning, each slice was carefully transferred into a custom-made circulation chamber filled with bicarbonate-buffered solution containing 10 µM (-)-blebbistatin. To ensure a controlled thermal environment, a glass spiral was incorporated before the chamber entrance and the solution flow rate was regulated to 6 ml/ min to maintain a stable temperature of 35 °C.

The stimulation of cardiac slices was achieved by utilizing a unipolar platinum-iridium electrode (ThermoFisher), connected to an electrical stimulator (STG4002, Multi Channel Systems MCS GmbH). The stimulation parameters included a cycle length of 200 ms, a pulse width of 1 ms, and a strength set at 1.5 times the threshold, which typically ranged from 3 to 5 V. To attain a state of electrophysiological stability, the cardiac slices were subjected to continuous pacing for a minimum of 30 minutes. During this duration, the signal-to-noise ratio of fluorescence intensity consistently increased, ultimately reaching a stable state.

In alignment with the objectives of this study, short-axis slices were selected for analysis. These slices were systematically chosen from the middle one-third of the heart

to ensure that the observations were controlled for potential AP heterogeneity along the longitudinal axis, spanning from the base to the apex.

2.3.2. Atrial isolation and SAN exposing preparation

To conduct optical mapping of the SAN and expose this critical cardiac structure, a series of surgical steps were executed (126). First, the atria were carefully isolated from the heart, providing the initial access to the SAN region. Subsequently, the ventricles were dissected away from the anterior aspect of the atrial preparation, ensuring that it would not interfere with the subsequent steps.

Following the ventricular dissection, a precise incision was made along the tricuspid valve (TV) following the TV-Superior Vena Cava (SVC) axis. This particular incision allowed for the precise opening of the right atrium (RA), offering a clear pathway to the SAN region.

To gain further access to the SAN, a cut was made along the medial limb of the crista terminalis, which revealed the right atrial appendage (RAA). Finally, by performing a cut along the anterior atrial free wall, extending from the midpoint of the RAA to the right bottom corner of the RAA, the RA was flattened. This step resulted in the effective exposure of the SAN, setting the stage for subsequent optical mapping and research procedures.

Following the exposure of the SAN, the specimen was transferred to a custom-made circulation chamber containing a bicarbonate-buffered extracellular solution supplemented with 10 µM (-)-blebbistatin, similar to the setup used for heart slices. The specimen was held flat within the chamber using 0.1 mm pins, for minimizing speciment movement and ensuring optimal conditions for data collection.

2.3.3. Optical data recording

For the purpose of exciting fluorescent dyes, a light emitting diode (LED) light source (LEX3-G; 525 nm; SciMedia/Brainvision) was employed, which was seamlessly integrated with a THT Macroscope (SciMedia/Brainvision) to ensure precise optical

control and imaging. To isolate the excitation light, it was passed through a dedicated excitation filter (BP531 nm/40) and subsequently directed by a dichroic mirror (580-FDI) toward the perfusion chamber, where it was accurately focused onto the tissue slice under examination.

The fluorescent signals emanating from the tissue slice were diligently collected using a high-quality 1.0X objective lens (LEICA) and then subjected to precise filtration using a long-pass filter (LP600 nm) to selectively capture the desired fluorescence. The filtered fluorescent emissions were systematically recorded with the assistance of the MiCAM05-N256 imaging system (SciMedia/Brainvision), which featured a high-performance CMOS image sensor with mapping field area equal to 10 × 10 mm (256 × 256 pixels) and a frame rate of 1 kHz.

The entire optical recording process was controlled by the BV Workbench software (Brainvision). The captured data were then formatted and stored in accordance with the requirements of subsequent customized MATLAB analysis.

2.3.4. Drug application

To comprehensively investigate the impact of various metabolites, such as FPL64176 or IGF-1, on the experimental models, these metabolites were introduced directly into the circulating extracellular solution. This strategic addition allowed for the controlled and precise exposure of the cardiac tissues to the metabolites of interest.

2.3.5. Analysis of optical data

Data processing, analysis, and visualization were skillfully executed through the utilization of custom MATLAB scripts, thoughtfully crafted by Dr. Ehsan Amin. These comprehensive suite of MATLAB scripts played a pivotal role in enhancing the accuracy and interpretability of the results.

The processing of optical data involved several essential steps to ensure the reliability of the findings. First and foremost, ensemble averaging was applied to minimize noise

and enhance the signal-to-noise ratio. To further enhance data quality, drift correction was carried out using polynomial fitting techniques. Additionally, spatial mean filters, with a dimension of 3 × 3 pixels, were judiciously employed to reduce spatial artifacts.

The data processing methodology drew inspiration from the RHYTHM source code developed by Gloschat et al. in 2018 (127). This source code served as a valuable reference, guiding the approach to effectively process and analyze optical data.

The electrophysiological characteristics of the cardiac tissue were explored by focusing on the extraction of key parameters, including activation times and APD at distinct repolarization percentages, such as APD_{30}, APD_{50}, APD_{80}, and APD_{90}. In this pursuit, the "findpeaks" function was adjusted to accurately identify local maxima and measure widths at various peak amplitude levels, ensuring the precision of the APD calculations.

To effectively present findings, the capabilities of the vector drawing program Inkscape were harnessed. This versatile tool allowed us to arrange, refine, and enhance the visual representation of MATLAB-generated plots and maps, ensuring that the data was not only rigorously analyzed but also presented in a clear and insightful manner (128).

2.4. Histology

2.4.1. TTC staining

To evaluate the infarct size and location, heart slices underwent incubation in a solution containing 2 % (w/v) TTC, which was thoroughly dissolved in PBS. This incubation process was carried out over a 30-minutes period at a temperature of 37 °C. Subsequently, the heart slices were carefully positioned and affixed onto coverslips for further examination. TTC, known for its ability to permeate cell membranes and interact with intracellular dehydrogenases, played a crucial role in this assessment. Within the cardiac tissue, viable cells that retained their reducing potential, signifying preserved NADPH levels, displayed a distinctive brick-red coloration. Conversely, non-viable cells, characterized by ruptured sarcolemmal membranes and enzyme washout, appeared

pale in contrast. Within the tissue, the infarcted regions manifested as discernible TTC-negative zones, serving as a distinctive marker for the extent of myocardial damage (129).

2.4.2. Paraffin-Embedding

To achieve the precise slicing of cardiac tissues to a thickness of 10 µm or less, a specific tissue preparation protocol was followed. Initially, freshly obtained hearts were cannulated and thoroughly washed with a cold PBS solution at 4 °C to remove any residual blood. Subsequently, the hearts were immersed in formalin for a 24 hours fixation period.

Following fixation, the tissue dehydration process commenced, which involved sequential immersion in ethanol solutions with increasing concentrations. This entailed a 2-hour incubation in 70 % ethanol, followed by 1 hour in 80 % ethanol, another 1 hour in 90 % ethanol, and finally, a 12-hour immersion in 100 % ethanol.

The next step involved the transfer of tissue sections through a series of two consecutive pure Roticlear baths, each lasting 90 minutes, to ensure optimal clarity. Subsequently, the tissue sections underwent two 45 minutes rounds of embedding in 60°C paraffin wax for paraffin infiltration. Ultimately, the cardiac tissues were securely placed in a metallic embedding mold filled with 60 °C paraffin and left at room temperature (RT) until the mold could be easily removed, facilitating the subsequent precision cutting process to achieve the desired 10 µm thickness for analysis.

In the preparation of paraffin-embedded specimens for sectioning, the paraffin block, housing the specimen, was initially subjected to a cooling process on ice to enhance its structural rigidity. Subsequently, the block was affixed to a rotary microtome (leica) and sections were cut at a thickness of 10 µm, ensuring a clearance angle of 5 degrees to optimize sectioning quality. Following the cutting process, these sections were gently floated on a bath of distilled water maintained at 40 °C to achieve a flattened state. Next, the sections were picked up by Superfrost ultra plus microscope slides (J3800AMNZ,Thermoscientific) from water and stored in an upright position within a

slide rack. The slide rack was then placed in an oven at 42 °C overnight, allowing for further stabilization and preservation of the sections before final storage at RT.

2.4.3. Chromogenic *in situ* hybridization

Chromogenic *in-situ* hybridization was performed using slices that had been cut to a thickness of 150 µm using the same setup vibratome. These slices were obtained consecutively to the ones employed for optical mapping. Upon their retrieval, a critical step was initiated to preserve the molecular content of the tissue.

To achieve this, the slices were promptly subjected to fixation using a 4 % PFA solution dissolved in PBS at a pH of 7.4. This fixation process, executed for a duration of 15 minutes, adhered meticulously to the manufacturer's established protocols. Specifically, the guidelines outlined in Advanced Cell Diagnostics' HD2.5 brown RNAScope kits were followed (130). In a sequential procedure, after the sections underwent fixation, they were subjected to a series of meticulous steps. Initially, they were thoroughly washed twice in PBS. Following this, a dehydration phase was initiated, involving sequential incubation in 50 %, 70 %, and ultimately 100 % ethanol, with each step lasting 5 minutes at RT.

Subsequently, the sections were treated with 4 drops of hydrogen peroxide for a duration of 10 minutes at RT, followed by a single rinse with PBS. The next phase involved the application of 4 drops of Protease IV, with an incubation period of 30 minutes at RT. The sections were then subjected to extensive washing in PBS.

Moving forward, the hybridization phase was executed, during which the sections were exposed to CACNA1C or CACNA1D probes and incubated for 2 hours at 40 °C. Post-hybridization, thorough washing in the provided washing buffer was performed as specified in the kit's instructions.

The subsequent steps encompassed the hybridization of the sections with AMP1 (30 minutes at 40 °C), AMP2 (15 minutes at 40 °C), AMP3 (30 minutes at 40 °C), AMP4 (15 minutes at 40 °C), AMP5 (1 hour at RT), and AMP6 (15 minutes at RT). Between each AMP application, diligent washing using the provided washing buffer was carried out.

To culminate the process, equal parts of DAB-A and DAB-B were mixed, and 120 µl of this DAB mixture was applied to each section. This final step involved an incubation period of 10 minutes, ultimately revealing the desired staining patterns and enabling further molecular analysis.

Following the comprehensive chromogenic *in situ* hybridization procedure outlined above, the sections were mounted carefully onto coverslips. This was achieved by placing the slices onto coverslips using Prolong™ Gold Antifade Mountant. This final step ensured the preservation of the staining patterns and enabled long-term storage, facilitating subsequent analyses and observations. Subsequently, images of the stained sections were acquired using a Zeiss Observer.Z1 microscope (Carl Zeiss), allowing for detailed examination and analysis of the molecular patterns within the tissue.

2.4.4. Multiplex fluorescence RNAscope

To investigate the concurrent labeling of two or three targets, the Multiplex Fluorescence RNAscope Kit V2 was employed on formalin-fixed paraffin-embedded (FFPE) tissue sections with a thickness of 10 µm. This protocol adhered to the guidelines provided in the user manual for Advanced Cell Diagnostics' RNAScope Multiplex Fluorescent Reagent Kit v2 (Document Number 323100-USM).

The initial step in the RNAscope procedure for FFPE tissue sections involves deparaffinization. To accomplish this, the sections were subjected to two consecutive 5-minute incubations at RT in xylene, each with agitation. Subsequently, they underwent two 2-minute incubations in 100% ethanol. Finally, the sections were placed face-up on absorbent paper and allowed to air dry completely.

In the next step, each section was treated with 400 µl of hydrogen peroxide and incubated for 10 minutes at RT. Afterwards, the sections were rinsed with distilled water. Following this, the slides were immersed in a target retrieval solution at 90 °C for 15 minutes, and then quickly air-dried for 15 seconds before being transferred to 100 % ethanol for a 3-minute duration. The sections were allowed to air dry for an additional 5 minutes at 60 °C.

To prepare the sections for fluorescent assay, 400 µl of protease plus solution was evenly applied to cover each section, and they were incubated for 40 minutes at 40 °C.

In the fluorescent assay segment, the initial phase involves the hybridization of probes. To accomplish this, a 500 µl mixture of probes was prepared, comprising Cacna1c-C1, Cacna1d-C3, and Trpn2-C2 in a ratio of 50:1:1. This probe mixture was applied to each section, and the sections were then incubated for a duration of 2 hours at 40°C. Subsequently, the sections underwent a double wash in washing buffer.

The next steps of the assay involved a series of hybridization processes, involving AMP1 (30 minutes at 40 °C), AMP2 (30 minutes at 40 °C), and AMP3 (15 minutes at 40 °C). Following the application of each amplification step, thorough washing was performed utilizing the washing buffer.

Following the hybridization of the probes with AMPs, the next steps involved the development of HRP-Cs. To achieve this, each section was initially coated with 400 µl of HRP-C1 and incubated for 15 minutes at 40 °C. Subsequently, 70 µl of Cy3, serving as a fluorescent dye, was introduced, and the sections were incubated for an additional 30 minutes at 40 °C. Finally, 400 µl of HRP blocker was applied to the sections and incubated for an additional 10 minutes. This entire process was repeated for HRP-C2 and HRP-C3, with the exception of utilizing different fluorescent dyes (C3-Cy5 and C2-Fluorescein).

To stain the cell nuclei, 200 µl of DAPI was added to each slide and incubated for 30 s at RT. Any excess liquid was carefully removed by gentle tapping, and a coverslip was placed on each section using ProlongTM Gold Antifade Mountant. The sections were then evaluated using an Observer.Z1 microscope.

2.5. Mathematical modeling

Utilizing a dynamic mathematical model of mouse ventricular AP as the foundation, simulations with parameters tailored to physiological temperatures (accessible archived code in CellML) were conducted (131). This comprehensive model encompassed membrane ionic channel currents, ionic pumps, and exchangers, all while considering the intricate processes that regulate intracellular ion concentrations of Na^+, K^+, and Ca^{2+}.

The translation of these model formulations into MATLAB was followed by the application of the ODE15s differential equation solver, a crucial step to maintain strict adherence to conservation principles.

Notably, a significant enhancement involved the replacement of the Na^+/K^+ ATPase with a thermodynamically consistent model, which played a pivotal role in ensuring the stability of internal Na^+ and K^+ ion concentrations, particularly in pathophysiological scenarios (132). Additionally, the formulation of inwardly rectifying K^+ currents (I_{K1}) was updated based on the latest research findings (133).

Furthermore, a seven-state Markovian model, factoring in both voltage- and Ca^{2+}-dependent inactivation, was employed to model the $Ca_V1.3$ channel, facilitating the development of the $Ca_V1.3$ channel model (134). Adjustments to the voltage-dependent activation and inactivation rate constants were made in line with experimental data from SAN myocytes (101).

Moreover, an essential modification involved the introduction of an exponential term into the model, enabling the calculation of the percentage ratios between $Ca_V1.2$ and $Ca_V1.3$ as total LTCC currents. These extensive refinements and adaptations to the model were instrumental in accurately simulating and comprehending the intricate dynamics of ventricular APs.

2.6. Statistical analysis

Statistical analyses were carried out using MATLAB, employing either the Student's t-test (paired or unpaired) for pairwise comparisons or two-way ANOVA for multi-group comparisons. Data presentation followed a format of mean ± standard deviation (SD) to provide a concise summary of the data distribution. In the context of statistical significance, p-values less than 0.05 were considered indicative of noteworthy differences between means. Specifically, significance levels were denoted as follows: * for $p < 0.05$, ** for $p < 0.01$,*** for $p < 0.001$ and **** for $p < 0.0001$.

It is important to note that throughout the entire study, the variable 'n' consistently referred to the number of hearts examined as replicates. This ensured transparency and consistency in reporting the experimental sample sizes.

2.7. Materials and solutions

2.7.1. Optical Mappings stocks

The purchase information for all materials utilized in my experiments has been documented in Table 2.

Table 2 Materials purchase information

Material	company	Product Number	Storage Tempreture (°C)
Di-8-ANEPPS	ThermoFisher Scientific	D3167	4
SC-79	Merck	123871	-20
(-)-blebbistatin	Selleckchem	S7099	4
Pluronic™ F-127	ThermoFisher Scientific	P3000MP	RT
Dimethylsulfoxid (DMSO)	ThermoFisher Scientific	D12345	RT
FPL 64176	Merck	F131	4
Human IGF-1	Macs Miltenyi Biotec	130-093-887	-20
Distilled water	Ampuwa	1080181	RT
NaCl	Roth	3957.1	RT
$CaCl_2$	Roth	5239.1	RT
Glucose	Roth	HN06.3	RT

KCl	Merck	1.049.361.000	RT
$MgCl_2 \cdot 6H_2O$	Roth	HN03.2	RT
NaH_2PO_4	Roth	P030.1	RT
$NaHCO_3$	Roth	HN01.1	RT
HEPES	Roth	HN77.3	RT
Isoflurane	harvard apparatus	34-1041	RT
Heparine-Natrium 5000 I.E/ml	BBraun	1708.00.00	RT
Phosphate buffer saline (PBS)	Gibco	14190094	RT
low-melt agarose	Carl Roth	6351.2	RT
tissue adhesive histoacryl	BBraun	175182	RT
Paraformaldehyde (PFA)	Sigma	441244	RT
2,3,5-triphenyltetrazolium chloride (TTC)	Merck	T8877	RT
RNAscope™ 2.5 HD Assay - BROWN	ACDBio	322300 /322310	4
RNAscope™ Multiplex Fluorescent Kit v2	ACDBio	323100 /323110	4
Prolong™ Gold Antifade Mountant	ThermoFisher Scientific	P36930	RT
Roticlear	Roth	A538.1	RT

The optical mapping dyes and medications were either solubilized in DMSO or in a solution containing pluronic™ F-127, depending on their individual solubility characteristics. Table 3 contains the detailed information regarding the specific solvents, corresponding solute concentrations and the storage concentration for each solute.

Table 3 stock conditions for dyes and drugs

Solute	solvent	Concentration (mM)	Storage Tempreture (°C)
Di-8-ANEPPS	DMSO	2.2	4
SC-79	DMSO	50	-20
(-)-blebbistatin	DMSO	6.8	4
FPL	DMSO	3	4
IGF-1	PBS	0.129	-20

2.7.2. Bicarbonate-buffered extracellular solution

A bicarbonate-buffered extracellular solution was created by following a precise procedure. The necessary materials from Table 4 were dissolved in distilled water. Subsequently, the solution was gently warmed to 37°C. The desired pH level of 7.4 was carefully adjusted using 5M NaOH. Finally, the solution was passed through a 0.2 µM Nalgene™ Rapid-Flow filter.

Table 4 Composition of Solutes in Bicarbonate-Buffered Extracellular Solution

Solute	Concentration (mM)
NaCl	123
$CaCl_2$	1.8
glucose	10
KCl	5.4
$MgCl_2$	1.2
NaH_2PO_4	1.4
$NaHCO_3$	24

3. Results

3.1. Unveiling the Significance of $Ca_V1.3$ Ion Channel Remodeling after MI

3.1.1. Multifaceted heterogeneity in the vicinity of acute I/R injury

In an effort to establish a correlation between the structural and functional aspects of the mouse myocardium following acute I/R injury, an optical mapping technique was employed, as detailed in Fig. 3. Following the introduction of Di-8-ANEPPS through *ex vivo* Langendorff perfusion for optical mapping, the subsequent step involved the assessment of short-axis tissue slices with regard to membrane voltage. Recordings were conducted at an exceptionally high spatial resolution, utilizing a grid of 256 x 256 pixels, after electrical stimulation. Subsequently, the same tissue slices underwent further analysis aimed at identifying the regions impacted by I/R injury through TTC staining. In parallel, RNAscope experiments were performed on consecutive tissue slices, revealing valuable insights into regional gene transcription patterns.

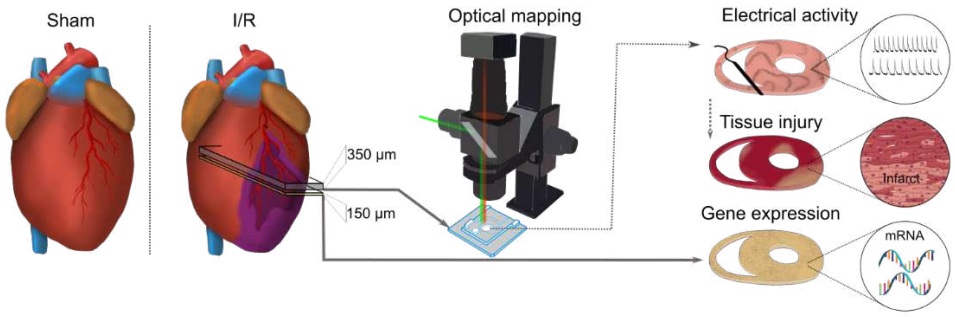

***Fig. 3. Experimental Workflow**. Sham and I/R hearts were first sectioned transversally into slices of 350 µm thickness. These slices underwent optical mapping and subsequent TTC staining for assessment. Corresponding consecutive tissue slices, each measuring 150 µm, were subjected to analysis of gene expression using RNAscope.*

Fig. 4 provides a detailed representation of AP mapping obtained from slices of the LV in both sham (Fig. 4A) and I/R injured (Fig. 4B) mouse hearts. It is noteworthy that the background fluorescence intensity in the sham group indicates uniform distribution of the dye across the entire section. The activation time map depicted in the upper panel of Fig. 4A reveals anisotropic AP propagation patterns across the entire slice. Conversely,

when examining slices from hearts subjected to I/R-injury, background fluorescence signals point to areas of absent dye infiltration within the infarcted area. Consequently, this lack of dye penetration hinders the detection of electrical activity within the corresponding activation map, as depicted in the upper panel of Fig. 4B.

To investigate transmural early AP repolarization, APD_{50} was recorded in both sham and I/R-injured tissue slices, illustrated in Fig. 4 (bottom panels). In the APD_{50} map of healthy left ventricular slices, a spatially uniform APD was observed, characterized by a shortening towards epicardial regions. Representative normalized AP waveforms (labeled 1 to 5) displayed distinctive features, such as sharp, short, and triangular shapes devoid of a plateau phase. Notably, these waveforms exhibited a notable shortening of APD_{50} in the endo- to epicardial extent, indicated in Fig. 4A (bottom panel).

In contrast, the transmural contour maps of APD_{50} within I/R-affected tissue slices exhibited an inhomogeneous prolongation of APD_{50}, predominantly concentrated in the vicinity of the infarcted region, with a distinct emphasis on epicardial regions, depicted in Fig. 4B (bottom panel). A comparison of selected AP waveforms along the transmural axis (labeled 1 to 5) revealed a noticeable plateau phase during early repolarization, particularly prominent in epicardial regions close to the I/R-affected area.

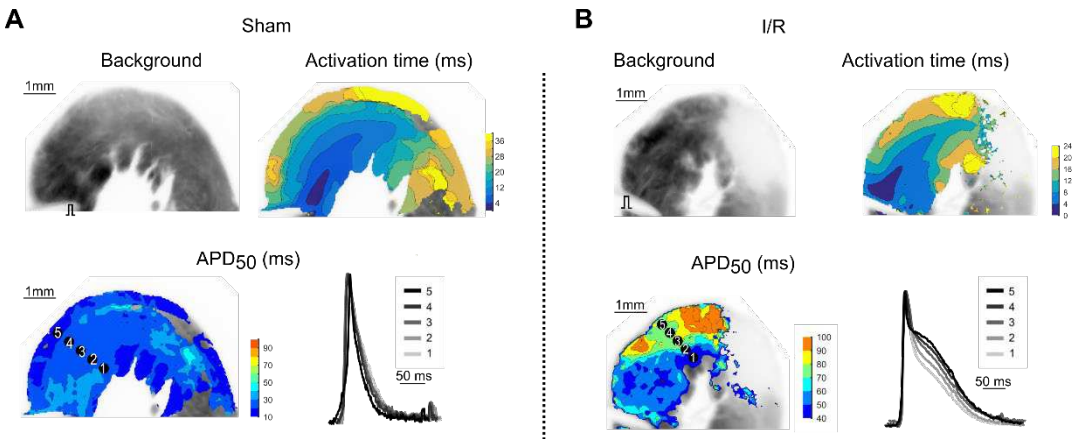

Fig. 4. Visualization of AP dynamics and kinetics in left ventricular slices from both sham-operated (A) *and I/R-injured hearts* ***(B)****. The activation time maps illustrate the propagation of stimulated APs under a pacing cycle length (PCL) of 300 ms, depicted with a color spectrum from blue to yellow. Spatial distributions of* APD_{50} *across the sections are represented in* APD_{50} *maps, color-coded from blue to orange. Overlaid APs across the endocardial to epicardial extent (1-5) are also presented for reference.*

The comprehensive analysis, as depicted in Fig. 5, has brought to light to a noteworthy variation in APD_{50} values between epicardial and endocardial regions, evident in both sham-operated and I/R injury groups. In the sham group, it is worth noting that the endocardial cells displayed a more extended APD_{50} (27 ± 2 ms) compared to the epicardial cells, which exhibited a notably quicker repolarization (16 ± 4 ms), supported by two way ANOVA test (p value= 0.0057, n = 5). This observation emphasizes a marked transmural gradient in early AP repolarization dynamics within the examined sham tissue slices, where epicardial cells exhibit a swifter recovery from excitation.

However, in hearts subjected to I/R injury, the situation evolves. A comprehensive quantification of APD_{50} values reveals a substantial and statistically significant prolongation of the early repolarization phase among epicardial in contrast to endocardial cells. Specifically, the APD_{50} values within epicardial regions experience a pronounced prolongation, measuring at 86 ± 22 ms, while the endocardial regions display a significantly shorter APD_{50} of 29 ± 11 ms (p value= 0.0055, n = 7). Additionally, The fixed effects parameters from ANOVA test showed that the p value for transmural heterogeneity is 0.0015 (**) and for I/R injury is 0.0008 (***). The interaction between I/R injury and transmural heterogeneity is highly significant, with a p-value less than 0.0001 (****). This finding underscores the emergence of a distinct transmural heterogeneity in early AP repolarization kinetics under the influence of I/R injury, wherein epicardial cells exhibit a substantial lengthening of the repolarization phase. Furthermore, the data indicate a notable reversal in transmural APD gradient near the I/R injury site.

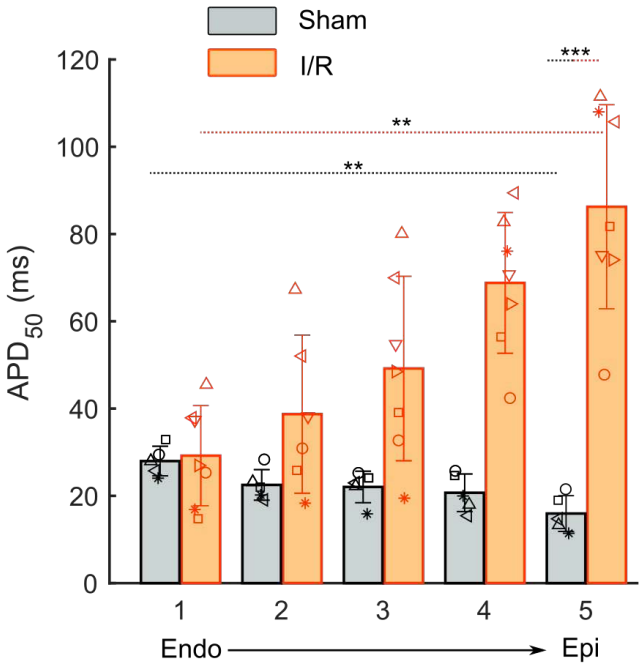

Fig. 5. Quantitative assessment of regional APD_{50} gradients in sham (n = 5) and I/R tissue (n = 7) samples. *Each symbol corresponds to data from a specific slice within their respective groups. Statistical analysis was conducted using a two way ANOVA test with Sidak's multiple comparisons (** p < 0.01, *** p < 0.001).*

When subjected to rapid pacing (PCL = 200 ms), I/R-injured cardiac tissue commonly displays repolarization alternans characterized by alternating amplitudes in consecutive APs (135,136). This alternans phenomenon contributes to spatial and temporal heterogeneity in AP repolarization. In this study, both sham-operated and I/R-injured left ventricular slices were subjected to pacing at a 200 ms cycle length, and their AP amplitudes were analyzed along the transmural axis (see Fig. 6). Analysis of calculated alternans maps revealed the absence of transmural beat-to-beat oscillations in all sham tissue slices. The superimposed consecutive APs from the endocardial and epicardial regions confirmed the absence of any form of AP alternans, as depicted in upper left panel of Fig. 6. In contrast, within epicardial regions affected by I/R injury, pronounced AP alternans was evident. An overlay of representative APs demonstrated the emergence of AP alternans, particularly in the epicardium, as illustrated in the bottom left panel of Fig. 6.

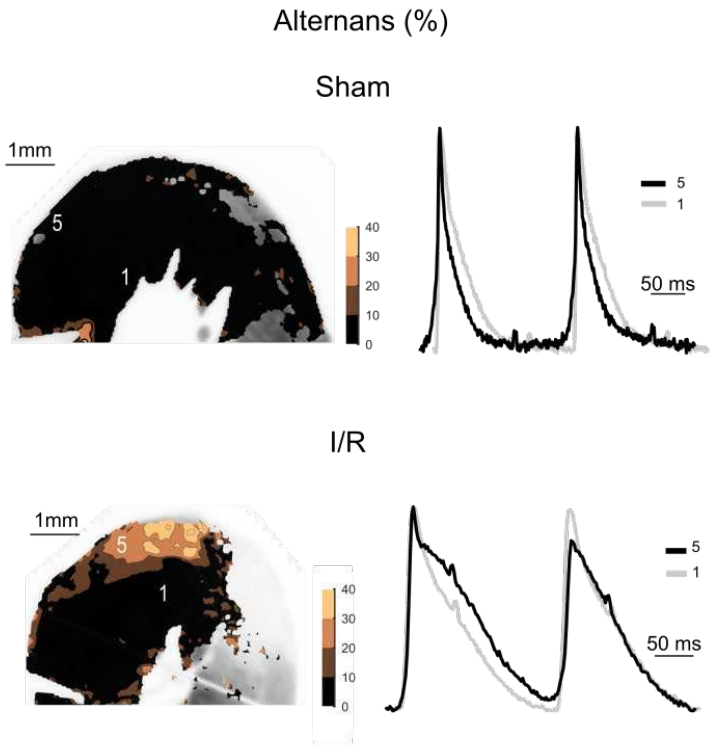

Fig. 6. Alternans maps of APs in slices of sham-operated and I/R-injured hearts*. These maps, which correspond to the same sections as those in Fig. 2, were generated using a PCL of 200 ms, represented in a black- creme color scheme. Representative consecutive APs from the endocardial and epicardial regions (1, 5) have been superimposed.*

Following optical mapping, TTC staining of the same tissue slices confirmed the localization of tissue damage resulting from I/R injury (Fig. 7). The delineation of infarcted tissue was compared to the absence of background fluorescence, as observed in Fig. 4B. Consequently, to test the hypothesis of ventricular re-expression of $Ca_V1.3$ following AMI, the tissue slices, which followed those used for optical mapping, underwent Cacna1D RNAscope *in situ* hybridization. The results presented in Fig. 7 pertain to the tissue slice that immediately followed the one depicted in Fig. 4. Detailed magnifications along the transmural axis revealed the exclusive expression of Cacna1D in epicardial regions proximal to the I/R injury site.

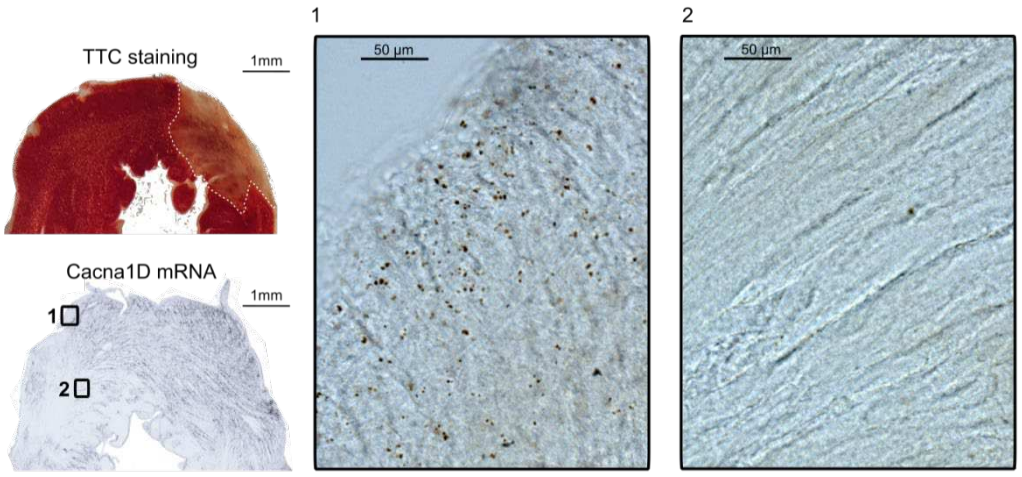

Fig. 7. TTC staining and Cacna1D In Situ Hybridization of I/R injured heart. *The I/R tissue slice underwent TTC staining after optical mapping, while the following sequential slice was subjected to Cacna1D mRNA in situ hybridization using RNAscope. Insets depict magnified views of the epicardial and endocardial regions, as denoted (1, 2). The hybridized probes appeared as brown dots.*

3.1.2. Transition of LTCCs isoforms and mathematical simulation in mouse ventricular APs

As discussed above, in the healthy adult mouse heart, co-expression of $Ca_V1.2$ and $Ca_V1.3$ is only observed in atrial, SAN, and AVN myocytes, while $Ca_V1.2$ is exclusively expressed in ventricular myocytes (137,138). To investigate cell-specific gene remodeling of LTCCs after I/R injury, ventricular co-hybridization of $Ca_V1.2$ and $Ca_V1.3$ mRNA probes was performed. The use of multiplex fluorescence RNAscope for Cacna1C and Cacna1D, which encode for $Ca_V1.2$ and $Ca_V1.3$, respectively, validated the exclusive presence of Cacna1C in the left ventricular sections under normal conditions. However, following an I/R injury, co-expression of Cacna1D with Cacna1C was observed within the same ventricular myocyte nuclei (see Fig. 8).

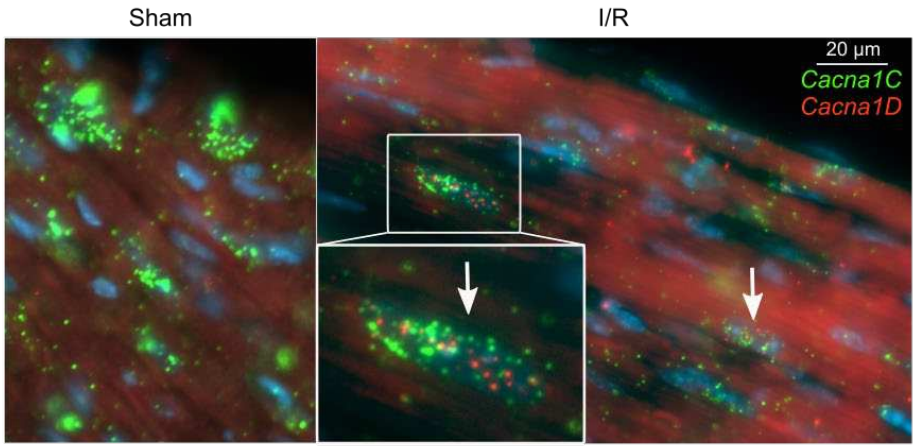

Fig. 8. Co-expression of Cacna1D and Cacna1C after I/R injury. *Multiplex fluorescence RNAscope for Cacna1C and Cacna1D in left ventricular sections from sham and I/R hearts. White arrows indicate co-localization of Cacna1D and Cacna1C.*

Next, a mathematical model of a single cardiomyocyte was employed to explore the functional implications of a shift in LTCC isoforms as described above within mouse ventricular APs (131), in line with the findings of Srivastava et al., who demonstrated the re-expression of $Ca_V1.3$ and the down-regulation of $Ca_V1.2$ genes in failing human hearts (139). The model takes into account the electrical characteristics of membrane ionic currents and the regulation of calcium levels inside the cell, which collectively contribute to the generation of APs in mouse ventricular myocytes (Fig. 9). In the present project, the model formulation was assembled in MATLAB and was then further refined based on recent reports, focusing on the time-independent I_{k1} and the sodium/potassium ATPase (I_{NKA}) (132,133,140). These adjustments ensured temporal stability of the model concerning intracellular ion concentrations across various stimulation frequencies (1-10 Hz). The integration of $Ca_V1.3$ into the ionic model involved modifying a Markovian model (134) formulation for $Ca_V1.2$, in conjunction with the utilization of available experimental data describing $Ca_V1.3$ gating properties (101,141,142). Prior investigations have demonstrated that $Ca_V1.3$ displays a voltage-dependent activation that is shifted towards more negative potentials, approximately by 20 mV, in comparison to $Ca_V1.2$ (142). Furthermore, $Ca_V1.3$ exhibits both faster activation (by approximately 30%) and slower inactivation (by approximately 30%) kinetics compared to $Ca_V1.2$ (141). The current-voltage (I/V) relationship for $Ca_V1.3$ in SAN myocytes was

described by Mangoni et al. by the subtraction of I_{CaL} recorded in $Ca_V1.3^{-/-}$ cells from the total I_{CaL} in WT cells (101), as depicted by the digitized data points in Fig. 9B.

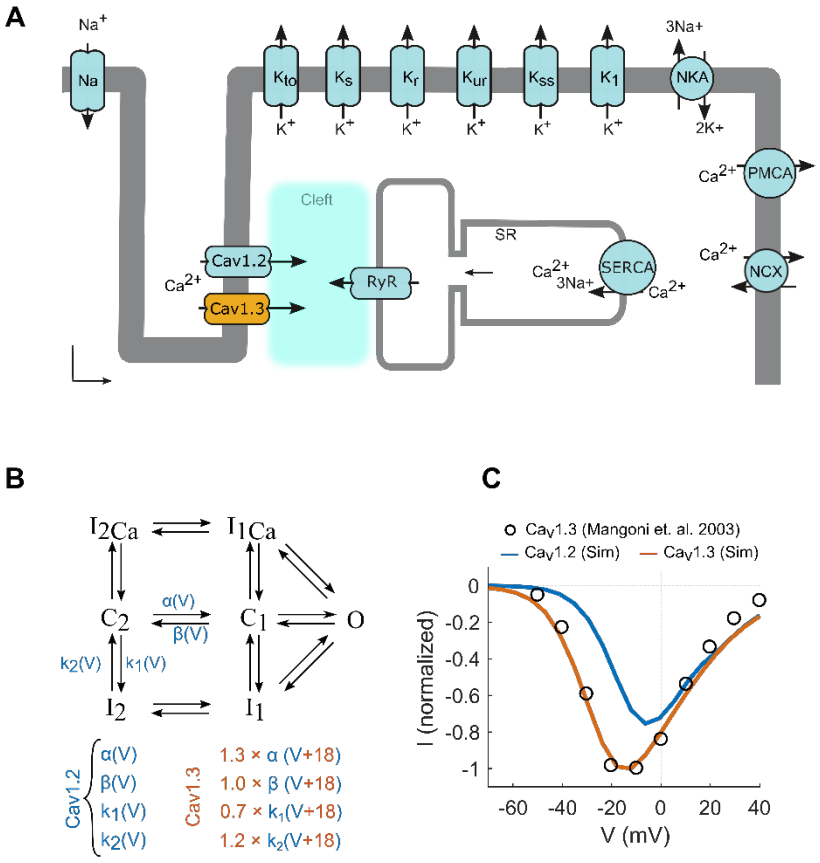

Fig. 9. Integration of a $Ca_V1.2$ Markovian model and development of a $Ca_V1.3$ model. (A) *a mathematical model representing a single mouse ventricular AP was created to include $Ca_V1.3$.* ***(B)*** *The Markovian model for $Ca_V1.2$ (depicted in blue) was changed by incorporation of experiment-derived parameters, as indicated in orange color. This integration process led to the development of a $Ca_V1.3$ model.* ***(C)*** *Simulated current-voltage relationships for $Ca_V1.2$ and $Ca_V1.3$ overlaid with experimental data of Ca_V 1.3 recordings from SAN cells.*

Similar voltage-clamp experiments were then simulated to adjust the parameters shown in Fig. 9B in order to fit the normalized experimental data of the $Ca_V1.3$ I/V relationship. The currents simulated for both isoforms demonstrate that $Ca_V1.3$ activates at more negative potentials than $Ca_V1.2$, as shown in Fig. 9C.

Next, the functional consequences of $Ca_V1.3$ expression during a monoexponential LTCC transition from $Ca_V1.2$ to $Ca_V1.3$ in mouse ventricular myocytes were simulated,

with pacing at a 300 ms cycle length (Fig. 10A). $Ca_V1.2$ conductivity was decreased from 100% to 50%, while CaV1.3 conductivity was simultaneously increased from 0% to 50%. As the expression of $Ca_V1.3$ increased, the model anticipated an increase in APD, extending from approximately 12 ms to around 65 ms. A notable elevation in APD was observed after approximately 85 seconds, as depicted in Fig. 10C. To better understand how $Ca_V1.3$ expression affects the AP, the changes in membrane potential (V_m) and I_{CaL} at 1 s (1), 85 s (2), and 210 s (3) were magnified and plotted in Fig. 10B. At first, as $Ca_V1.3$ expression increased, EADs appeared and caused the APD to prolong significantly. Later on, EADs disappeared, most likely because the LTCCs inactivated as the intracellular calcium concentration increased.

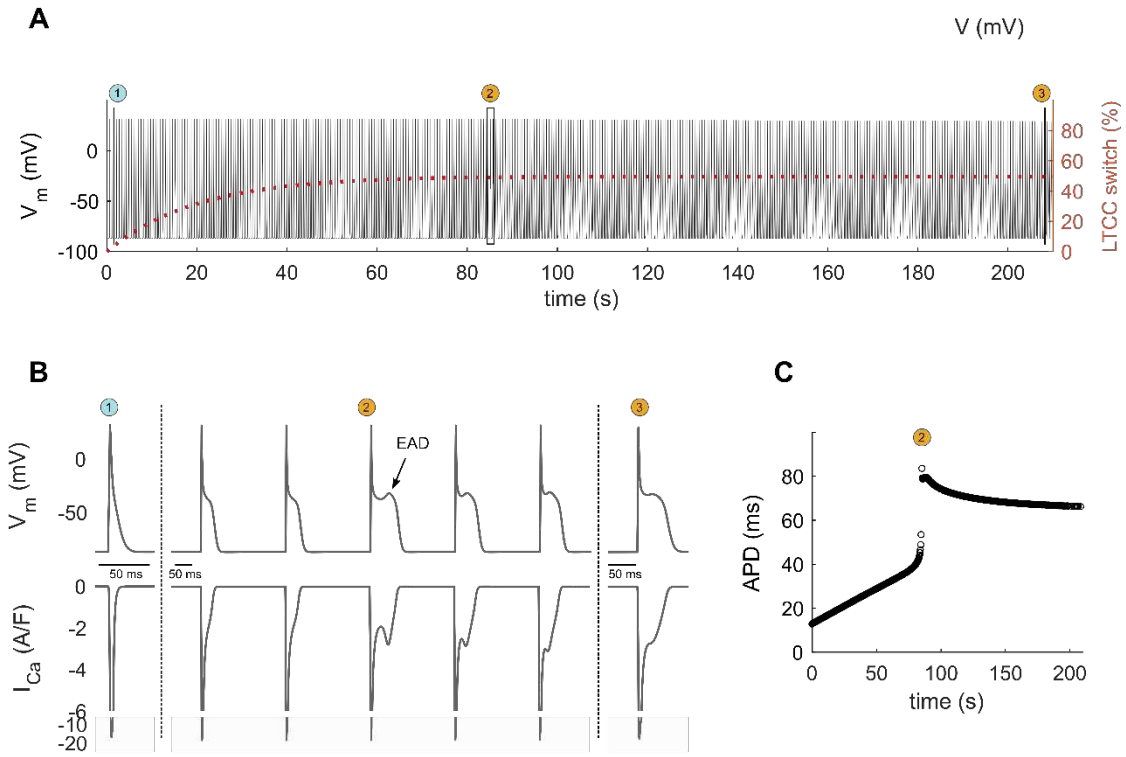

Fig. 2. Simulation of APs by gradually boosting $Ca_V1.3$ conductance while simultaneously decreasing $Ca_V1.2$ conductance over time. (A) *To mimic the LTCC isoform switch, $Ca_V1.3$ conductance was progressively increased from 0% to 50%, while, concurrently, $Ca_V1.2$ conductance was lowered from 100% to 50% over a period of 210 s with an exponential rate of 0.05s.* ***(B)*** *The AP and the associated Ca^{2+} currents within specified time intervals (windows 1 (1s), 2 (85s), and 3 (210s)) as depicted in (A) demonstrate prolonged APD and the occurrence of EADs.* ***(C)*** *shows the temporal progression of APD prolongation.*

The simulations also suggest that if the transition in the LTCC occurs more rapidly over time, it could potentially result in a failure of repolarization, as depicted in Fig. 11. In conclusion, these simulations support the idea that the re-expression of $Ca_V1.3$ in myocardial tissue following I/R injury could lead to an extended plateau phase during early repolarization of APs. This phenomenon is well-recognized for increasing the risk of arrhythmias.

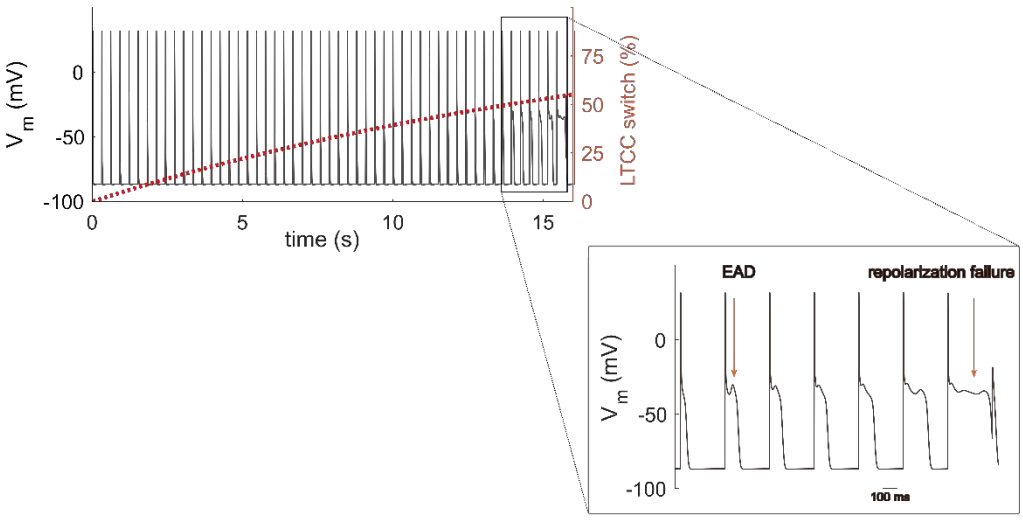

Fig. 3. Mathematical simulation of a fast LTCC isoform transition and the resulting repolarization failure*. Simulating APs with a more rapid $Ca_V1.2$ to $Ca_V1.3$ transition, as compared to the scenario depicted in Fig. 10, resulted in a repolarization failure.*

3.1.3. Pharmacological emulation of LTCC isoform transition and its influence on AP morphology

To further investigate the functional impacts of the observed LTCC isoform transition, the compound FPL 64176 was employed. This compound was chosen due to its ability to align the I/V characteristics of ventricular myocytes, which exclusively express $Ca_V1.2$ channels, with those of SAN myocytes expressing $Ca_V1.3$ channels (Fig. 12). This alignment hence served as a model for studying the influence of the LTCC isoform transition on cellular electrophysiological properties. As previously noted, Toyoda et al. reported that the recorded I_{CaL} in SAN cells from mice lacking $Ca_V1.3$ channels displays a positive shift of approximately 20 mV in its I/V relationship when compared to wild-type

SAN cells expressing both $Ca_V1.2$ and $Ca_V1.3$ channels.(142) Fig. 12A provides a graphical representation of the digitized data points illustrating these corresponding I/V relationships. Additionally, Fan et al. observed that the LTCC agonist, FPL 64176, augments channel conductance and induces a shift in voltage-dependent activation toward more hyperpolarized potentials in isolated rat ventricular myocytes. (Fig. 12B) (143).

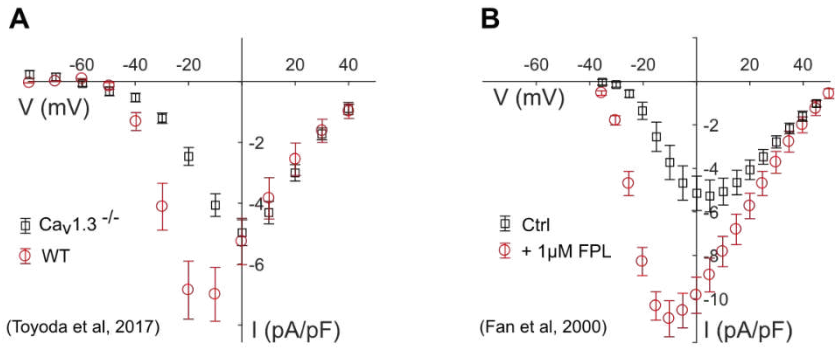

Fig. 4. Depiction of Ca^{2+} I/V relationships for SAN cells sourced from both wild-type and $CaV1.3^{-/-}$ mice (A), and from rat ventricular myocytes before and after application of FPL 64176 (B). *Digitized from indicated reports in the literature* (142,143).

To assess the suitability of optical mapping on heart slices as a method for investigating the impact of pharmacological agents, an examination using a control sample slice obtained from a healthy adult mouse was conducted. The observation period extended for more than 5 hours, during which various electrophysiological parameters were studied. These parameters included activation time, conduction velocity (CV), the APD at 50% repolarization (APD_{50}), and AP morphology. Fig. 13 provides a comprehensive visualization of the temporal evolution of the APD_{50} in the tissue slice over the recording duration, demonstrating a stable APD_{50} value of 20 ms. Additionally, two sample APs were chosen for comparison: one at t_1=20 minutes when the AP reached stability and another at t_2=300 minutes, both originating from the exact same region. These comparisons revealed no discernible differences in morphology between the two APs. At both time points, the APs displayed consistent triangular shapes and temporal characteristics that are typical of murine adult APs. The calculated activation times consistently indicated AP propagation at a speed of 0.21 ± 0.03 mm/ms,

closely resembling the physiological CV within the murine heart (144). In light of the consistent parameter stability observed throughout this extended recording period, it can be deduced that this method is well suited for investigating the effects of pharmacological agents on AP morphology and propagation.

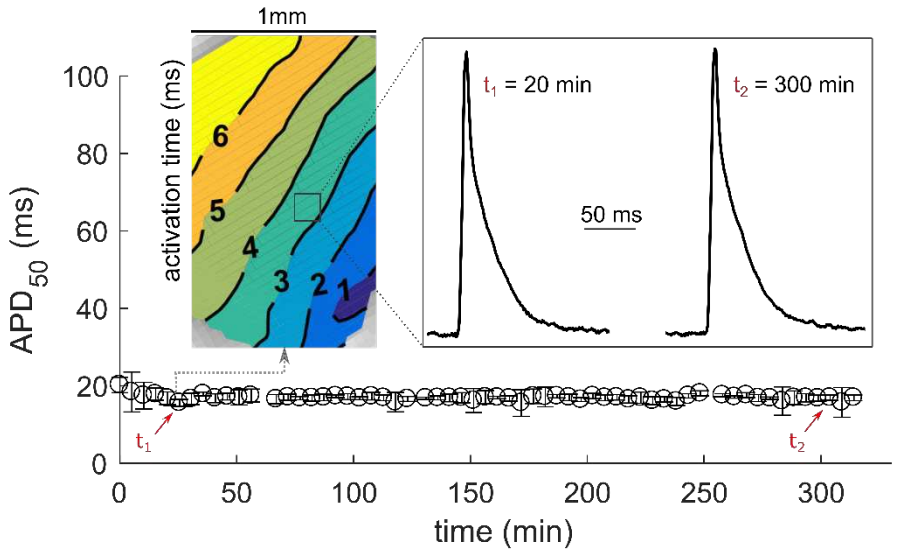

Fig. 5. Optical mapping of a normal murine ventricle slice under control conditions. *Upon stimulation at a PCL of 300 ms, the isochronal activation times (measured in ms) demonstrated the propagation of AP. The APD_{50} exhibited stability over a five-hour period. Representative single APs from specified time points (t_1 and t_2, as indicated) during the experiment were isolated.*

The application of FPL 64176 at a concentration of 500 nM led to a notable prolongation of APD_{50} over time, eventually reaching a stable state after approximately 75 minutes (Fig. 14A). The overlayed normalized APs illustrate the temporal progression of alterations in AP morphology, characterized by a prominent shoulder during the early repolarization phase, while the initial depolarization phase remained largely unchanged (Fig. 14B). Quantitative analysis reveals a threefold increase in the APD_{50} over time, transitioning from an initial value of 24 ± 5 ms to a final value of 73 ± 14 ms (Fig. 14C; n = 10, p value= 10^{-5}).

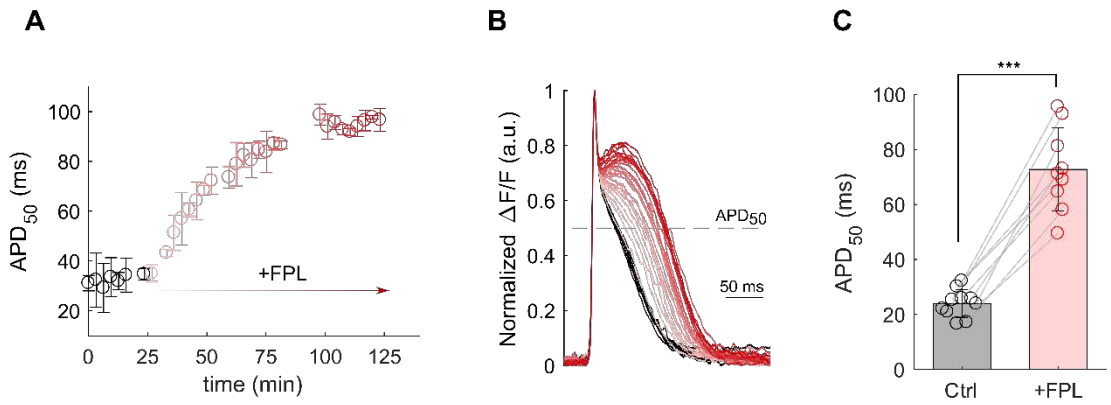

Fig. 6. The pharmacological activation of LTCC by FPL64176 at a concentration of 500 nM leads to APD_{50} prolongation. (A) *Temporal variations in left ventricular APD_{50} subsequent to the introduction of FPL64176 into the extracellular solution at t=25 minutes.* ***(B)*** *overlay of normalized APs from (A)* ***(C)*** *The assessment of APD_{50} prolongation induced by FPL64176 using a paired Student's t-Test (n = 10; male/female) revealed statistically significant differences (*** indicating a p-value < 0.001).*

Interestingly, it was observed that increased levels of FPL at a concentration of 1 µM resulted in the occurrence of EADs and even repolarization failure, as illustrated in Fig. 15A and B, respectively. The time-resolved activation mapping revealed the homogeneous propagation of the initial depolarization (t_1) of the AP, while EAD formation (t_2) induced ectopic excitation with circular and unidirectional propagation, as shown in Fig. 15B.

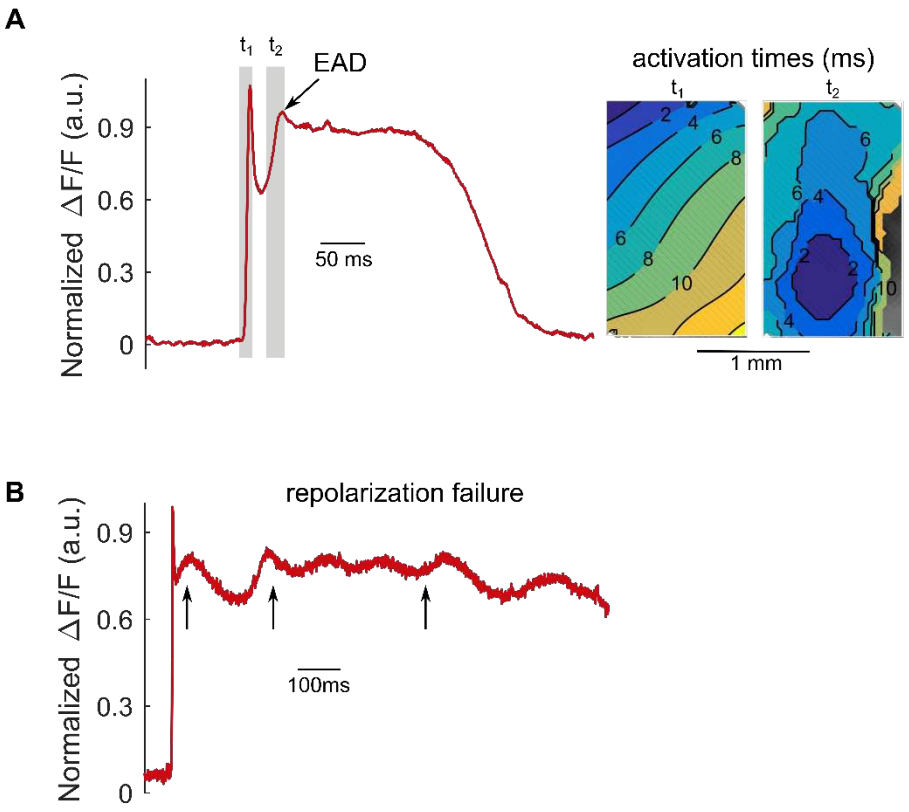

Fig. 7. EAD formation and repolarization failure at high concentrations (1uM) of FPL64176. (A) *Activation map for the initial depolarization and EAD at specified time points (t_1, t_2) are displayed.* ***(B)*** *In some cases, repolarization failure was observed, with consecutive EADs (indicated by arrows).*

3.1.4. Reversing APD prolongation following I/R injury by inhibiting LTCC

The pharmaceutical compound diltiazem, classified as a class IV antiarrhythmic drug, is well recognized as an inhibitor of LTCCs (145). In clinical applications, its actions encompass a decrease in heart rate and slowing the CV within the AVN (146). Here, the effects of diltiazem on AP morphology and its propagation within LV slices subsequent to I/R injury were studied, as illustrated in Fig. 16. Activation maps revealed that application of 5 µM diltiazem delayed AP propagation, as evidenced by the presence of more closely spaced isochrones (Fig. 16A). Furthermore, AP prolongation at epicardial regions following I/R injury was corrected by diltiazem, yielding a comparatively uniform early repolarization pattern, as depicted by APD_{50} maps (Fig. 16B). The impact of LTCC inhibition on AP morphology may be appreciated in the overlayed APs obtained from representative endocardial (1) and epicardial (2) sites in Fig. 16C. This study demonstrates that diltiazem effectively reverses the early repolarization shoulder

appearing in epicardial APs following I/R injury. Notably, at higher concentrations of diltiazem (> 10 µM), a complete conduction block was observed, which may be attributed to off-target effects, including sodium channel inhibition.

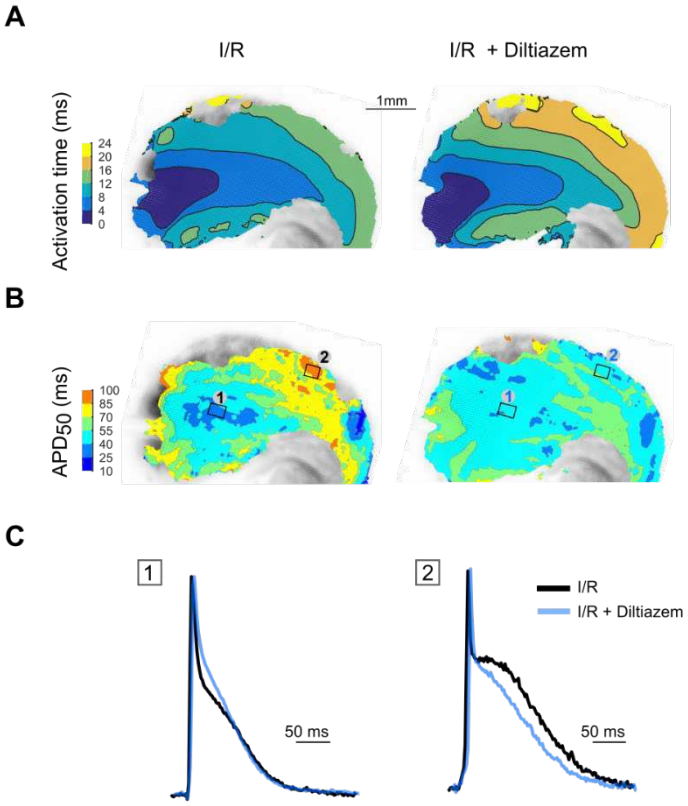

Fig. 8. Pharmacological inhibition of LTCC reverses the widening of murine left ventriclar APs following I/R injury. activation map (A) *and* APD_{50} *map* ***(B)*** *of I/R injured left ventricular cardiac slices before and after the application of 5 µM diltiazem, an LTCC inhibitor****. (C)*** *overlayed APs from midcardium (1) and epicardium (2), corresponding to the regions marked in (B).*

3.2. Sex-specific repolarization heterogeneity in mouse left ventricle

3.2.1. Sex-dependent repolarization characteristics in murine ventricular tissue slices

To optically analyze locoregional AP features in adult male and female mice, attention was directed towards three key regions and parameters of interest within the LV: the entire LV free wall, the epicardium, which corresponds approximatively to the outer one-third of the LV free wall, and the transmural APD gradient within LV. An exclusion zone of approximately 30 degrees was defined on both the anterior and posterior sides of the cardiac slice. This exclusion zone, as illustrated in Fig. 17, effectively excluded the anterior and inferior heart regions from the analysis, leaving a central region of 120 degrees, which accurately represents the LV free wall. Furthermore, the papillary muscles were also excluded from the analysis.

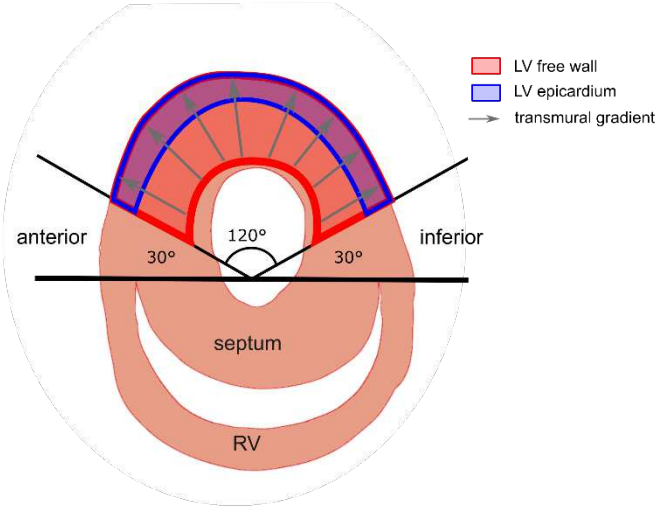

Fig. 9. Schematic illustration of the three locoregional regions and parameters analyzed in the LV of adult male and female mice for AP features. *The analysis regions included the entire LV free wall (highlighted in red), the epicardium, representing one-third of the LV free wall (highlighted in blue), and the transmural gradient of APD (indicated by gray arrows). Papillary muscles and a zone of approximately 30 degrees were excluded from both the anterior and posterior sides, leaving 120 degrees LV free wall for analysis. This figure was modified from previously published work* (128).

Sex-specific disparities in the spatial distribution of APD_{90} within the LV are depicted in color-coded maps, employing a stimulation frequency of 5 Hz (Fig. 18A). The

quantitative analysis, as presented in Fig. 18B, reveals a statistically significant distinction in epicardial APD_{90} between male and female LV slices (p value= 0.0061), based on data obtained from six male and nine female mice, respectively. Notably, this observed difference in epicardial APD_{90} was not mirrored in the entire LV APD_{90} or their respective SD, which remained comparable between the two sexes.

While the APD_{90} and their SD in the entire LV were not found to be significantly different between sexes, a significant negative transmural gradient in APD_{90} towards the epicardium was observed in LV slices of male mice. Notably, this gradient displayed a substantial reduction in the LV slices of female mice, as depicted in Fig. 19 and outlined in further detail in Table 5 (p value= 0.00002). Furthermore, an examination of the coefficients of variation (COV) revealed a noteworthy increase in the dispersion of epicardial APD_{90} (MSLRT = 5.1, p value = 0.023) and transmural APD gradients (MSLRT = 18.4, p value= 1.7 × 10−5) in female mice as compared to their male counterparts.

Table 5. Calculated variations in the indicated APDs and transmural gradients in male and female mice, along with the corresponding confidence intervals, employing hierarchical nested statistical analysis.

	estimated difference (ms)	**standard error (ms)**	**df**	**t value**	**lower limit**	**upper limit**	**Bonferroni p-value**
APD_{30}	0.686	0.687	15.0	1.000	-0.77	2.150	0.302
APD_{50}	-5.744	3.164	15.6	-1.81	-12.46	0.979	0.080
APD_{80}	-9.738	3.382	18.0	-2.880	-16.84	-2.634	0.009
APD_{90}	-9.273	3.024	18.0	-3.067	-15.63	-2.920	0.006
APD_{90} gradient	-8.292	1.415	16.8	-5.861	-11.28	-5.305	0.00002

This Table, directly adapted from the work previously published (128).

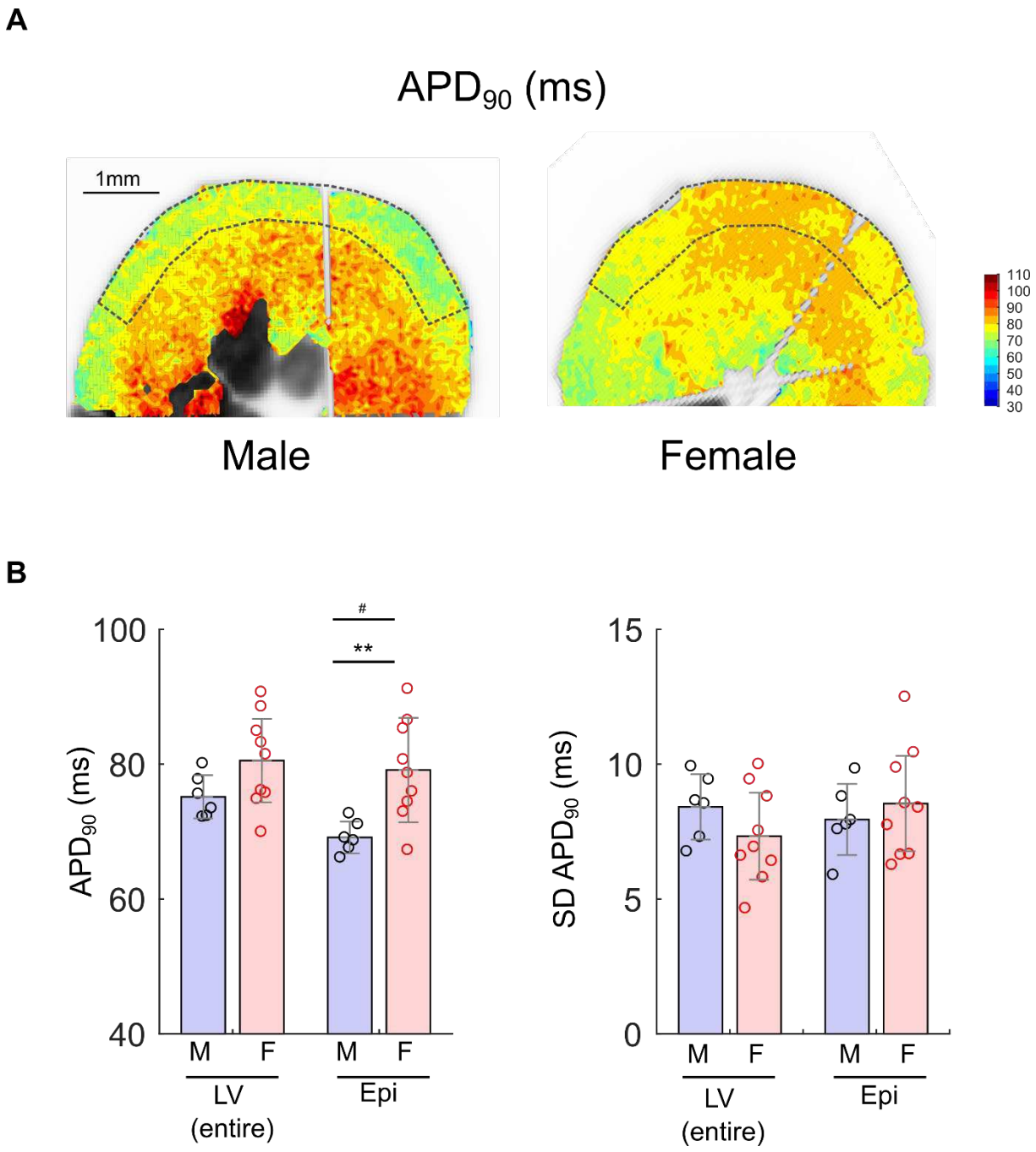

Fig. 10. Comparative analysis of APD_{90} in the LVs of adult male and female mice. (A) *Optical mapping of APD_{90} in transverse LV Slices of male (left) and female (right) mice* ***(B)*** *Bar graphs illustrating the APD_{90} and its SD obtained from male (M) and female (F) mice. The measurements were taken from both the entire left ventricular free wall (LV(entire)) and the epicardium (Epi). Sample sizes included six males (M) and nine females (F). The significance of the observed differences is denoted by ** ($p = 0.0061$) for APD_{90} and # ($MSLRT = 5.1$, $p = 0.023$) for SD. Figure was modified from prior publication* (128).

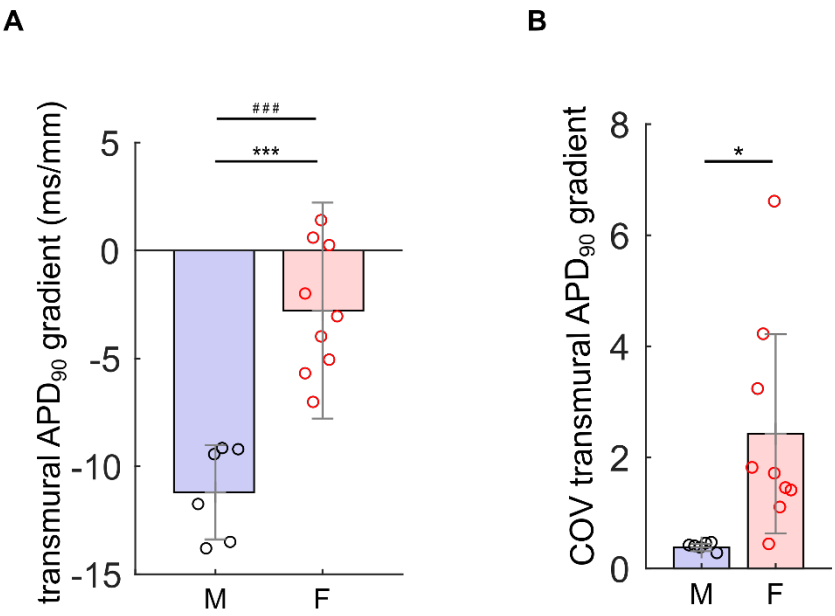

Fig. 19. Transmural gradient and COV in APD in male and female mice. (A) *the distinctive transmural gradient in APD_{90} observed between male and female mice is presented, along with corresponding confidence intervals. The data were derived using hierarchical nested statistical analysis, with sample sizes including six males (M) and nine females (F), with *** indicating a significant difference ($p = 1.8\times 10^{-5}$), and ### signifying the result of the MSLRT test (18.4, $p = 1.7 \times 10^{-5}$).* ***(B)*** *the increase in dispersion of epicardial APD_{90} in female mice, as indicated by * ($p = 0.023$) in comparison to their male counterparts, is depicted by COV analysis. Figure was modified from prior publication* (128).

With the most pronounced manifestation of sex-specific APD heterogeneity observed within the epicardium, a focused inquiry was conducted in this region of particular interest. Overlaying epicardial AP morphologies conceals the presence of longer APD, especially during late repolarization, in female mice as compared to their male counterparts, both illustrated and quantified in Fig. 20.

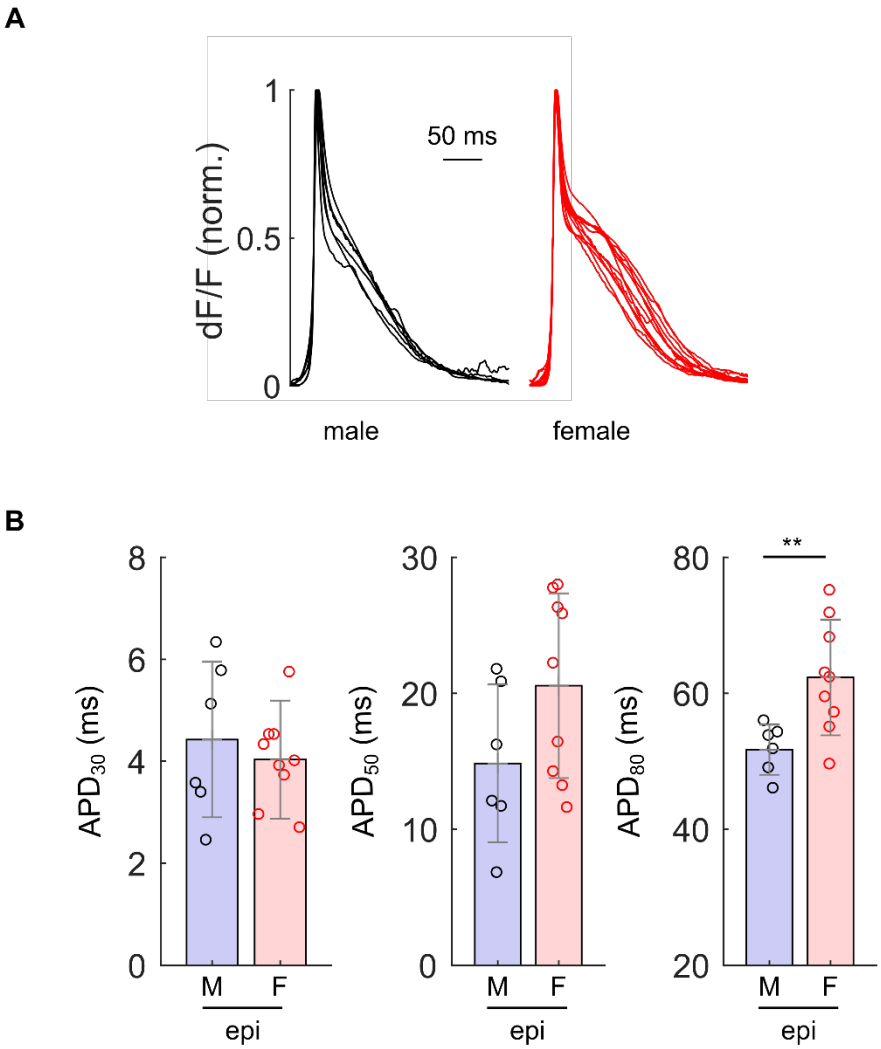

Fig. 11. Representative epicardial APs in male and female mice. (A) *Sample APs from the epicardial region of 6 male and 9 female mice.* ***(B)*** *Quantitative representation of APD at different phases, including APD_{30}, APD_{50}, and APD_{80}. A marked distinction emerged in APD_{80}, indicated by a significant p-value of 0.009 (**).*

3.2.2. Modelling the Contribution of Ionic Currents to Mouse Cardiomyocyte AP morphology

The debate over the sex-specific expression and functionality of ion channels (Table 1) necessitated the use of mathematical modelling to further elucidate and compare the potential differences in ionic current modulation. Fig. 21A illustrates a schematic representation of an electrophysiological model for a single mouse cardiomyocyte that was originally developed by the Bondarenko group (147).

As most debates surrounding the sex-specific regulation of ion channels in cardiomyocytes revolve around potassium channels, the maximum conductivities of potassium currents within the model were initially compared. It was observed that in mouse cardiomyocytes, g_{Kr} and g_{Ks} play relatively minor roles in comparison to other currents, resulting in their exclusion from further analysis (Fig. 21B). Instead, the influence of the remaining potassium currents on AP morphology was subjected to a more detailed assessment. This was achieved by mathematically simulating variations in current densities, both increases and decreases of up to ±50%. A stimulus pulse was administered for a duration of 5 s at a frequency of 5 Hz. Emphasis was placed on the changes in AP morphology induced by the series of simulations as conductivity levels were adjusted. The APs from separate stimulations were superimposed to enhance the visual appreciation of differences (Fig. 22).

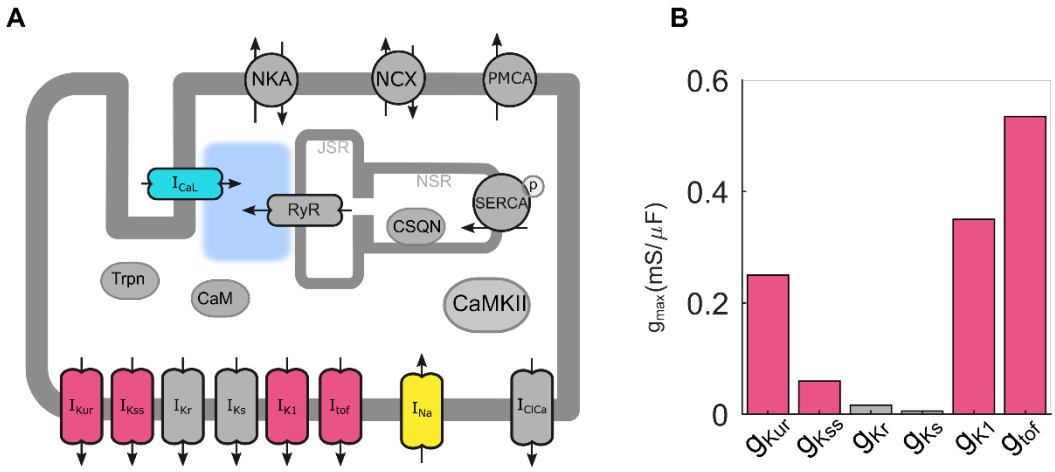

Fig. 12. Schematic diagram of the AP in left ventricular cardiomyocytes, illustrating the elative contribution of various implemented K^+ currents in the herein developed model. (A) *Depicts the profile of different ionic currents and calcium fluxes based on Bondarenko's electrophysiology for single cardiomyocytes.* ***(B)*** *Represents the conductivity of contributing K^+ currents according to the model, with gray columns indicating conductivities deemed to have a negligible role in AP morphology according to the model's analysis. Figure was modified from prior publication* (128).

As expected, a reduction in all K^+ current densities led to the prolongation of APD, while changes in I_{K1} alone resulted in an alteration of the resting membrane potential. However, since no reliable sex-specific differences in resting membrane potential were

observed in previous experimental data, I_{K1} was subsequently excluded from further investigation in this context (59,60,62). A decrease in I_{Kur} was foreseen to result in the extension of APD_{30} and APD_{80} by as much as 4% and 29%, respectively. Conversely, a reduction in I_{to}, according to the model, implied an increase in APD by up to 16% during early repolarization and 28% during late repolarization phases. For reductions in I_{Kss}, the model indicated APD changes of less than 4%. These observations have been depicted in Fig. 22B, illustrating the relationship between APD_{30} and APD_{80} and the corresponding conductivities (g) of K^+ currents (I_{to} and I_{Kur}). It is noteworthy that while both I_{to} and I_{Kur} significantly influence late repolarization (APD_{80}), early repolarization (APD_{30}) is primarily shaped by I_{to} alone.

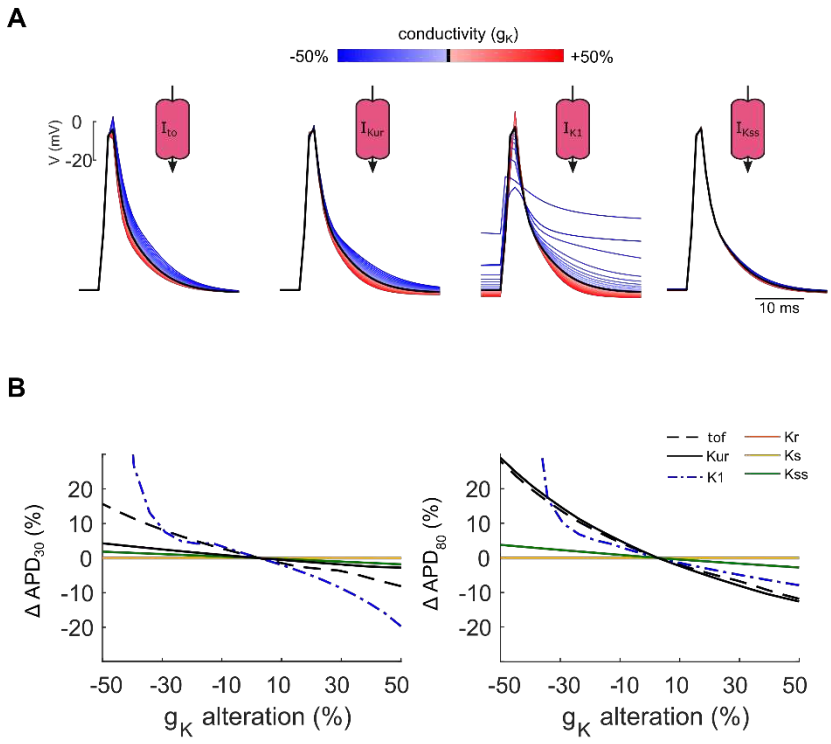

Fig. 13. The simulation of APs through a systematic adjustment of specified K^+ channels conductivities. ***(A)*** *showcases the simulated variations in APs resulting from a gradual modification of indicated K^+ conductivities (g_k), ranging from a decrease of 50% to an increase of 50% relative to the control condition.* ***(B)*** *illustrates the consecutive changes in APD_{30} and APD_{80} against the percentage change in g_k. I_{K1}, I_{KSS}, I_{to}, and I_{Kur} abbreviate inward rectifier K^+ current, steady-state K^+ current, transient outward K^+ current, and ultrarapid delayed-rectifier K^+ current, respectively. Figure was modified from prior publication* (128).

In the subsequent phase, the influence of I_{Na} on AP morphology was mathematically simulated utilizing a Markov model (147). As illustrated in Fig. 23, by altering the transition rate constant of the Na^+ channel from a fast-inactivated state (IF_{Na}) to the open state (O_{Na}) within a range of -50% to +50%, a corresponding decrease and increase of 9% were observed in APD_{80}. Collectively, the mathematical simulations underscore the primary impact of I_{to} on early repolarization, while both I_{to} and I_{Kur} jointly exert a comparable and dominant influence on late repolarization, which is partially counterbalanced by the baseline activity of I_{NaL}.

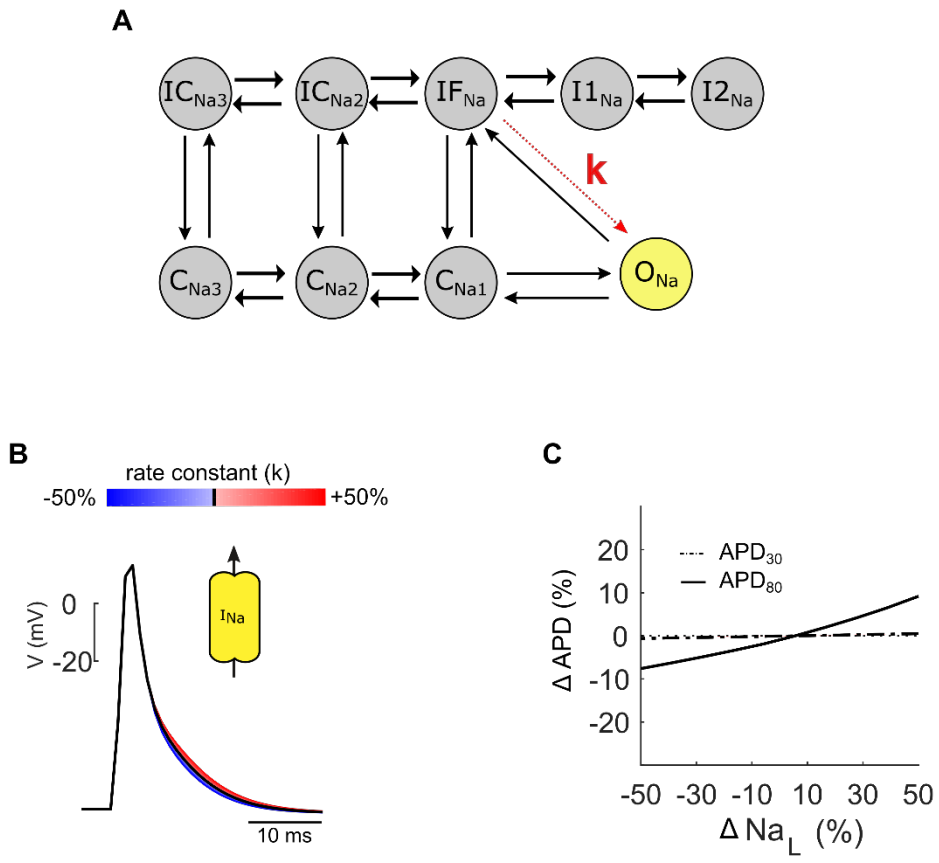

Fig. 14. Mathematical modelling of action potential (AP) morphology via modulation of Na_v channel conductivity. (A) *State diagram of a Markov model for the Na_v channel, In this representation, C_{Na1}, C_{Na2}, and C_{Na3} correspond to closed states; O_{Na} signifies an open state; IF_{Na} represents a fast-inactivated state; $I1_{Na}$ and $I2_{Na}$ denote intermediate inactivated states; and IC_{Na2} and IC_{Na3} indicate inactivated closed states.* ***(B)*** *Overlay of APs demonstrating the impact of modifying the rate constant (k) between IF_{Na} and O_{Na}.* ***(C)*** *Depiction of relative changes in APD_{30} and APD_{80} at specified percentages of I_{NaL}. Figure was modified from prior publication* (128).

3.2.3. Activation of LTCC Masks Sex-dependent Repolarization Reserve

The female sex has been acknowledged as an independent risk factor for drug-induced LQTS (148). Ca^{2+} mishandling and the resulting cascade of signaling events in cardiomyocytes, referred to as the 'Ca^{2+} vicious cycle,' have been linked to several cardiac pathophysiologies, including LQTS (149). Increased Ca^{2+} influx has been associated with the prolongation of the electrographic QT interval, potentially leading to cardiac arrhythmias (150). To assess the impact of Ca^{2+} stress in a sex-dependent manner, the pharmacological LTCC agonist, FPL 64176, was utilized. This compound enhances voltage-dependent calcium current, which contributes to AP repolarization (151).

Fig. 24A shows the mapping of APD_{80} in a representative left ventricular epicardial region. It demonstrates that the application of FPL 64176 at a concentration of 250 nM led to the delayed late repolarization of APs in heart slice preparations obtained from both male and female mice. These APs were stimulated with a basic cycle length (BCL) of 200 ms. However, when APDs were quantified after incubation with FPL 64176, it became apparent that a significant prolongation of medium and late repolarization by 30% to 80% occurred exclusively in females, whereas in males, only a subtle tendency towards a repolarization delay was observed (Fig. 24B). APD at 30% repolarization remained unaffected, regardless of gender. These data suggest the existence of a sex-dependent repolarization reserve, which becomes apparent following LTCC activation.

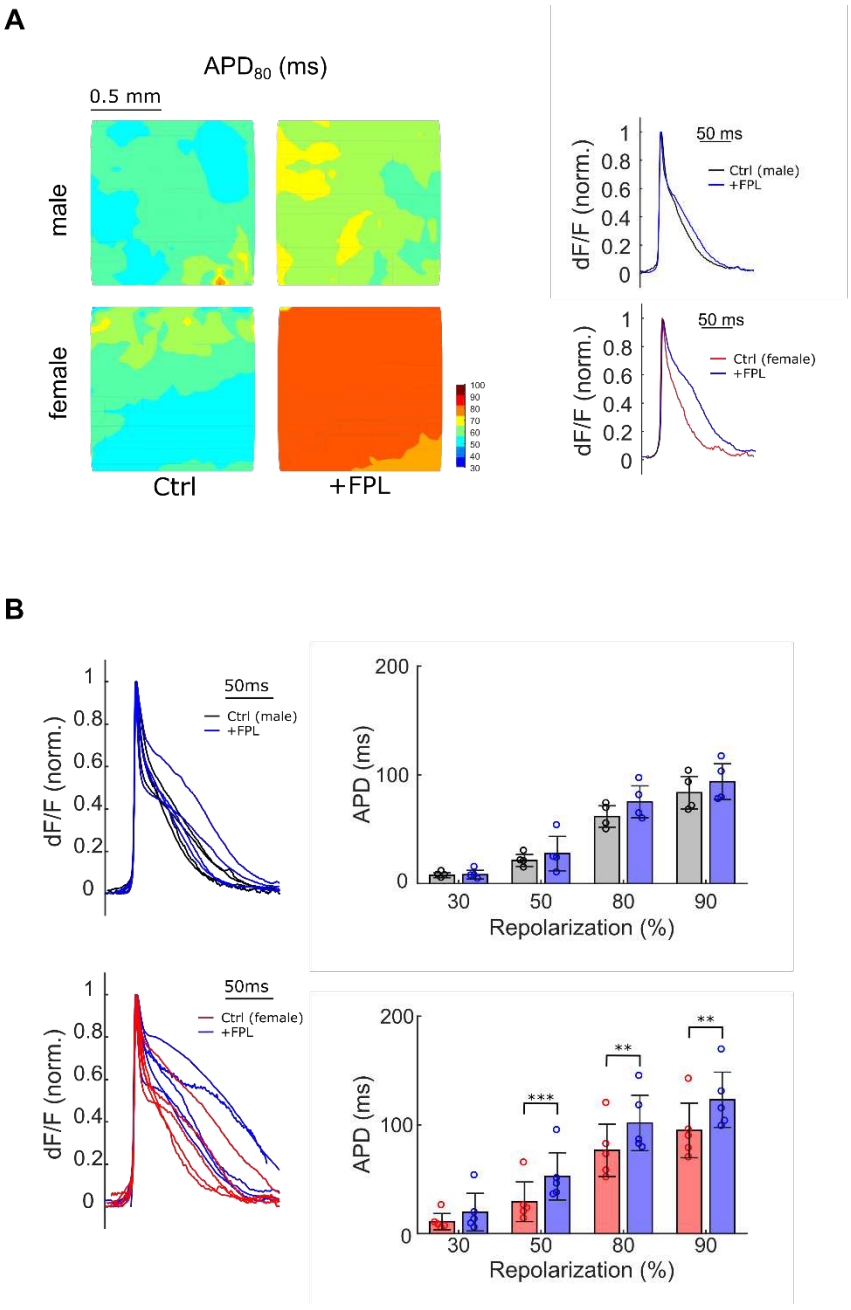

Fig. 15. Sex-specific prolongation of APD induced by LTCC activation. (A) *Optical mapping of APD_{80} in a representative LV region both before and after the administration of the pharmacological LTCC activator FPL 64176 (250 nM) in male (upper) and female (lower) heart slice preparations. An overlay of two representative APs presented in right panel. These APs were generated by averaging the data from all the areas depicted in the left portion, both before and after the application of FPL 64176.* ***(B)*** *Superimposed LV APs from male and female hearts (prior to and following FPL application), along with the quantification of the APD at specified percentages of repolarization (n = 5 slices from N = 5 male mice, n = 5 slices from N = 5 female mice; APD_{50}: p = 0.00077, APD_{80}: p = 0.00623, APD_{90}: p = 0.00899). The color codes represent male (black), female (red), and post-FPL 64176 application (blue). Figure was modified from prior publication* (128). *The Predominant Impact of $I_{Na\text{-}L}$ on AP Repolarization in the Presence of Calcium Stress Revealed by Simulation*

Ultimately, a more in-depth understanding of the experimentally observed sex-dependent variations in repolarization reserve was sought by mathematical modeling. Simulation involved the adjustment of the voltage at which Ca_v channel activation occurs to a more negative level (-15 mV) in single mouse cardiomyocytes, effectively replicating the effects of FPL 64176. The distinct effects of potassium currents (I_{to}, I_{Kur}) and sodium current (I_{NaL}) in terms of sex-specific regulation and their notable contributions to late AP morphology in the model experiments, as reported in part 3.2.2, were evaluated by adjusting their respective current levels. To achieve a specific increase in APD_{80}, the corresponding degree of current modification was calculated.

A 23% reduction in I_{to}, a 21% reduction in I_{Kur}, and a 52% increase in I_{NaL} individually resulted in a 10% prolongation of APD_{80} in the model under baseline conditions. Fig. 25 illustrates that shifting the voltage-dependence of Ca_v channel activation by -15 mV led to a maximum increase in APD_{80} of 40%, which remained unaffected by the additional reductions in I_{to} or I_{Kur}. However, when the I_{NaL} conductivity was increased by 52%, causing a 10% prolongation of APD_{80} under normal Ca_v channel function, it more than doubled APD_{80} when confronted with Ca_v channel overactivation.

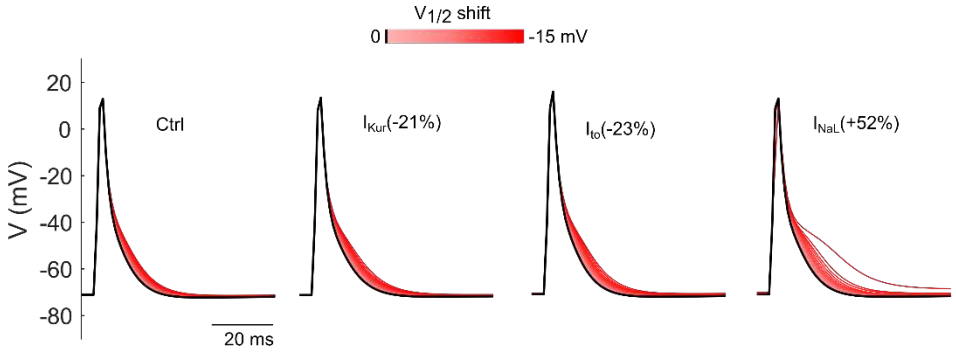

Fig. 16. Simulation of APs in response to a gradual shift in the voltage-dependence of I_{CaL} activation. *The voltage at which half-maximum channel activation ($V_{1/2}$) was altered to more negative values by as much as 15 mV in four distinct conditions: Cntrl (male sex), I_{to} (-23%, reflecting a 23% reduction in g_{to}), I_{Kur} (-21%, reflecting a 21% reduction in g_{Kur}), and I_{NaL} (+52%, indicating a 52% increase in rate constant, k, as depicted in Fig. 23A). Note the delay and variability in late repolarization, particulraly when I_{NaL} is increased. Figure was modified from prior publication* (128).

The potential current contributions to late repolarization behavior in response to an increase in Ca_v channel function are summarized in Fig. 26. Collectively, mathematical modelling highlights the significant role of I_{NaL} in shaping the late AP morphology, particularly under conditions of calcium stress.

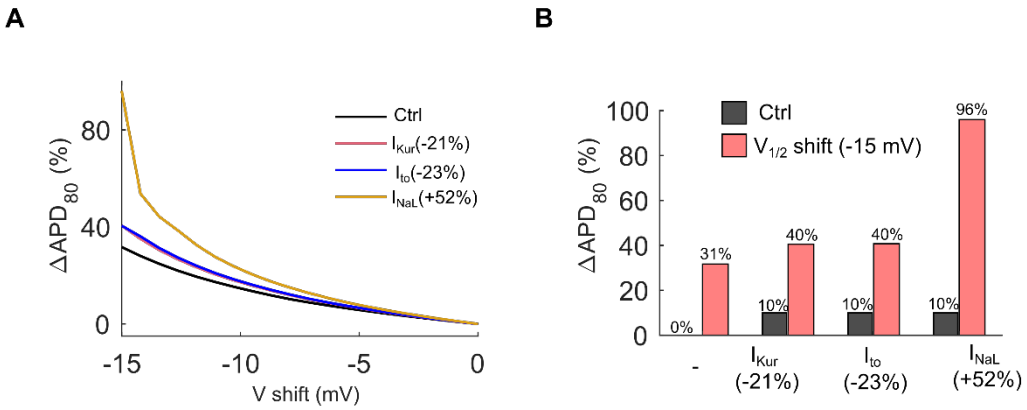

Fig. 17. Mathematical simulation of sex-specific effects of ionic currents on APD during LTCC activation. ***(A)*** *Computation of changes in APD_{80} with the specified adjustment in the voltage-dependence of I_{CaL} activation, considering sex-specific alterations in currents.* ***(B)*** *Alterations in APD_{80} resulting from the indicated sex-specific adjustments in currents, both with (red) and without (gray) a 15 mV shift in $V_{1/2}$ of I_{CaL} to negative values.*

3.3. Exploring the Effect of IGF-1 in Modulating HCN4 Channels

3.3.1. Effect of IGF-1 on SAN automaticity

To explore the effect of IGF-1, a crucial post-MI protein regulator, on the spontaneous beating frequency in the SAN, changes in the SAN BCL in the presence and absence of IGF-1 were quantified. As depicted in Fig. 27A, following a 10-minute incubation of the SAN in 500nM IGF-1, a significant reduction in BCL was observed, with BCL decreasing from 318.00 ± 89.43 ms to 180.8 ± 40.88 ms ($P = 0.0467$, $n = 5$). Conversely, in the absence of IGF-1, following a 10-minute incubation period, BCL displayed a nonsignificant increase, shifting from 317.33 ± 56.28 ms to 328.83 ± 58.45 ms. By performing an unpaired Student's t-Test to compare the IGF-1-incubated group with the Ctrl group, a significant reduction in BCL was calculated, emphasizing the pronounced effect of IGF-1 on the modulation of the spontaneous beating frequency in the SAN ($P = 0.001$, $n = 6$).

Following the quantification of SAN BCL changes in response to IGF-1, a visual representation was included in Fig. 27B. This figure shows a representative activation map and concurrent SAN AP recordings taken before and after the introduction of 500nM IGF-1 to the solution. The activation map indicates the spatial distribution of electrical activity, with the SAN's specific location marked by a white asterisk (*), and a white box outlined the selected region for AP measurement. These visual elements reveal the dynamic alterations in the SAN's spontaneous beating frequency, contributing to a deeper understanding of the influence of IGF-1 on cardiac electrophysiology.

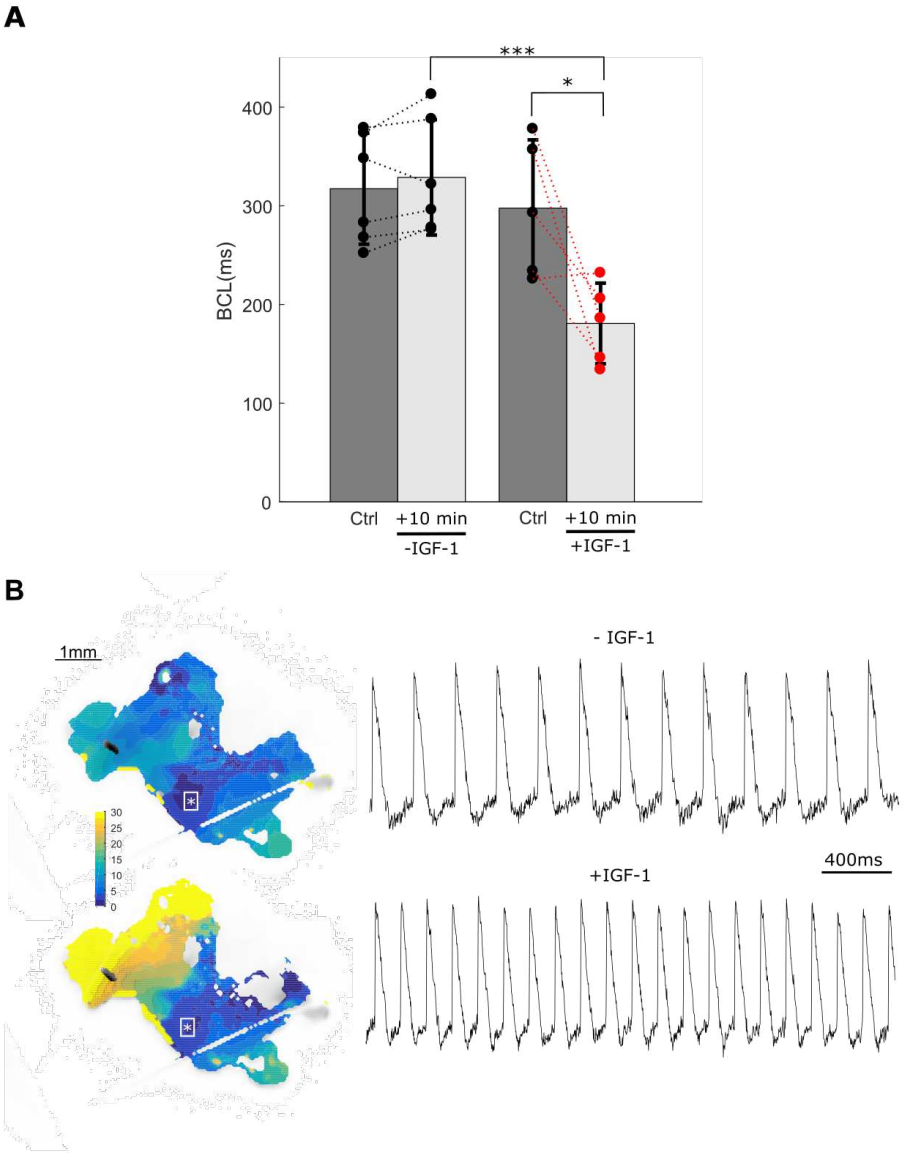

Fig. 18. The impact of IGF-1 on the spontaneous beating rate of the SAN (A) *Quantification of SAN BCL changes in the presence and absence of IGF-1. Statistical analysis involved paired Student's t-Test (* P = 0.0467, n = 5) and unpaired Student's t-Test (*** P = 0.001, n = 6).* ***(B)*** *A representative activation map and corresponding SAN AP recorded before and after the addition of 500nM IGF-1. The position of the SAN is indicated by a white asterisk (*) on the activation map, and the white box denotes the selected region for AP analysis.*

3.3.2. Impact of SC79, an AKT Activator, on SAN Firing Rate

The study's next phase aimed to investigate whether IGF-1's impact on the SAN occurs through the AKT signaling pathway, aligning with prior observations by Reinartz et al., who identified AKT as a downstream component of the IGF-1 signaling cascade

(120). To explore this hypothesis, SC79, a known activator of AKT, was introduced as an alternative to IGF-1. The primary objective was to determine whether SC79 elicited a response similar to IGF-1, thereby suggesting a shared mechanism of action through the AKT pathway.

However, as demonstrated in Fig. 28A, SC79 did not induce a significant reduction in SAN BCL when compared to Ctrl group (unpaired t-test $P = 0.5753$, $n = 4$), unlike IGF-1. While a significant difference was observed within the SC79 treated group between measurements taken prior to and after the application of 50µM SC79 (paired Student's t-Test $P = 0.0171$, $n = 4$), it is noteworthy that, in contrast to IGF-1, the BCL did not decrease but rather exhibited an increase. In Fig. 28B, the representative activation map and selected AP from the SAN region before and after the application of 50µM SC79 are illustrated, highlighting the observed increase in BCL. This observation indicates the presence of distinct regulatory mechanisms, implying that the influence of IGF-1 on the SAN may not be solely mediated by the AKT signaling cascade. These findings contribute to a more comprehensive understanding of the intricate signaling pathways governing the electrophysiological dynamics of the SAN.

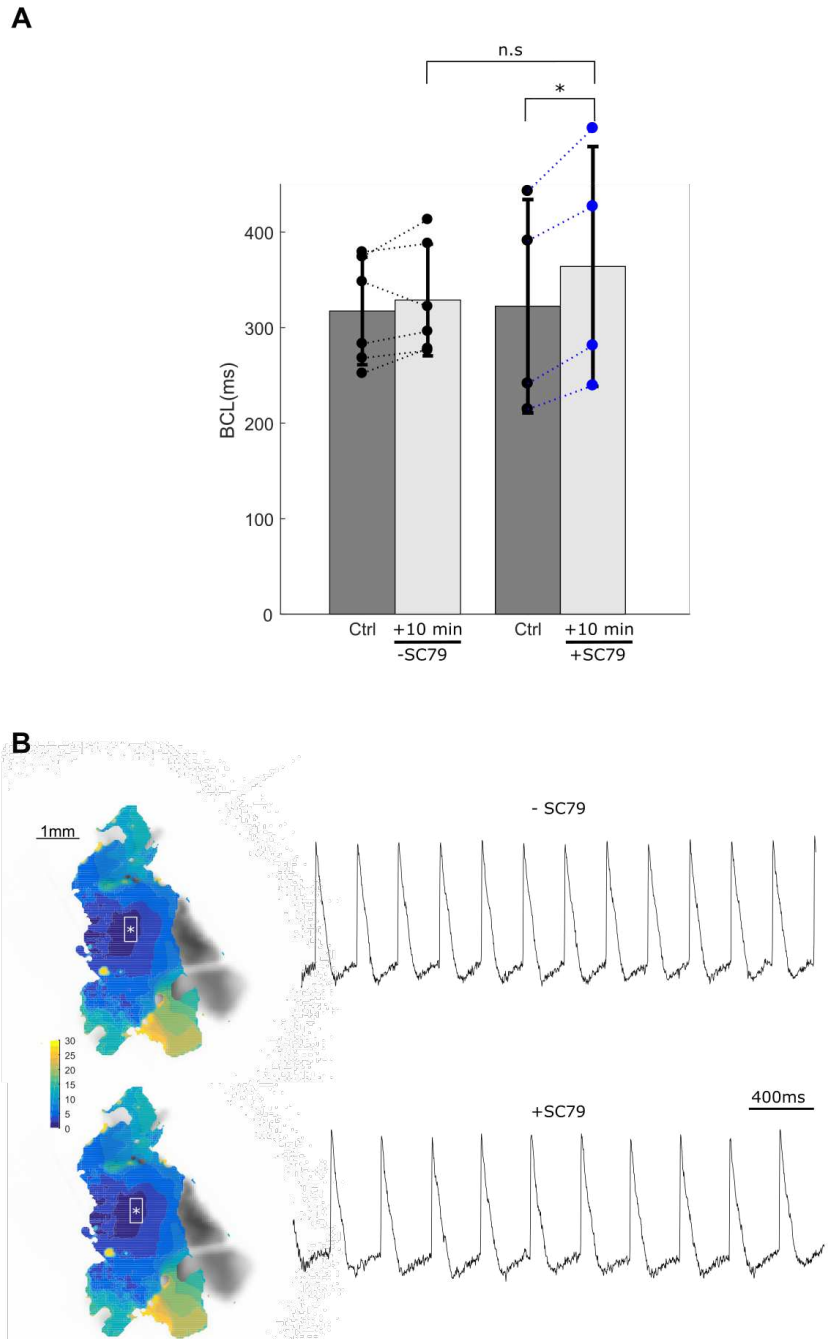

Fig. 19. The Effect of SC79 on the Spontaneous Beating Frequency of the SAN (A) *Quantification of SAN BCL changes in the presence and absence of SC79. Statistical analysis involved paired Student's t-Test (* p = 0.0171, n = 4) and unpaired Student's t-Test (n.s., p = 0.5753, n = 4).* ***(B)*** *An illustrative activation map and corresponding AP of the SAN recorded before and after the introduction of 50µM SC79. The position of the SAN is marked with a white asterisk (*) on the activation map, and a white box outlines the selected area for AP measurement.*

4. Discussion

Normal cardiac function relies on the ability of the heart to distribute electrical signals effectively throughout its structure. However, irregularities in electrophysiological behavior, often linked to cardiac pathophysiology, may contribute to arrhythmias, potentially resulting in SCD. Understanding the spatial dispersion of AP repolarization after I/R injury remains a challenging endeavor (152). This challenge is partly rooted in the variability of definitions for infarct, border, and remote zones, which are significantly influenced by specific experimental conditions and methodology, and the choice of animal species (135,153–156).

To address these uncertainties, researchers have sought an unbiased approach to connect post-I/R electrical changes with high-resolution structural alterations (157). In this study, the problem was tackled by introducing a multi-modal optical mapping approach applied to transversely sectioned mouse heart slices. Besides providing access to a wide range of genetic models for mechanistic exploration, the mouse heart offers a unique opportunity to comprehensively examine both functional and structural adaptations following I/R. This level of detailed analysis is often more challenging to achieve in larger animal species.

To the best of current knowledge, this study represents a pioneering effort to comprehensively investigate early post-I/R transmural AP variations, including their alignment with the infarcted region, as indicated by TTC staining, and their correlation with the regulation of ion channel genes, as detected by *in situ* hybridization.

Under control conditions, the distribution of APD in murine LV transversal slices is generally uniform, displaying a slightly quicker repolarization in the epicardium compared to the endocardium. This transmural gradient in APD has been documented in various studies across different species (158–161). However, following I/R injury, the results presented in this thesis disclose the emergence of an early repolarization shoulder in the AP. This shoulder exclusively appears at epicardial locations near the infarcted area. The recurrent occurrence of AP alternans at these sites validates the notable malfunction in AP repolarization.

Furthermore, the transmural gradient in APD is reversed after I/R injury. Such reversal potentially supports the distinctive inversion of the T-wave observed in surface electrocardiograms, often regarded as a clinical indicator of MI (162,163). This understanding gains substantial support from a simulation study, which predicts that leveling, and particularly reversing, transmural AP heterogeneity will alter the sequence of repolarization from epicardium to endocardium, eventually inverting T-wave orientation (152).

Recent advances in "omics technologies" have enabled a comprehensive survey of gene and protein regulation in cardiovascular disease (164). Examination of these databases led to the formulation of a hypothesis suggesting the potential re-expression of LTCC Cacna1D and its corresponding protein $Ca_V1.3$ in adult ventricles post-ischemia (102,139,165). By application of *in situ* hybridization, the confirmation of *de novo* expression of Cacna1D in cardiomyocytes could be achieved, particularly within regions exhibiting delays in early AP repolarization. This investigation was extended to mathematical modeling, offering a rationale to causatively associate ion channel regulation with the observed electrical remodeling processes in I/R slices. The incorporation of $Ca_V1.3$ into a mouse ventricular single-cell model reliably predicted the outcomes of optical mapping on membrane voltage in the proximity of the infarcted area. Additionally, the model predicted the formation of EADs and repolarization failures due to an isoform transition from $Ca_V1.2$ to $Ca_V1.3$. Such transition may provide the arrhythmogenic substrate for ectopic beats and reentrant tachycardias, which are often seen in ischemic heart disease (90).

The emerging use of optical technologies in tissue slices has proven to be highly valuable as experimental tools (125,166–169). Within this study's framework, experimental evidence is provided, demonstrating that adult heart tissue slices remain viable and electrically stable over hours. This characteristic makes them an ideal 2D myocardium model system for studying the effects of pharmacological substances. Exploiting these adaptable techniques, the impact of gradual LTCC activation by FPL 64176 on APD prolongation is demonstrated in this study.

Remarkably, a gain in LTCC function induced EAD formation and repolarization failure, aligning with predictions made by mathematical modeling of *de novo* $Ca_V1.3$

expression. Subsequently, the hypothesis was reliably confirmed through calcium channel blockage by diltiazem, which not only eliminated the observed AP shoulder but also reduced spatial repolarization dispersion in post-I/R tissue slices. Given the acknowledged transcriptional cross-talk between the two LTCC genes Cacna1C and Cacna1D during development (170), it is proposed that such cross-talk occurs in the vicinity of infarcted regions.

The remodeling of the LTCC isoform profile from $Ca_V1.2$ to $Ca_V1.3$ post-I/R contributes to an increased LTCC function. This elevation can be attributed to the distinctive gating characteristics of $Ca_V1.3$, which features a more negative activation voltage and slower inactivation kinetics in comparison to $Ca_V1.2$ (101,141). Consequently, the observed shift in isoform expression is involved in the increased LTCC activity, providing a detailed understanding of the functional changes following I/R. Despite previous reports indicating a decrease in LTCC currents acutely after ischemia due to lowered pH (90), our results are in good agreement with the described changes in LTCC function over a more extended post-ischemic timeframe. Cardiomyocytes isolated from patients enduring chronic ischemic cardiomyopathy manifest hyperactive LTCC (171), and a machine learning analysis of monophasic AP in patients diagnosed with coronary artery disease suggests larger LTCC currents in cases with recurrent VA (172). Additionally, a deletion of exon-33 in $Ca_V1.2$ detected in MI surviving rat myocytes, results in a gain of function and VA (173). Existing evidence points to the regulation of voltage sensitivity of LTCCs by the S3–S4 linker in domain IV (containing exon-33) (174), and notably, $Ca_V1.3$ lacks the corresponding sequence of exon-33 in $Ca_V1.2$, potentially explaining the negative shift in voltage-dependent activation. (Fig. 29)

The elucidation of molecular mechanisms underlying cardiac electrical disturbances has gained significant attention in recent years. However, precisely identifying the molecular, structural, and functional remodeling processes at spatiotemporal resolution remains challenging. The development of methods to relate loco-regional ion channel expression with electrical dysfunction becomes fundamental for exploring arrhythmogenic mechanisms and serves to identify potential therapeutic targets. The

multi-modal analysis presented in this thesis offers an integrated tool to enhance understanding of heart rhythm disturbances following I/R injury.

Given the relatively low membrane conductance of cardiomyocytes during the initial repolarization phase of the cardiac AP, even minor adjustments in net transmembrane current can significantly impact the APD and facilitate the generation of EAD. Inhibiting currents associated with the sodium/calcium exchanger (I_{NCX}) and the I_{NaL} has been shown to mitigate EAD formation, while reductions in potassium ion conductances may exacerbate it. Despite the focus on remodeling LTCC isoforms, the study does not exclude the potential involvement of other ion channel or transporter dysfunction in EAD formation post-I/R.

Acknowledging certain limitations inherent in this study, it is noted that the absence of specific pharmacological channel modulators and challenges associated with targeting cardiac Cacna1D restricted the feasibility of causative experiments to establish a direct link between AP morphology and $Ca_V1.3$ expression. Additionally, the observation of AP prolongation in later repolarization phases, indicative of diminished potassium conductances, was not explicitly addressed in the present study. It is also crucial to recognize that slicing cardiac tissue disrupts cardiomyocyte alignments oblique to the cutting direction, potentially introducing conduction inhomogeneities and complicating the comparison of conduction velocities across preparations.

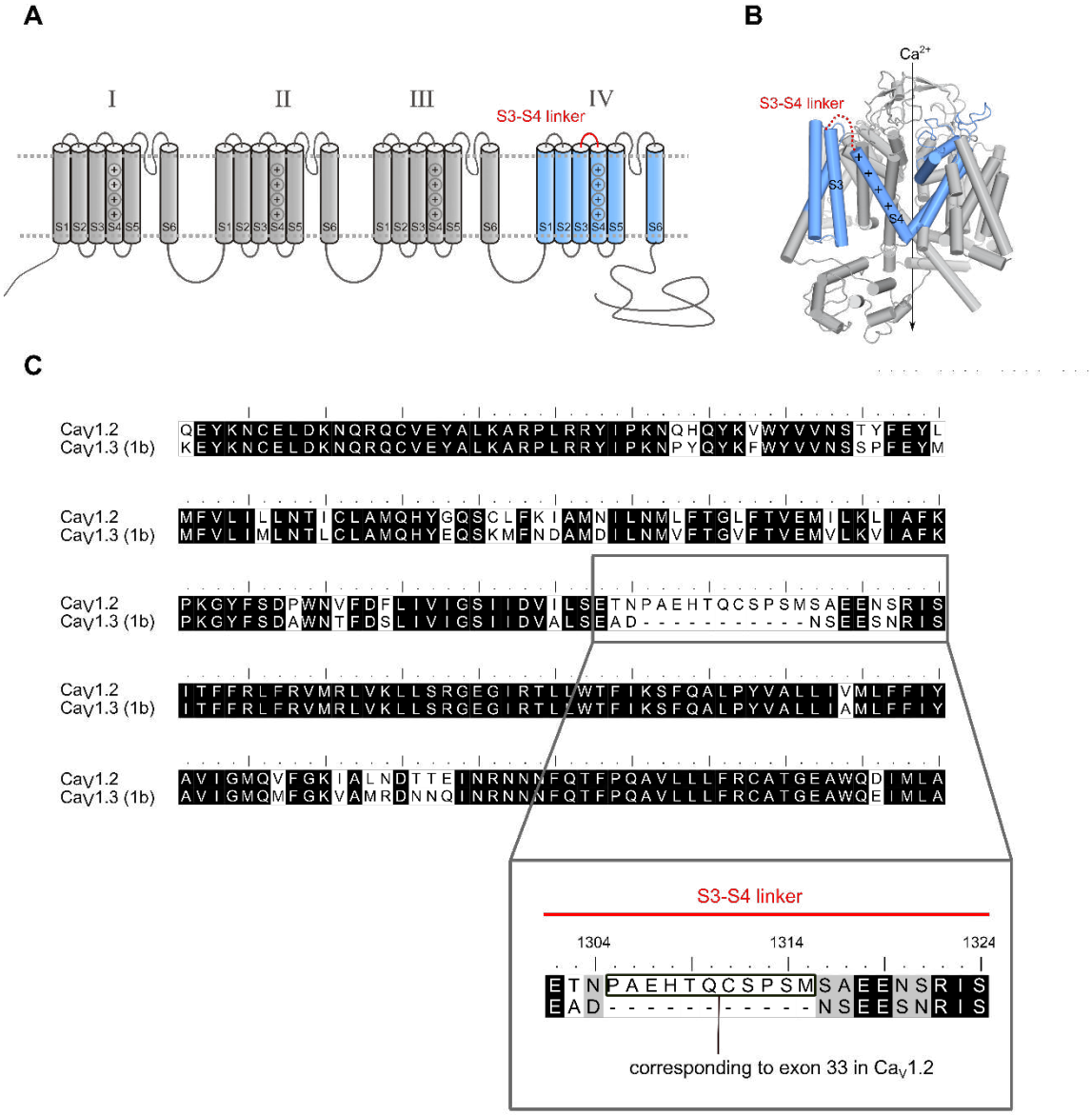

Fig. 29. Alignment of amino acid sequences in the S3-S4 linker of segment IV in cardiac Cav1 channels. ***(A)*** *Illustration of the membrane topology of Ca_V1 channels, encompassing four repeats (I – IV) of six transmembrane helices.* ***(B)*** *Structural depiction of $Ca_V1.1$ (PDB code: 6JPB) highlighting the presumed conformational arrangement of transmembrane helices and the position of the S3-S4 linker in segment IV.* ***(C)*** *Amino acid sequence alignment of $Ca_V1.2$ (uniprot entry code: Q01815; 1175-1424 aa) and $Ca_V1.3$(1b) (uniprot entry code: Q99246-4; 1183-1421 aa) indicates the absence of specific exon 33 amino acids in the S3-S4 linker of $Ca_V1.3$ compared to the isoform $Ca_V1.2$.*

Sex-specific variations in cardiac AP morphology have been documented and are widely acknowledged to be caused, among others, by variations in ion channel regulation. Nonetheless, the majority of studies investigating sex-dependent expression

and function of cardiac ion channels have been conducted on isolated cardiomyocytes. This has resulted in the lack of the spatial context necessary for accurate male-female comparisons and may contribute to functionally relevant heterogeneity between the sexes (175,176). The present study highlights the use of optical mapping for membrane voltage in a mouse heart slice preparation, providing a viable approach to discern sex-specific AP heterogeneity at high spatial resolution. By integration of this method into mathematical modeling, hypotheses are formulated to elucidate how the observed heterogeneity in AP morphology may correlate with respective single current densities in cardiomyocytes.

The current study uncovers notable sex-specific differences in AP repolarization within the epicardial regions of the LV, revealing prolonged APD during late repolarization in female mice compared to their male counterparts. Consequently, the transmural gradient in late APD, observed in male mice, levels off in female mice, indicating distinct sex-specific patterns of transmural heterogeneity. These findings align well with human electrographic studies demonstrating a larger T peak - T end interval in men compared to women (177).

Furthermore, the present study emphasizes a significantly higher degree of interindividual variability in both AP and APD gradients in female mice, potentially attributed to menstrual stages, although these were not implemented in this investigation. Additionally, structural heterogeneity, such as lipid or collagen deposition, may contribute to varying ion channel expression patterns both within and between individuals. In examining the sex-specificity of cardiac APs, factors like hormonal state and age emerge as key considerations in understanding the observed variations (58–63,178,179).

It is important to note the considerable variance in reported APD parameters in isolated cells (Fig. 30, Table 6), likely reflecting uncontrolled methodological and spatial determinants. By employing a heart slice preparation that maintains a more physiological cell composite, our study robustly confirms both prolonged epicardial APD and increased APD variance in female mice compared to males.

Table 6. Literature-Based Comparison of AP Parameters in Males and Females

Strain	Location	APD_{20} (ms)		APD_{50} (ms)		APD_{90} (ms)		BCL (ms)	Reference
		M	F	M	F	M	F		
CD1	V	2.7±0.2	4.2±0.4	4.4±0.3	9.2±1.3	14.8±1	22.7±2.1	250	(58)
C57BL/6 H/H	V	-	-	6.2+0.5	9.3+0.8	23.3+ 1.8	35.2+2.7	500	(62)
C57BL/6	RV	-	-	3.11±0.2	5.21±0.8	12.52±1.2	29.53±6.2	-	(63)
C57BL/6	LV	-	-	11±2 8±2	12±2 15±3	47±7 42±9	54±5 63±6	3000 1000	(60)
C57BL/6	septum	-	-	3.7±0.3	5.7±0.9	29.7±5.2	30.7±4.5	1000 333	(59)
CD1	V	3±n.r.	-	4± n.r.	-	12.7±1.2	-	1000	(180)
C57BL/6	V	3.1±0.1	-	9.0±0.6	-	37.1±2.7	-	1000	(181)
C57BL/6	LV	-	-	-	-	56.8±7.3	-	1000	(182)
C57BL/6	RV	-	-	-	-	79.3±0.6	-	1000	(183)
ICR	LV tissue	-	-	5.9±1.7	-	49±12 69±9.7[a]	-	111-200	(159)
C57BL/6	LV	-	-	-	-	36±3	-	1000	(184)
C57BL/6	LV tissue	-	-	-	-	67.4±2.7	-	200	(185)

Abbrevations: M:male, F:female, n.r: not reported, V:ventricle, LV:left ventricle, RV: right ventricle. [a] after contractile uncoupling. The content of this figure remains unchanged from its original publication (128).

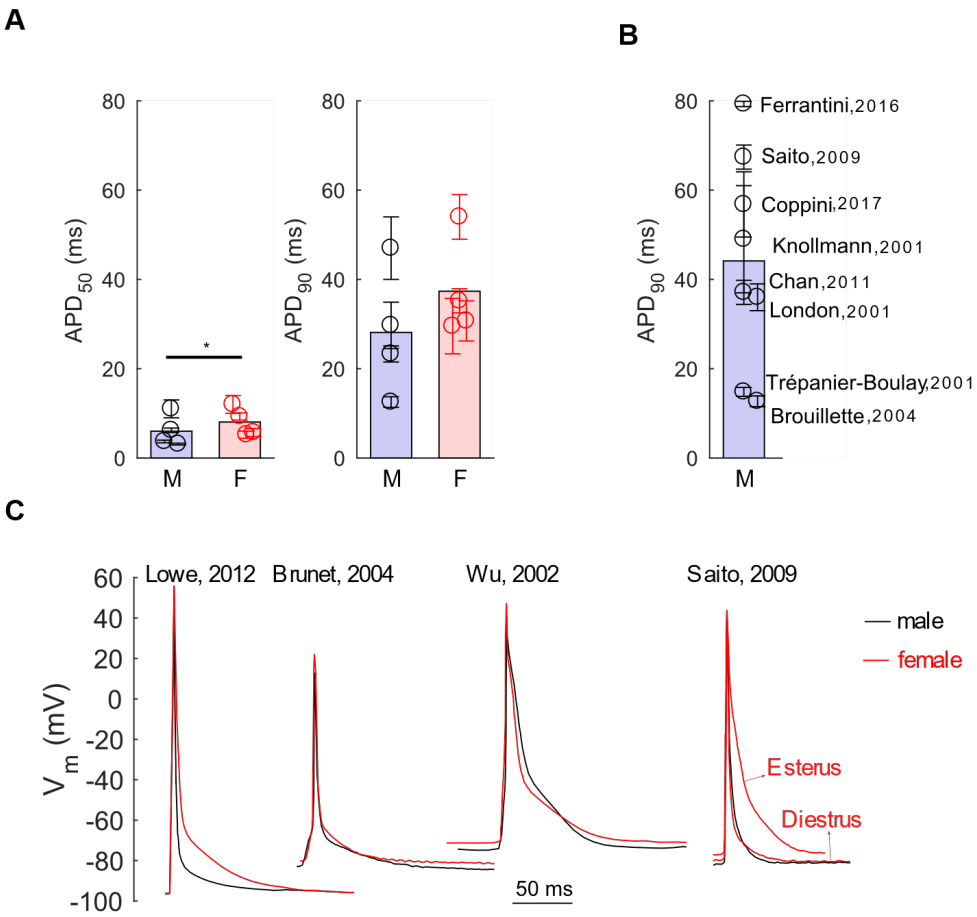

Fig. 30. Digitalization of published data illustrating sex differences in mouse ventricular APs. *In* ***(A)****, quantification of* APD_{50} *and* APD_{90} *from digitally extracted male and female APs across various studies is depicted. Significantly, an unpaired t-test revealed a notable difference in* APD_{50} *(p=0.0174, N=4).* ***(B)*** *Depicts* APD_{90} *values of individual male mice.* ***(C)*** *Presents an overlay of APs as shown in (A). The digitalization of APs from literature was performed using WebPlotDigitizer version 4.5. Figure was modified from prior publication* (128).

The cardiac AP is the result of a complex, voltage-dependent interaction involving various ionic currents that depolarize and repolarize the resting membrane potential. Therefore, alterations in AP morphology indicate changes in the underlying ionic currents. Recent studies on isolated cardiomyocytes have investigated the genetic or functional regulation of several candidate currents to elucidate differences in the cardiac AP between male and female mice. Nevertheless, inconsistencies are prevalent in the existing literature.

For example, multiple reports suggest a decrease in the I_{Kur} in female mouse ventricles, leading to a comprehensible prolongation of the APD (58,59,63,64). Conversely, other studies portray I_{Kur} as either similar to or even greater than that in male mice (60,61,178). As highlighted earlier, factors such as sex hormonal state or spatial context may contribute to conflicting reports on sex-dependent I_{Kur} expression. On a more robust note, there is consistent evidence supporting a lower density of the I_{to} in females (59,63,64). The ion channel alpha-subunits $K_V4.2$ and $K_V4.3$, responsible for I_{to}, have been observed to be less expressed in females compared to males.

It is crucial to emphasize that the functionality of most ion channels stems from intricate multi-protein complexes. This functionality is shaped not solely by the gene or protein expression of the pore-lining subunits but also by auxiliary subunits and diverse post-translational modifications, which intricately influence channel numbers on the cell surface and their gating properties (186).

Interestingly, the beta-subunit KCNE4 exerts modulatory control over both I_{Kur} and I_{to} functions (64). Among the sex-specific ionic currents, the I_{NaL} exhibits a noteworthy increase in females compared to males, especially under specific activation conditions (62). Through mathematical modeling of mouse cardiomyocyte electrophysiology, the quantitative impact of each predominant ionic current on AP morphology was demonstrated. Under physiological conditions, it is proposed that I_{to} influences both early and late repolarization, while I_{Kur} and, to a lesser extent, I_{NaL} are specifically identified as contributors to late repolarization. Conversely, currents such as I_{Kss}, I_{Kr}, and I_{Ks} are unlikely to substantially contribute to sex-specific AP morphology in mice due to their relatively negligible densities. It is crucial to acknowledge that although not considered in the model, post-translational regulation of these currents may indeed alter their contribution (187,188).

Next, the evaluation of sex-specific AP morphology in response to modified Ca^{2+} flux into cardiomyocytes was pursued. In numerous cardiac pathophysiologies, such as hypertrophy and Long-QT syndromes, heightened Ca^{2+} influx assumes a pivotal role (189–191). This is often associated with a shift in voltage-dependent activation of I_{CaL} towards more negative potentials, amplifying I_{CaL} window current, which prolongs the APD and fosters the occurrence of EAD (192). The study demonstrated that the response

in AP morphology to pharmacological activation of I_{CaL} is sex-specific, with females exhibiting a more pronounced APD prolongation. This observation is presumably attributable to differential expression of I_{CaL} density. In female rats and dogs, cardiomyocytes display elevated Ca^{2+} channel densities, resulting in greater I_{Ca} than in cardiomyocytes from their male counterparts (63,193,194). However, for mice, it was observed that only reduced levels of estrogen are linked to an increased number of cardiac LTCCs (195). Based on simulation experiments augmenting window I_{CaL}, an influential role for I_{NaL} in shaping the sex-specific response of AP morphology is suggested. Among the determinants specified earlier for female APD prolongation in mice, I_{NaL} distinctly stands out in delaying APD_{80} in response to enhanced Ca^{2+} influx. Considering significant differences in the spatial expression of cardiac ion channels between mice and humans, it implies a notable contribution of I_{NaL} in drug-induced LQTS, a phenomenon more prevalent in women than in men (148).

It is noteworthy that, in addition to ion channels, ion transporters may exhibit sex-specific expression, thereby influencing cardiac electrophysiology in a sex-specific manner (196,197). Consequently, under conditions of elevated intracellular Ca^{2+} concentrations and subsequent formation of EADs, the potential involvement of the sodium/calcium exchanger NCX should be considered (198).

Several limitations are inherent in our study and warrant attention. The presently available mathematical models of single mouse ventricular myocytes exhibit considerably shorter APDs than those recorded from cardiac tissue. This disparity may be attributed to the absence of mechanical load or mechanical uncoupling agents. Continuous refinement of models based on experimental data is thus not only necessary but also essential for enhancing our quantitative understanding of sex-specific differences in cardiac electrophysiology. This iterative process holds promise for the development of sex-specific models more tailored to specific medical needs.

This study specifically focused on the LV epicardial region due to the abundance of published data on sex-specific ion channel regulation in cardiomyocytes isolated from this area and the availability of a corresponding mathematical model. However, the introduced experimental approach can be generalized to other cardiac regions, including the septum and RV. Transmural slices, with high spatial resolution, offer a tool

to investigate sex-specific intra-heart APD heterogeneity. Such analyses may open new avenues for understanding sex-specific differences in cardiac arrhythmia susceptibility.

Despite the current limitation of concentrating on the sex-specific characterization of membrane voltage in healthy mouse heart slices and post MI hearts, the approach is well-suited to gain comprehensive insight into sex-specific differences in regional remodeling processes (e.g., membrane voltage and calcium signaling) in hypertrophy or other pathophysiological conditions. Looking ahead, both super-resolution microscopic and spatial omics technologies can be seamlessly integrated with the established optical mapping and mathematical modeling approach to test unbiased hypotheses regarding regulated ion channel function in both physiological and pathophysiological conditions.

The investigation into the impact of IGF-1 on the spontaneous beating frequency of the SAN has revealed valuable insights into the intricate regulatory mechanisms governing cardiac electrophysiology. The observed substantial reduction in BCL of SAN from 318.00 ± 89.43 ms to 180.8 ± 40.88 ms after a brief exposure to 500nM IGF-1 underscores the pivotal role of this post-MI protein regulator in dynamically modulating cardiac activity. Such reduction in BCL, indicative of an increase in the firing frequency, is in agreement with the known role of HCN4 in controlling the "funny current", one of the factors involved in cardiac pacemaking. Moreover, the rapid onset of this effect after only 10 minutes of incubation with IGF-1 suggests alignment with fast modulation systems, such as PTM. Therefore, the observed effect of IGF-1 on the reduction of BCL, possibly mediated through PTM of HCN4, provides a mechanistic insight into how IGF-1 may influence the spontaneous beating frequency of the SAN in the post-MI cardiac environment. While statistical analyses further support the significance of this reduction, indicating a pronounced effect of IGF1 on the SAN, the inclusion of HCN4 in the discussion provides a link to the underlying molecular processes governing this observed phenomenon. This comprehensive understanding contributes to the broader comprehension of post-MI cardiac electrophysiology dynamics.

A subsequent exploration into the involvement of the AKT signaling pathway, using the AKT activator SC79 as an alternative to IGF-1, revealed unexpected findings. In contrast to IGF-1, SC79 did not induce a reduction in BCL of SAN, suggesting that the influence of IGF-1 on SAN beating frequency may not be solely mediated through the

AKT pathway. This unexpected distinction implies the existence of additional, distinct regulatory mechanisms contributing to the observed effects of IGF-1. Alternatively, SC79 may not have yielded the same result due to potential challenges in penetrating the cells and interacting with its receptor, or possibly, variations in dosage levels. To further test the hypothesis that IGF-1 works through the AKT pathway, it is imperative to explore the use of other AKT modulators. By employing different compounds that modulate AKT activity, researchers may discern whether the observed effects are specific to IGF-1 or if they can be replicated with alternative modulators. This approach will provide a more comprehensive understanding of the signaling pathways involved in IGF-1-mediated modulation of SAN beating frequency.

The insights gained from this study have broader implications for understanding cardiac function post-MI and may have therapeutic implications. Further investigations are warranted to elucidate the specific molecular pathways through which IGF-1 exerts its influence on SAN beating frequency, considering potential crosstalk with other signaling cascades.

In conclusion, the results presented in this study shed light on the multifaceted regulatory mechanisms governing the sinuatrial response to IGF-1. The unexpected distinction between IGF-1 and SC79 prompts a reevaluation of the assumed exclusive role of the AKT pathway, paving the way for future research aimed at unraveling the intricacies of IGF-1-mediated modulation of cardiac electrophysiology.

In this thesis, the complex landscape of cardiac electrophysiology post-I/R injury is explored by optical mapping techniques, focusing on transmural AP heterogeneity, ion channel regulation, also considering sex-specific differences. Novel findings include the emergence of an early repolarization shoulder near the infarcted area, transmural APD reversal, and *de novo* expression of Cacna1D, implicating $Ca_V1.3$ in arrhythmogenic substrate formation. While this transmural APD reversal may be pathogenic, it may also depend on biological sex, as this study shows distinct transmural APD gradients in females versus males. The study emphasizes the intricate regulation of ion currents, challenging assumptions about sex-dependent I_{Kur} expression. Additionally, the impact of modified Ca^{2+} flux on AP morphology is explored, revealing sex-specific responses. The investigation concludes with insights into the regulatory role of IGF-1 in the SAN

post-MI, highlighting unexpected distinctions between IGF-1 and the AKT activator SC79. Overall, the study advances our understanding of cardiac electrophysiology, offering insights into pathological conditions and potential therapeutic targets.

5. References

1. Murray CJL, Vos T, Lozano R, Naghavi M, Flaxman AD, Michaud C, et al. Disability-adjusted life years (DALYs) for 291 diseases and injuries in 21 regions, 1990–2010: a systematic analysis for the Global Burden of Disease Study 2010. Lancet [Internet]. 2012 Dec 15 [cited 2023 Aug 1];380(9859):2197–223. Available from: http://www.thelancet.com/article/S0140673612616894/fulltext

2. Saunders-Hastings P, Heong SW, Srichaikul J, Wong HL, Shoaibi A, Chada K, et al. Acute myocardial infarction: Development and application of an ICD-10-CM-based algorithm to a large U.S. healthcare claims-based database. PLoS One [Internet]. 2021 Jul 1 [cited 2023 Jul 31];16(7). Available from: https://pubmed.ncbi.nlm.nih.gov/34197488/

3. Reimer KA, Lowe JE, Rasmussen MM, Jennings RB. The wavefront phenomenon of ischemic cell death. 1. Myocardial infarct size vs duration of coronary occlusion in dogs. Circulation [Internet]. 1977 [cited 2023 Aug 1];56(5):786–94. Available from: https://www.ahajournals.org/doi/abs/10.1161/01.cir.56.5.786

4. Moran AE, Forouzanfar MH, Roth GA, Mensah GA, Ezzati M, Flaxman A, et al. The global burden of ischemic heart disease in 1990 and 2010: The global burden of disease 2010 study. Circulation [Internet]. 2014 Apr 8 [cited 2023 Aug 1];129(14):1493–501. Available from: https://www.ahajournals.org/doi/abs/10.1161/CIRCULATIONAHA.113.004046

5. Velagaleti RS, Vasan RS. Heart Failure in the Twenty-First Century: Is it a Coronary Artery Disease or Hypertension Problem? Cardiol Clin. 2007 Nov 1;25(4):487–95.

6. Lewis EF, Moye LA, Rouleau JL, Sacks FM, Arnold JMO, Warnica JW, et al. Predictors of late development of heart failure in stable survivors of myocardial infarction: The CARE study. J Am Coll Cardiol [Internet]. 2003 Oct 15 [cited 2023 Aug 1];42(8):1446–53. Available from: https://www.jacc.org/doi/10.1016/S0735-1097(03)01057-X

7. DeWood MA, Spores J, Notske R, Mouser LT, Burroughs R, Golden MS, et al. Prevalence of Total Coronary Occlusion during the Early Hours of Transmural Myocardial Infarction. http://dx.doi.org/101056/NEJM198010163031601 [Internet]. 2009 Jun 5 [cited 2023 Aug 1];303(16):897–902. Available from: https://www.nejm.org/doi/full/10.1056/NEJM198010163031601

8. Bentzon JF, Otsuka F, Virmani R, Falk E. Mechanisms of Plaque Formation and Rupture. Circ Res [Internet]. 2014 Jun 19 [cited 2023 Aug 1];114(12):1852–66. Available from: https://www.ahajournals.org/doi/abs/10.1161/CIRCRESAHA.114.302721

9. Jennings RB. Historical Perspective on the Pathology of Myocardial Ischemia/Reperfusion Injury. Circ Res [Internet]. 2013 Aug 2 [cited 2023 Aug 1];113(4):428–38. Available from: https://www.ahajournals.org/doi/abs/10.1161/CIRCRESAHA.113.300987

10. Elliott AC, Smith GL, Eisner DA, Allen DG. Metabolic changes during ischaemia and their role in contractile failure in isolated ferret hearts. J Physiol [Internet]. 1992 Aug 1 [cited 2023 Aug 1];454(1):467–90. Available from: https://onlinelibrary.wiley.com/doi/full/10.1113/jphysiol.1992.sp019274

11. physiology JK-TJ of, 1986 undefined. The effects of inorganic phosphate and creatine phosphate on force production in skinned muscles from rat ventricle. Wiley Online Libr KentishThe J Physiol 1986•Wiley Online Libr [Internet]. 1986 [cited 2023 Aug 1];370:585–604. Available from: https://physoc.onlinelibrary.wiley.com/doi/abs/10.1113/jphysiol.1986.sp015952

12. Solaro RJ, Lee JA, Kentish JC, Allen DG. Effects of acidosis on ventricular muscle from adult and neonatal rats. Circ Res. 1988;63(4):779–87.

13. Steenbergen C, Deleeuw G, Rich T, Williamson JR. Effects of acidosis and ischemia on contractility and intracellular pH of rat heart. Circ Res [Internet]. 1977 [cited 2023 Aug 1];41(6):849–58. Available from: https://www.ahajournals.org/doi/abs/10.1161/01.res.41.6.849

14. Frangogiannis NG. Pathophysiology of Myocardial Infarction. Compr Physiol [Internet]. 2015 Oct 1 [cited 2023 Aug 1];5(4):1841–75. Available from: https://onlinelibrary.wiley.com/doi/full/10.1002/cphy.c150006

15. Bolli R, Marbán E. Molecular and cellular mechanisms of myocardial stunning. Physiol Rev. 1999;79(2):609–34.

16. Sekili S, McCay PB, Li XY, Zughaib M, Sun JZ, Tang L, et al. Direct evidence that the hydroxyl radical plays a pathogenetic role in myocardial “stunning” in the conscious dog and demonstration that stunning can be markedly attenuated without subsequent adverse effects. Circ Res [Internet]. 1993 [cited 2023 Aug 1];73(4):705–23. Available from: https://www.ahajournals.org/doi/abs/10.1161/01.RES.73.4.705

17. Gao WD, Atar D, Liu Y, Perez NG, Murphy AM, Marban E. Role of troponin I proteolysis in the pathogenesis of stunned myocardium. Circ Res. 1997;80(3):393–9.

18. Van Eyk JE, Powers F, Law W, Larue C, Hodges RS, Solaro RJ. Breakdown and release of myofilament proteins during ischemia and ischemia/reperfusion in rat hearts identification of degradation products and effects on the pCa-force relation. Circ Res. 1998 Feb 9;82(2):261–71.

19. Suzuki S, Kaneko M, Chapman DC, Dhalla NS. Alterations in cardiac contractile proteins due to oxygen free radicals. Biochim Biophys Acta - Gen Subj. 1991 May 24;1074(1):95–100.

20. Steenbergen C, Hill ML, Jennings RB. Volume regulation and plasma membrane injury in aerobic, anaerobic, and ischemic myocardium in vitro: Effects of osmotic cell swelling on plasma membrane integrity. Circ Res. 1985;57(6):864–75.

21. Pouleur H. Diastolic dysfunction and myocardial energetics. Eur Heart J [Internet].

1990 Jan 1 [cited 2023 Aug 2];11(suppl_C):30–4. Available from: https://dx.doi.org/10.1093/eurheartj/11.suppl_C.30

22. Kübler W, Spieckermann PG. Regulation of glycolysis in the ischemic and the anoxic myocardium. J Mol Cell Cardiol. 1970 Dec 1;1(4):351–77.

23. Jennings RB, Murry CE, Steenbergen C, Reimer KA. Development of cell injury in sustained acute ischemia. Circulation [Internet]. 1990 Sep 1 [cited 2023 Aug 2];82(3 Suppl):II2-12. Available from: https://europepmc.org/article/med/2394018

24. Burke AP, Virmani R. Pathophysiology of Acute Myocardial Infarction. Med Clin North Am. 2007 Jul 1;91(4):553–72.

25. Frangogiannis NG. Matricellular proteins in cardiac adaptation and disease. Physiol Rev [Internet]. 2012 Apr 1 [cited 2023 Aug 2];92(2):635–88. Available from: https://journals.physiology.org/doi/10.1152/physrev.00008.2011

26. Dobaczewski M, Bujak M, Zymek P, Ren G, Entman ML, Frangogiannis NG. Extracellular matrix remodeling in canine and mouse myocardial infarcts. Cell Tissue Res [Internet]. 2006 Jun 22 [cited 2023 Aug 2];324(3):475–88. Available from: https://link.springer.com/article/10.1007/s00441-005-0144-6

27. Zimmerman SD, Thomas DP, Velleman SG, Li X, Hansen TR, McCormick RJ. Time course of collagen and decorin changes in rat cardiac and skeletal muscle post-MI. Am J Physiol - Hear Circ Physiol [Internet]. 2001 [cited 2023 Aug 2];281(4 50-4):1816–22. Available from: https://journals.physiology.org/doi/10.1152/ajpheart.2001.281.4.H1816

28. Ren G, Michael LH, Entman ML, Frangogiannis NG. Morphological characteristics of the microvasculature in healing myocardial infarcts. J Histochem Cytochem [Internet]. 2002 Jan 1 [cited 2023 Aug 2];50(1):71–9. Available from: https://journals.sagepub.com/doi/full/10.1177/002215540205000108

29. Landmesser U, Engberding N, Bahlmann FH, Schaefer A, Wiencke A, Heineke A, et al. Statin-Induced Improvement of Endothelial Progenitor Cell Mobilization, Myocardial Neovascularization, Left Ventricular Function, and Survival After Experimental Myocardial Infarction Requires Endothelial Nitric Oxide Synthase. Circulation [Internet]. 2004 Oct 5 [cited 2023 Aug 2];110(14):1933–9. Available from: https://www.ahajournals.org/doi/abs/10.1161/01.CIR.0000143232.67642.7A

30. Pfeffer MA, Braunwald E. Ventricular remodeling after myocardial infarction. Experimental observations and clinical implications. Circulation [Internet]. 1990 [cited 2023 Aug 2];81(4):1161–72. Available from: https://www.ahajournals.org/doi/abs/10.1161/01.CIR.81.4.1161

31. St John Sutton M, Lee D, Rouleau JL, Goldman S, Plappert T, Braunwald E, et al. Left Ventricular Remodeling and Ventricular Arrhythmias After Myocardial Infarction. Circulation [Internet]. 2003 May 27 [cited 2023 Aug 2];107(20):2577–82. Available from:

https://www.ahajournals.org/doi/abs/10.1161/01.CIR.0000070420.51787.A8

32. Sutton MSJ, Pfeffer MA, Moye L, Plappert T, Rouleau JL, Lamas G, et al. Cardiovascular Death and Left Ventricular Remodeling Two Years After Myocardial Infarction. Circulation [Internet]. 1997 Nov 18 [cited 2023 Aug 2];96(10):3294–9. Available from: https://www.ahajournals.org/doi/abs/10.1161/01.CIR.96.10.3294

33. Lee WW, Marinelli B, Van Der Laan AM, Sena BF, Gorbatov R, Leuschner F, et al. PET/MRI of Inflammation in Myocardial Infarction. J Am Coll Cardiol [Internet]. 2012 Jan 10 [cited 2023 Aug 2];59(2):153–63. Available from: https://www.jacc.org/doi/10.1016/j.jacc.2011.08.066

34. Frangogiannis NG. The inflammatory response in myocardial injury, repair, and remodelling. Nat Rev Cardiol 2014 115 [Internet]. 2014 Mar 25 [cited 2023 Aug 2];11(5):255–65. Available from: https://www.nature.com/articles/nrcardio.2014.28

35. Frangogiannis NG, Ren G, Dewald O, Zymek P, Haudek S, Koerting A, et al. Critical Role of Endogenous Thrombospondin-1 in Preventing Expansion of Healing Myocardial Infarcts. Circulation [Internet]. 2005 Jun 7 [cited 2023 Aug 2];111(22):2935–42. Available from: https://www.ahajournals.org/doi/abs/10.1161/CIRCULATIONAHA.104.510354

36. Mesirca P, Alig J, Torrente AG, Müller JC, Marger L, Rollin A, et al. Cardiac arrhythmia induced by genetic silencing of 'funny' (f) channels is rescued by GIRK4 inactivation. Nat Commun 2014 51 [Internet]. 2014 Aug 21 [cited 2022 Jul 12];5(1):1–15. Available from: https://www.nature.com/articles/ncomms5664

37. John RM, Tedrow UB, Koplan BA, Albert CM, Epstein LM, Sweeney MO, et al. Ventricular arrhythmias and sudden cardiac death. Lancet [Internet]. 2012 Oct 27 [cited 2023 Jul 25];380(9852):1520–9. Available from: http://www.thelancet.com/article/S0140673612614135/fulltext

38. Fishman GI, Chugh SS, Dimarco JP, Albert CM, Anderson ME, Bonow RO, et al. Sudden Cardiac Death Prediction and Prevention. Circulation [Internet]. 2010 Nov 30 [cited 2023 Jul 25];122(22):2335–48. Available from: https://www.ahajournals.org/doi/abs/10.1161/CIRCULATIONAHA.110.976092

39. Lynge TH, Risgaard B, Banner J, Nielsen JL, Jespersen T, Stampe NK, et al. Nationwide burden of sudden cardiac death: A study of 54,028 deaths in Denmark. Hear Rhythm. 2021 Oct 1;18(10):1657–65.

40. Daoud EG, Weiss R, Bahu M, Knight BP, Bogun F, Goyal R, et al. Effect of an irregular ventricular rhythm on cardiac output. Am J Cardiol. 1996 Dec 15;78(12):1433–6.

41. De Groot SHM, Schoenmakers M, Molenschot MMC, Leunissen JDM, Wellens HJJ, Vos MA. Contractile Adaptations Preserving Cardiac Output Predispose the Hypertrophied Canine Heart to Delayed Afterdepolarization–Dependent Ventricular Arrhythmias. Circulation [Internet]. 2000 Oct 24 [cited 2023 Jul

25];102(17):2145–51. Available from: https://www.ahajournals.org/doi/abs/10.1161/01.CIR.102.17.2145

42. Gillis AM. Atrial Fibrillation and Ventricular Arrhythmias. Circulation [Internet]. 2017 Feb 7 [cited 2023 Jul 25];135(6):593–608. Available from: https://www.ahajournals.org/doi/abs/10.1161/CIRCULATIONAHA.116.025312

43. Gemayel C, Pelliccia A, Thompson PD. Arrhythmogenic right ventricular cardiomyopathy. J Am Coll Cardiol [Internet]. 2001 [cited 2023 Jul 25];38(7):1773–81. Available from: https://www.jacc.org/doi/10.1016/S0735-1097(01)01654-0

44. Hasdemir C, Ulucan C, Yavuzgil O, Yuksel A, Kartal Y, Simsek E, et al. Tachycardia-Induced Cardiomyopathy in Patients With Idiopathic Ventricular Arrhythmias: The Incidence, Clinical and Electrophysiologic Characteristics, and the Predictors. J Cardiovasc Electrophysiol [Internet]. 2011 Jun 1 [cited 2023 Jul 25];22(6):663–8. Available from: https://onlinelibrary.wiley.com/doi/full/10.1111/j.1540-8167.2010.01986.x

45. Ten Tusscher KHWJ, Mourad A, Nash MP, Clayton RH, Bradley CP, Paterson DJ, et al. Organization of ventricular fibrillation in the human heart: experiments and models. Exp Physiol [Internet]. 2009 May 1 [cited 2023 Nov 30];94(5):553–62. Available from: https://onlinelibrary.wiley.com/doi/full/10.1113/expphysiol.2008.044065

46. Jalife J. Ventricular Fibrillation: Mechanisms of Initiation and Maintenance. https://doi.org/101146/annurev.physiol62125 [Internet]. 2003 Nov 28 [cited 2023 Jul 31];62:25–50. Available from: https://www.annualreviews.org/doi/abs/10.1146/annurev.physiol.62.1.25

47. Von Rotz M, Aeschbacher S, Bossard M, Schoen T, Blum S, Schneider S, et al. Risk factors for premature ventricular contractions in young and healthy adults. Heart [Internet]. 2017 May 1 [cited 2023 Jul 31];103(9):702–7. Available from: https://heart.bmj.com/content/103/9/702

48. Cha YM, Lee GK, Klarich KW, Grogan M. Premature Ventricular Contraction-Induced Cardiomyopathy. Circ Arrhythmia Electrophysiol [Internet]. 2012 Feb [cited 2023 Jul 31];5(1):229–36. Available from: https://www.ahajournals.org/doi/abs/10.1161/CIRCEP.111.963348

49. Pellegrini CN, Scheinman MM. Clinical Management of Ventricular Tachycardia. Curr Probl Cardiol. 2010 Sep 1;35(9):453–504.

50. Long B, Koyfman A. Best Clinical Practice: Emergency Medicine Management of Stable Monomorphic Ventricular Tachycardia. J Emerg Med. 2017 Apr 1;52(4):484–92.

51. Nogami A. Purkinje-related Arrhythmias Part II: Polymorphic Ventricular Tachycardia and Ventricular Fibrillation. Pacing Clin Electrophysiol [Internet]. 2011 Aug 1 [cited 2023 Jul 31];34(8):1034–49. Available from: https://onlinelibrary.wiley.com/doi/full/10.1111/j.1540-8159.2011.03145.x

52. Samie FH, Jalife J. Mechanisms underlying ventricular tachycardia and its transition to ventricular fibrillation in the structurally normal heart. Cardiovasc Res [Internet]. 2001 May 1 [cited 2023 Jul 31];50(2):242–50. Available from: https://dx.doi.org/10.1016/S0008-6363(00)00289-3

53. Viskin S. Long QT syndromes and torsade de pointes. Lancet [Internet]. 1999 Nov 6 [cited 2023 Jul 31];354(9190):1625–33. Available from: http://www.thelancet.com/article/S0140673699021078/fulltext

54. Abi-Gerges N, Philp K, Pollard C, Wakefield I, Hammond TG, Valentin JP. Sex differences in ventricular repolarization: from cardiac electrophysiology to Torsades de Pointes. Fundam Clin Pharmacol [Internet]. 2004 Apr [cited 2022 Aug 30];18(2):139–51. Available from: https://pubmed.ncbi.nlm.nih.gov/15066127/

55. Locati EH, Zareba W, Moss AJ, Schwartz PJ, Michael Vincent G, Lehmann MH, et al. Age- and Sex-Related Differences in Clinical Manifestations in Patients With Congenital Long-QT Syndrome. Circulation [Internet]. 1998 Jun 9 [cited 2022 Aug 30];97(22):2237–44. Available from: https://www.ahajournals.org/doi/abs/10.1161/01.cir.97.22.2237

56. RR M, BS F, RT S, MD M, MH L. Female gender as a risk factor for torsades de pointes associated with cardiovascular drugs. JAMA [Internet]. 1993 Dec 1 [cited 2022 Aug 30];270(21):2590–7. Available from: https://pubmed.ncbi.nlm.nih.gov/8230644/

57. Ebert SN, Liu XKE, Woosley RL. Female gender as a risk factor for drug-induced cardiac arrhythmias: evaluation of clinical and experimental evidence. J women's Heal [Internet]. 1998 [cited 2022 Aug 30];7(5):547–57. Available from: https://pubmed.ncbi.nlm.nih.gov/9650155/

58. Trépanier-Boulay V, St-Michel C, Tremblay A, Fiset C. Gender-Based Differences in Cardiac Repolarization in Mouse Ventricle. Circ Res [Internet]. 2001 Aug 31 [cited 2022 Apr 8];89(5):437–44. Available from: https://www.ahajournals.org/doi/abs/10.1161/hh1701.095644

59. Brunet S, Aimond F, Li H, Guo W, Eldstrom J, Fedida D, et al. Heterogeneous expression of repolarizing, voltage-gated K+ currents in adult mouse ventricles. J Physiol [Internet]. 2004 Aug 1 [cited 2022 Apr 8];559(1):103–20. Available from: https://onlinelibrary.wiley.com/doi/full/10.1113/jphysiol.2004.063347

60. Wu Y, Anderson ME. Reduced repolarization reserve in ventricular myocytes from female mice. Cardiovasc Res [Internet]. 2002 Feb 15 [cited 2022 Apr 8];53(3):763–9. Available from: https://academic.oup.com/cardiovascres/article/53/3/763/331177

61. Brouillette J, Rivard K, Lizotte E, Fiset C. Sex and strain differences in adult mouse cardiac repolarization: Importance of androgens. Cardiovasc Res. 2005;65(1):148–57.

62. Lowe JS, Stroud DM, Yang T, Hall L, Atack TC, Roden DM. Increased late sodium current contributes to long QT-related arrhythmia susceptibility in female mice.

Cardiovasc Res [Internet]. 2012 Aug 1 [cited 2022 Apr 8];95(3):300–7. Available from: https://academic.oup.com/cardiovascres/article/95/3/300/375663

63. Saito T, Ciobotaru A, Bopassa JC, Toro L, Stefani E, Eghbali M. Estrogen contributes to gender differences in mouse ventricular repolarization. Circ Res [Internet]. 2009 Aug 14 [cited 2022 Apr 8];105(4):343–52. Available from: https://www.ahajournals.org/doi/abs/10.1161/CIRCRESAHA.108.190041

64. Crump SM, Hu Z, Kant R, Levy DI, Goldstein SAN, Abbott GW. Kcne4 deletion sex- and age-specifically impairs cardiac repolarization in mice. FASEB J [Internet]. 2016 Jan 1 [cited 2022 Apr 8];30(1):360–9. Available from: https://onlinelibrary.wiley.com/doi/full/10.1096/fj.15-278754

65. Armstrong PW, Gershlick AH, Goldstein P, Wilcox R, Danays T, Lambert Y, et al. Fibrinolysis or Primary PCI in ST-Segment Elevation Myocardial Infarction. N Engl J Med [Internet]. 2013 Apr 11 [cited 2023 Aug 10];368(15):1379–87. Available from: https://www.nejm.org/doi/full/10.1056/NEJMoa1301092

66. Demidova marina M, Smith JG, Höijer CJ, Holmqvist F, Erlinge D, Platonov P g. Prognostic impact of early ventricular fibrillation in patients with ST-elevation myocardial infarction treated with primary PCI. Eur Hear Journal Acute Cardiovasc Care [Internet]. 2012 Dec 1 [cited 2023 Aug 10];1(4):302–11. Available from: https://dx.doi.org/10.1177/2048872612463553

67. Raviele A, Bonso A, Gasparini G, Themistoclakis S. Prophylactic Implantation of Implantable Cardioverter/Defibrillators in Post-Myocardial Infarction Patients. In Springer, Dordrecht; 1998 [cited 2023 Aug 10]. p. 305–10. Available from: https://link.springer.com/chapter/10.1007/978-94-011-5254-9_43

68. Gorenek B, Blomström Lundqvist C, Brugada Terradellas J, Camm AJ, Hindricks G, Huber K, et al. Cardiac arrhythmias in acute coronary syndromes: position paper from the joint EHRA, ACCA, and EAPCI task force. EP Eur [Internet]. 2014 Nov 1 [cited 2023 Aug 8];16(11):1655–73. Available from: https://dx.doi.org/10.1093/europace/euu208

69. Takada T, Shishido K, Hayashi T, Yokota S, Miyashita H, Yokoyama H, et al. Impact of Late Ventricular Arrhythmias on Cardiac Mortality in Patients with Acute Myocardial Infarction. J Interv Cardiol. 2019;2019.

70. Henkel DM, Witt BJ, Gersh BJ, Jacobsen SJ, Weston SA, Meverden RA, et al. Ventricular arrhythmias after acute myocardial infarction: A 20-year community study. Am Heart J. 2006 Apr 1;151(4):806–12.

71. Uretsky BF, Sheahan RG. Primary Prevention of Sudden Cardiac Death in Heart Failure: Will the Solution Be Shocking? J Am Coll Cardiol [Internet]. 1997 Dec [cited 2023 Aug 10];30(7):1589–97. Available from: https://www.jacc.org/doi/10.1016/S0735-1097(97)00361-6

72. Bhar-Amato J, Davies W, Agarwal S. Ventricular Arrhythmia after Acute Myocardial Infarction: 'The Perfect Storm.' Arrhythmia Electrophysiol Rev [Internet]. 2017 Sep 1 [cited 2023 Aug 10];6(3):134. Available from:

/pmc/articles/PMC5610731/

73. Jesel L, Berthon C, Messas N, Lim HS, Girardey M, Marzak H, et al. Ventricular arrhythmias and sudden cardiac arrest in Takotsubo cardiomyopathy: Incidence, predictive factors, and clinical implications. Hear Rhythm. 2018 Aug 1;15(8):1171–8.

74. Mircea AA. Post-myocardial infarction treatment with resiniferatoxin modulates the expression of important genes involved in inflammation, plaque stability and angiogenesis. Discoveries [Internet]. 2023 Mar 30 [cited 2023 Sep 8];11(1):e163. Available from: /pmc/articles/PMC10425609/

75. Arenal Á, Hernández J, Pérez-David E, Rubio-Guivernau JL, Ledesma-Carbayo MJ, Fernández-Avilés F. Do the spatial characteristics of myocardial scar tissue determine the risk of ventricular arrhythmias? Cardiovasc Res [Internet]. 2012 May 1 [cited 2023 Sep 8];94(2):324–32. Available from: https://dx.doi.org/10.1093/cvr/cvs113

76. Carmeliet E. Cardiac ionic currents and acute ischemia: From channels to arrhythmias. Physiol Rev [Internet]. 1999 [cited 2023 Aug 10];79(3):917–1017. Available from: https://journals.physiology.org/doi/10.1152/physrev.1999.79.3.917

77. Kleber AG. Resting membrane potential, extracellular potassium activity, and intracellular sodium activity during acute global ischemia in isolated perfused guinea pig hearts. Circ Res [Internet]. 1983 [cited 2023 Aug 10];52(4):442–50. Available from: https://www.ahajournals.org/doi/abs/10.1161/01.RES.52.4.442

78. Weiss J, Shine KI. Extracellular K+ accumulation during myocardial ischemia in isolated rabbit heart. https://doi.org/101152/ajpheart19822424H619 [Internet]. 1982 [cited 2023 Aug 10];11(4). Available from: https://journals.physiology.org/doi/10.1152/ajpheart.1982.242.4.H619

79. Coraboeuf E, Deroubaix E, Coulombe A. Acidosis-induced abnormal repolarization and repetitive activity in isolated dog Purkinje fibers. J Physiol (Paris) [Internet]. 1980 Jan 1 [cited 2023 Aug 10];76(2):97–106. Available from: https://europepmc.org/article/med/6772764

80. Mountantonakis SE, Park RE, Frankel DS, Hutchinson MD, Dixit S, Cooper J, et al. Relationship Between Voltage Map "Channels" and the Location of Critical Isthmus Sites in Patients With Post-Infarction Cardiomyopathy and Ventricular Tachycardia. J Am Coll Cardiol. 2013 May 21;61(20):2088–95.

81. De Jesus NM, Wang L, Herren AW, Wang J, Shenasa F, Bers DM, et al. Atherosclerosis exacerbates arrhythmia following myocardial infarction: Role of myocardial inflammation. Hear Rhythm. 2015 Jan 1;12(1):169–78.

82. Lindsey ML, Escobar GP, Mukherjee R, Goshorn DK, Sheats NJ, Bruce JA, et al. Matrix Metalloproteinase-7 Affects Connexin-43 Levels, Electrical Conduction, and Survival After Myocardial Infarction. Circulation [Internet]. 2006 Jun 27 [cited 2023 Aug 24];113(25):2919–28. Available from:

https://www.ahajournals.org/doi/abs/10.1161/CIRCULATIONAHA.106.612960

83. Baum JR, Long B, Cabo C, Duffy HS. Myofibroblasts cause heterogeneous Cx43 reduction and are unlikely to be coupled to myocytes in the healing canine infarct. Am J Physiol - Hear Circ Physiol [Internet]. 2012 Feb [cited 2023 Aug 24];302(3):790–800. Available from: https://journals.physiology.org/doi/10.1152/ajpheart.00498.2011

84. Qin D, Zhang ZH, Caref EB, Boutjdir M, Jain P, El-Sherif N. Cellular and Ionic Basis of Arrhythmias in Postinfarction Remodeled Ventricular Myocardium. Circ Res [Internet]. 1996 Sep 1 [cited 2023 Aug 25];79(3):461–73. Available from: https://www.ahajournals.org/doi/abs/10.1161/01.RES.79.3.461

85. de Langen CDJ, de Graeff PA, van Gilst WH, Bel KJ, Herre Kingma J, Wesseling H. Effects of angiotensin II and captopril on inducible sustained ventricular tachycardia two weeks after myocardial infarction in the pig. J Cardiovasc Pharmacol [Internet]. 1989 [cited 2023 Aug 25];13(2):186–91. Available from: https://research.rug.nl/en/publications/effects-of-angiotensin-ii-and-captopril-on-inducible-sustained-ve

86. Myerburg RJ, Kessler KM, Castellanos A. Sudden cardiac death. Structure, function, and time-dependence of risk. Circulation [Internet]. 1992 Jan 1 [cited 2023 Aug 25];85(1 Suppl):I2-10. Available from: https://europepmc.org/article/med/1728501

87. ARONSON RS, MING Z. Cellular mechanisms of arrhythmias in hypertrophied and failing myocardium. Monogr - Am Hear Assoc. 1993;87(6):VII.76-VII.83.

88. Martins JB, Kim W, Marcus ML. Chronic hypertension and left ventricular hypertrophy facilitate induction of sustained ventricular tachycardia in dogs 3 hours after left circumflex coronary artery occlusion. J Am Coll Cardiol. 1989 Nov 1;14(5):1365–73.

89. TenEick RE, Houser SR, Bassett AL. Cardiac Hypertrophy and Altered Cellular Electrical Activity of the Myocardium. 1989 [cited 2023 Aug 25];573–93. Available from: https://link.springer.com/chapter/10.1007/978-1-4613-0873-7_28

90. Nattel S, Maguy A, Le Bouter S, Yeh YH. Arrhythmogenic ion-channel remodeling in the heart: Heart failure, myocardial infarction, and atrial fibrillation. Physiol Rev. 2007;87(2):425–56.

91. Nerbonne JM, Kass RS. Molecular physiology of cardiac repolarization. Physiol Rev [Internet]. 2005 Oct [cited 2023 Aug 28];85(4):1205–53. Available from: https://journals.physiology.org/doi/10.1152/physrev.00002.2005

92. Pinto JMB, Boyden PA. Reduced Inward Rectifying and Increased E-4031-Sensitive K+ Current Density in Arrhythmogenic Subendocardial Purkinje Myocytes from the Infarcted Heart. J Cardiovasc Electrophysiol [Internet]. 1998 Mar 1 [cited 2023 Aug 28];9(3):299–311. Available from: https://onlinelibrary.wiley.com/doi/full/10.1111/j.1540-8167.1998.tb00915.x

93. Lue WM, Boyden PA. Abnormal electrical properties of myocytes from chronically

infarcted canine heart. Alterations in Vmax and the transient outward current. Circulation [Internet]. 1992 [cited 2023 Aug 28];85(3):1175–88. Available from: https://www.ahajournals.org/doi/abs/10.1161/01.CIR.85.3.1175

94. Jiang M, Cabo C, Yao JA, Boyden PA, Tseng GN. Delayed rectifier K currents have reduced amplitudes and altered kinetics in myocytes from infarcted canine ventricle. Cardiovasc Res [Internet]. 2000 Oct 1 [cited 2023 Aug 28];48(1):34–43. Available from: https://dx.doi.org/10.1016/S0008-6363(00)00159-0

95. Liu N, Niu H, Li Y, Zhang C, Zhou Q, Ruan Y, et al. The changes of potassium currents in rabbit ventricle with healed myocardial infarction. J Huazhong Univ Sci Technol - Med Sci [Internet]. 2004 [cited 2023 Aug 28];24(2):128–31. Available from: https://link.springer.com/article/10.1007/BF02885409

96. Dun W, Baba S, Yagi T, Boyden PA. Dynamic remodeling of K+ and Ca2+ currents in cells that survived in the epicardial border zone of canine healed infarcted heart. Am J Physiol Heart Circ Physiol [Internet]. 2004 Sep [cited 2023 Aug 29];287(3):H1046. Available from: /pmc/articles/PMC4289133/

97. Pinto JMB, Yuan F, Wasserlauf BJ, Bassett AL, Myerburg RJ. Regional Gradation of L-Type Calcium Currents in the Feline Heart with a Healed Myocardial Infarct. J Cardiovasc Electrophysiol [Internet]. 1997 May 1 [cited 2023 Aug 29];8(5):548–60. Available from: https://onlinelibrary.wiley.com/doi/full/10.1111/j.1540-8167.1997.tb00823.x

98. Spear JF, Horowitz LN, Hodess AB, MacVaugh IIIrd H, Moore EN. Cellular electrophysiology of human myocardial infarction. 1. Abnormalities of cellular activation. Circulation [Internet]. 1979 [cited 2023 Aug 29];59(2):247–56. Available from: https://www.ahajournals.org/doi/abs/10.1161/01.CIR.59.2.247

99. Janse MJ, Wit AL. Electrophysiological mechanisms of ventricular arrhythmias resulting from myocardial ischemia and infarction. https://doi.org/101152/physrev19896941049 [Internet]. 1989 [cited 2023 Aug 28];69(4):1049–169. Available from: https://journals.physiology.org/doi/10.1152/physrev.1989.69.4.1049

100. Takemura H, Yasui K, Opthof T, Niwa N, Horiba M, Shimizu A, et al. Subtype switching of L-Type Ca 2+ channel from Cav1.3 to Cav1.2 in embryonic murine ventricle. Circ J. 2005;69(11):1405–11.

101. Mangoni ME, Couette B, Bourinet E, Platzer J, Reimer D, Striessnig J, et al. Functional role of L-type Cav1.3 Ca channels in cardiac pacemaker activity. Proc Natl Acad Sci. 2003;100(9):5543–8.

102. Guo Y, Cui L, Jiang S, Zhang A, Jiang S. Proteomics of acute heart failure in a rat post-myocardial infarction model. Mol Med Rep. 2017;16(2):1946–56.

103. Smith LE, White MY. The role of post-translational modifications in acute and chronic cardiovascular disease. PROTEOMICS – Clin Appl [Internet]. 2014 Aug 1 [cited 2023 Aug 29];8(7–8):506–21. Available from: https://onlinelibrary.wiley.com/doi/full/10.1002/prca.201400052

104. Prabakaran S, Lippens G, Steen H, Gunawardena J. Post-translational modification: nature's escape from genetic imprisonment and the basis for dynamic information encoding. Wiley Interdiscip Rev Syst Biol Med [Internet]. 2012 Nov 1 [cited 2023 Aug 29];4(6):565–83. Available from: https://onlinelibrary.wiley.com/doi/full/10.1002/wsbm.1185

105. Huang B, Wang S, Qin D, Boutjdir M, El-Sherif N. Diminished Basal Phosphorylation Level of Phospholamban in the Postinfarction Remodeled Rat Ventricle. Circ Res [Internet]. 1999 Oct 29 [cited 2023 Aug 30];85(9):848–55. Available from: https://www.ahajournals.org/doi/abs/10.1161/01.RES.85.9.848

106. Rozanski GJ, Xu Z. Glutathione and K+ channel remodeling in postinfarction rat heart. Am J Physiol - Hear Circ Physiol [Internet]. 2002 [cited 2023 Aug 30];282(651-6):2346–55. Available from: https://journals.physiology.org/doi/10.1152/ajpheart.00894.2001

107. Fukuda K, Davies SS, Nakajima T, Ong BH, Kupershmidt S, Fessel J, et al. Oxidative Mediated Lipid Peroxidation Recapitulates Proarrhythmic Effects on Cardiac Sodium Channels. Circ Res [Internet]. 2005 Dec 9 [cited 2023 Aug 30];97(12):1262–9. Available from: https://www.ahajournals.org/doi/abs/10.1161/01.RES.0000195844.31466.e9

108. De Meyts P, Whittaker J. Structural biology of insulin and IGF1 receptors: implications for drug design. Nat Rev Drug Discov 2002 110 [Internet]. 2002 Oct [cited 2023 Aug 30];1(10):769–83. Available from: https://www.nature.com/articles/nrd917

109. Troncoso R, Ibarra C, Vicencio JM, Jaimovich E, Lavandero S. New insights into IGF-1 signaling in the heart. Trends Endocrinol Metab. 2014 Mar;25(3):128–37.

110. Opgaard OS, Wang PH. IGF-I is a matter of heart. Growth Horm IGF Res. 2005 Apr 1;15(2):89–94.

111. Ungvari Z, Csiszar A. The Emerging Role of IGF-1 Deficiency in Cardiovascular Aging: Recent Advances. Journals Gerontol Ser A [Internet]. 2012 Jun 1 [cited 2023 Aug 30];67A(6):599–610. Available from: https://dx.doi.org/10.1093/gerona/gls072

112. Troncoso R, Díaz-Elizondo J, Espinoza SP, Navarro-Marquez MF, Oyarzún AP, Riquelme JA, et al. Regulation of cardiac autophagy by insulin-like growth factor 1. IUBMB Life [Internet]. 2013 Jul 1 [cited 2023 Aug 30];65(7):593–601. Available from: https://onlinelibrary.wiley.com/doi/full/10.1002/iub.1172

113. Palmen M, Daemen MJAP, Bronsaer R, Dassen WRM, Zandbergen HR, Kockx M, et al. Cardiac remodeling after myocardial infarction is impaired in IGF-1 deficient mice. Cardiovasc Res [Internet]. 2001 Jun 1 [cited 2023 Aug 29];50(3):516–24. Available from: https://dx.doi.org/10.1016/S0008-6363(01)00237-1

114. Reiss K, Kajstura J, Zhang X, Li P, Szoke E, Olivetti G, et al. Acute Myocardial Infarction Leads to Upregulation of the IGF-1 Autocrine System, DNA Replication, and Nuclear Mitotic Division in the Remaining Viable Cardiac Myocytes. Exp Cell

Res. 1994 Aug 1;213(2):463–72.

115. Ock S, Choi SW, Choi SH, Kang H, Kim SJ, Lee WS, et al. Insulin signaling is critical for sinoatrial node maintenance and function. Exp Mol Med 2023 555 [Internet]. 2023 May 1 [cited 2023 Aug 30];55(5):965–73. Available from: https://www.nature.com/articles/s12276-023-00988-0

116. Stilli D, Sgoifo A, Macchi E, Zaniboni M, De Iasio S, Cerbai E, et al. Myocardial remodeling and arrhythmogenesis in moderate cardiac hypertrophy in rats. Am J Physiol - Hear Circ Physiol [Internet]. 2001 [cited 2023 Aug 30];280(1 49-1). Available from: https://journals.physiology.org/doi/10.1152/ajpheart.2001.280.1.H142

117. Fernández-Velasco M, Goren N, Benito G, Blanco-Rivero J, Boscá L, Delgado C. Regional distribution of hyperpolarization-activated current (If) and hyperpolarization-activated cyclic nucleotide-gated channel mRNA expression in ventricular cells from control and hypertrophied rat hearts. J Physiol [Internet]. 2003 Dec 1 [cited 2023 Aug 30];553(2):395–405. Available from: https://onlinelibrary.wiley.com/doi/full/10.1113/jphysiol.2003.041954

118. Stillitano F, Lonardo G, Zicha S, Varro A, Cerbai E, Mugelli A, et al. Molecular basis of funny current (If) in normal and failing human heart. J Mol Cell Cardiol [Internet]. 2008 [cited 2023 Aug 30];45(2):289–99. Available from: https://pubmed.ncbi.nlm.nih.gov/18556018/

119. Hofmann F, Fabritz L, Stieber J, Schmitt J, Kirchhof P, Ludwig A, et al. Ventricular HCN channels decrease the repolarization reserve in the hypertrophic heart. Cardiovasc Res [Internet]. 2012 [cited 2023 Aug 30];95(3):317–26. Available from: https://pubmed.ncbi.nlm.nih.gov/22652004/

120. Reinartz M, Raupach A, Kaisers W, Gödecke A. AKT1 and AKT2 induce distinct phosphorylation patterns in HL-1 cardiac myocytes. J Proteome Res [Internet]. 2014 Oct 3 [cited 2023 Aug 29];13(10):4232–45. Available from: https://pubs.acs.org/doi/full/10.1021/pr500131g

121. Li Y, Xue Q, Ma J, Zhang CT, Qiu P, Wang L, et al. Effects of imidapril on heterogeneity of action potential and calcium current of ventricular myocytes in infarcted rabbits. Acta Pharmacol Sin [Internet]. 2004 Nov 1 [cited 2023 Sep 5];25(11):1458–63. Available from: http://www.chinaphar.com/1671-4083/25/1458.htm

122. Maltsev VA, Sabbah HN, Undrovinas AI. Down-regulation of sodium current in chronic heart failure: Effect of long-term therapy with carvedilol. Cell Mol Life Sci [Internet]. 2002 Sep [cited 2023 Sep 5];59(9):1561–8. Available from: https://link.springer.com/article/10.1007/s00018-002-8529-0

123. Li X, Huang C, Jiang H, Cao F, Journal TW-C medical, 2005 U. The beta-adrenergic blocker carvedilol restores L-type calcium current in a myocardial infarction model of rabbit. Chinese Med journal, [Internet]. 2005 [cited 2023 Sep 5];118(05):377–82. Available from: https://mednexus.org/doi/abs/10.5555/cmj.0366-6999.118.05.p377.01

124. Heinen A, Nederlof R, Panjwani P, Spychala A, Tschaidse T, Reffelt H, et al. IGF1 Treatment Improves Cardiac Remodeling after Infarction by Targeting Myeloid Cells. Mol Ther [Internet]. 2019 Jan 2 [cited 2023 Sep 6];27(1):46–58. Available from: http://www.cell.com/article/S1525001618305276/fulltext

125. Wang K, Lee P, Mirams GR, Sarathchandra P, Borg TK, Gavaghan DJ, et al. Cardiac tissue slices: Preparation, handling, and successful optical mapping. Am J Physiol - Hear Circ Physiol. 2015;308(9):H1112–25.

126. Lang D, Glukhov A V. High-resolution optical mapping of the mouse sino-atrial node. J Vis Exp [Internet]. 2016 Dec 2 [cited 2023 Oct 10];2016(118). Available from: https://app.jove.com/de/t/54773/high-resolution-optical-mapping-of-the-mouse-sino-atrial-node

127. Gloschat C, Aras K, Gupta S, Faye NR, Zhang H, Syunyaev RA, et al. RHYTHM: An Open Source Imaging Toolkit for Cardiac Panoramic Optical Mapping. Sci Rep. 2018 Dec;8(1):1–12.

128. Moussavi-Torshizi SE, Amin E, Klöcker N. Sex-specific repolarization heterogeneity in mouse left ventricle: Optical mapping combined with mathematical modeling predict the contribution of specific ionic currents. Physiol Rep [Internet]. 2023 Jun 1 [cited 2023 Oct 5];11(11):e15670. Available from: https://onlinelibrary.wiley.com/doi/full/10.14814/phy2.15670

129. Fishbein MC, Meerbaum S, Rit J, Lando U, Kanmatsuse K, Mercier JC, et al. Early phase acute myocardial infarct size quantification: Validation of the triphenyl tetrazolium chloride tissue enzyme staining technique. Am Heart J. 1981 May;101(5):593–600.

130. Wang F, Flanagan J, Su N, Wang LC, Bui S, Nielson A, et al. RNAscope: A novel in situ RNA analysis platform for formalin-fixed, paraffin-embedded tissues. J Mol Diagnostics. 2012;14(1):22–9.

131. Li L, Niederer SA, Idigo W, Zhang YH, Swietach P, Casadei B, et al. A mathematical model of the murine ventricular myocyte: a data-driven biophysically based approach applied to mice overexpressing the canine NCX isoform. AJP Hear Circ Physiol. 2010 Oct;299(4):H1045-63.

132. Pan M, Gawthrop PJ, Cursons J, Tran K, Crampin EJ. The cardiac Na+/K+ ATPase: An updated, thermodynamically consistent model. Physiome. 2020;

133. Petkova-Kirova PS, London B, Salama G, Rasmusson RL, Bondarenko VE. Mathematical modeling mechanisms of arrhythmias in transgenic mouse heart overexpressing TNF-α. Am J Physiol Heart Circ Physiol. 2012 Feb;302(4):H934-52.

134. Mahajan A, Shiferaw Y, Sato D, Baher A, Olcese R, Xie LH, et al. A rabbit ventricular action potential model replicating cardiac dynamics at rapid heart rates. Biophys J. 2008 Jan;94(2):392–410.

135. Myles RC, Burton FL, Cobbe SM, Smith GL. Alternans of action potential duration and amplitude in rabbits with left ventricular dysfunction following myocardial infarction. J Mol Cell Cardiol. 2011 Mar;50(3):510–21.

136. Krogh-Madsen T, Christini DJ. Action potential duration dispersion and alternans in simulated heterogeneous cardiac tissue with a structural barrier. Biophys J [Internet]. 2007 Feb 15 [cited 2023 Dec 1];92(4):1138–49. Available from: http://www.cell.com/article/S0006349507709256/fulltext

137. Issa ZF, Miller JM, Zipes DP. Cardiac Ion Channels. In: Clinical Arrhythmology and Electrophysiology. Elsevier; 2019. p. 15–50.

138. Bers DM, Perez-Reyes E. Ca channels in cardiac myocytes: Structure and function in Ca influx and intracellular Ca release. Cardiovasc Res. 1999 May;42(2):339–60.

139. Srivastava U, Jennings-Charles R, Qu YS, Sossalla S, Chahine M, Boutjdir M. Novel re-expression of L-type calcium channel Cav1.3 in left ventricles of failing human heart. Hear Rhythm [Internet]. 2020 Jul 1 [cited 2022 Mar 31];17(7):1193–7. Available from: http://www.heartrhythmjournal.com/article/S1547527120301764/fulltext

140. Bondarenko VE, Rasmusson RL. Transmural heterogeneity of repolarization and Ca2+ handling in a model of mouse ventricular tissue. Am J Physiol - Hear Circ Physiol. 2010 Aug;299(2):H454-69.

141. Christel CJ, Cardona N, Mesirca P, Herrmann S, Hofmann F, Striessnig J, et al. Distinct localization and modulation of Ca v 1.2 and Ca v 1.3 L-type Ca 2+ channels in mouse sinoatrial node. J Physiol. 2012 Dec;590(24):6327–41.

142. Toyoda F, Mesirca P, Dubel S, Ding W-GG, Striessnig J, Mangoni ME, et al. CaV1.3 L-type Ca2+ channel contributes to the heartbeat by generating a dihydropyridine-sensitive persistent Na+ current. Sci Rep. 2017 Dec;7(1):7869.

143. Fan J-S, Yuan Y, Palade P. Kinetic effects of FPL 64176 on L-type Ca2+ channels in cardiac myocytes. Naunyn-Schmiedeberg's Arch Pharmacol 2000 3615. 2000;361(5):465–76.

144. Vaidya D, Morley GE, Samie FH, Jalife J. Reentry and fibrillation in the mouse heart: A challenge to the critical mass hypothesis. Circ Res. 1999 Jul;85(2):174–81.

145. Lei M, Wu L, Terrar DA, Huang CLH. Modernized classification of cardiac antiarrhythmic drugs. Circulation. 2018;138(17):1879–96.

146. Rodríguez Padial L, Barón-Esquivias G, Hernández Madrid A, Marzal Martín D, Pallarés-Carratalá V, de la Sierra A. Clinical Experience with Diltiazem in the Treatment of Cardiovascular Diseases. Cardiol Ther. 2016 Jun;5(1):75.

147. Bondarenko VE, Szigeti GP, Bett GCL, Kim SJ, Rasmusson RL. Computer model of action potential of mouse ventricular myocytes. Am J Physiol - Hear Circ Physiol [Internet]. 2004 Sep [cited 2023 Oct 17];287(3 56-3):1378–403. Available from: https://journals.physiology.org/doi/10.1152/ajpheart.00185.2003

148. Li G, Cheng G, Wu J, Zhou X, Liu P, Sun C. Drug-induced long qt syndrome in women. Adv Ther [Internet]. 2013 Sep 2 [cited 2023 Oct 26];30(9):793–802. Available from: https://link.springer.com/article/10.1007/s12325-013-0056-x

149. Hegyi B, Pölönen RP, Hellgren KT, Ko CY, Ginsburg KS, Bossuyt J, et al. Cardiomyocyte Na+ and Ca2+ mishandling drives vicious cycle involving CaMKII, ROS, and ryanodine receptors. Basic Res Cardiol [Internet]. 2021 Dec 1 [cited 2023 Oct 26];116(1):1–16. Available from: https://link.springer.com/article/10.1007/s00395-021-00900-9

150. Giudicessi JR, Ackerman MJ. Calcium revisited. Circ Arrhythmia Electrophysiol [Internet]. 2016 Jul 1 [cited 2023 Oct 26];9(7). Available from: https://www.ahajournals.org/doi/abs/10.1161/CIRCEP.116.002480

151. Fan JS, Palade P. Effects of FPL 64176 on Ca transients in voltage-clamped rat venticular myocytes. Br J Pharmacol. 2002;135(6):1495–504.

152. Gima K, Rudy Y. Ionic current basis of electrocardiographic waveforms: A model study. Circ Res. 2002 May;90(8):889–96.

153. Hegyi B, Bossuyt J, Griffiths LG, Shimkunas R, Coulibaly Z, Jian Z, et al. Complex electrophysiological remodeling in postinfarction ischemic heart failure. Proc Natl Acad Sci. 2018;115(13):201718211.

154. Kelemen K, Greener ID, Wan X, Parajuli S, Donahue JK. Heterogeneous repolarization creates ventricular tachycardia circuits in healed myocardial infarction scar. Nat Commun. 2022 Feb;13(1):1–14.

155. Mills WR, Mal N, Forudi F, Popovic ZB, Penn MS, Laurita KR. Optical mapping of late myocardial infarction in rats. Am J Physiol - Hear Circ Physiol. 2006;290(3):1298–306.

156. Wang L, Olivas A, Francis Stuart SD, Tapa S, Blake MR, Woodward WR, et al. Cardiac sympathetic nerve transdifferentiation reduces action potential heterogeneity after myocardial infarction. Am J Physiol Heart Circ Physiol. 2020 Mar;318(3):H558–65.

157. Zhu C, Rajendran PS, Hanna P, Efimov IR, Salama G, Fowlkes CC, et al. High-resolution structure-function mapping of intact hearts reveals altered sympathetic control of infarct border zones. JCI Insight. 2022 Feb;7(3).

158. Anumonwo JMB, Tallini YN, Vetter FJ, Jalife J. Action potential characteristics and arrhythmogenic properties of the cardiac conduction system of the murine heart. Circ Res. 2001 Aug;89(4):329–35.

159. Knollmann BC, Katchman AN, Franz MR. Monophasic action potential recordings from intact mouse heart: Validation, regional heterogeneity, and relation to refractoriness. J Cardiovasc Electrophysiol [Internet]. 2001 [cited 2022 Nov 7];12(11):1286–94. Available from: https://www.mendeley.com/catalogue/33b38ae7-b0bc-3116-9652-cd29349ca17a/?utm_source=desktop&utm_medium=1.19.8&utm_campaign=open_catalog&userDocumentId=%7B231a2d26-9edd-449b-a827-f66e6cfbbe6d%7D

160. Efimov IR, Fedorov V V., Glukhov A, Lou Q, Ambrosi C, Janks D, et al. Multiscale imaging of the human heart: Building the foundation for human systems

physiology and translational medicine. In: 2010 Annual International Conference of the IEEE Engineering in Medicine and Biology Society, EMBC'10. 2010. p. 5177–80.

161. Boukens BJ, Walton R, Meijborg VM, Coronel R. Transmural electrophysiological heterogeneity, the T-wave and ventricular arrhythmias. Prog Biophys Mol Biol. 2016 Dec;122(3):202–14.

162. Channer K, Morris F. ABC of clinical electrocardiography: Myocardial ischaemia. BMJ Br Med J. 2002 Apr;324(7344):1023.

163. Speerschneider T, Thomsen MB. Physiology and analysis of the electrocardiographic T wave in mice. Acta Physiol. 2013 Dec;209(4):262–71.

164. Leon-Mimila P, Wang J, Huertas-Vazquez A. Relevance of Multi-Omics Studies in Cardiovascular Diseases. Front Cardiovasc Med. 2019 Jul;6:91.

165. Binek A, Fernández-Jiménez R, Jorge I, Camafeita E, López JA, Bagwan N, et al. Proteomic footprint of myocardial ischemia/reperfusion injury: Longitudinal study of the at-risk and remote regions in the pig model. Sci Rep. 2017;7(1).

166. Wen Q, Gandhi K, Capel RA, Hao G, O'Shea C, Neagu G, et al. Transverse cardiac slicing and optical imaging for analysis of transmural gradients in membrane potential and Ca2+ transients in murine heart. J Physiol. 2018 Sep;596(17):3951–65.

167. Ripplinger CM. The best thing since sliced bread? Optical mapping of transverse cardiac slices in the mouse heart. J Physiol. 2018 Sep;596(17):3825–6.

168. Kang C, Qiao Y, Li G, Baechle K, Camelliti P, Rentschler S, et al. Human Organotypic Cultured Cardiac Slices: New Platform For High Throughput Preclinical Human Trials. Sci Rep. 2016;6.

169. Halbach M, Pillekamp F, Brockmeier K, Hescheler J, Müller-Ehmsen J, Reppel M. Ventricular Slices of Adult Mouse Hearts - a new Multicellular In Vitro Model for Electrophysiological Studies. Cell Physiol Biochem. 2006;18(1–3):1–8.

170. Xu M, Welling A, Paparisto S, Hofmann F, Klugbauer N. Enhanced Expression of L-type Cav1.3 Calcium Channels in Murine Embryonic Hearts from Cav1.2-deficient Mice. J Biol Chem. 2003;278(42):40837–41.

171. Sanchez-Alonso JL, Schobesberger S, Poulet CE, Bhogal N, Chowdhury R, Gorelik J. Function of L-Type Calcium Channel Microdomain in Human Myocytes from Hearts with Ischemic versus Dilated Cardiomyopathies. Biophys J. 2018;114(3):638a.

172. Rogers AJ, Selvalingam A, Alhusseini MI, Krummen DE, Corrado C, Abuzaid F, et al. Machine Learned Cellular Phenotypes in Cardiomyopathy Predict Sudden Death. Circ Res. 2021 Jan;128:172–84.

173. Lia G, Wang J, Liao P, Bartels P, Zhang H, Yu D, et al. Exclusion of alternative exon 33 of CaV1.2 calcium channels in heart is proarrhythmogenic. Proc Natl Acad Sci

U S A. 2017 May;114(21):E4288–95.

174. Tuluc P, Benedetti B, Costé de Bagneaux P, Grabner M, Flucher BE. Two distinct voltage-sensing domains control voltage sensitivity and kinetics of current activation in Cav1.1 calcium channels. J Gen Physiol. 2016;147(6):437–49.

175. Antzelevitch C, Fish J. Electrical heterogeneity within the ventricular wall. Basic Res Cardiol [Internet]. 2001 [cited 2023 Nov 10];96(6):517–27. Available from: https://link.springer.com/article/10.1007/s003950170002

176. Bartos DC, Grandi E, Ripplinger CM. Ion Channels in the Heart. Compr Physiol [Internet]. 2015 Jul 1 [cited 2023 Nov 10];5(3):1423–64. Available from: https://onlinelibrary.wiley.com/doi/full/10.1002/cphy.c140069

177. Smetana P, Batchvarov V, Hnatkova K, Camm AJ, Malik M. Sex differences in the rate dependence of the T wave descending limb. Cardiovasc Res [Internet]. 2003 Jun 1 [cited 2023 Nov 13];58(3):549–54. Available from: https://dx.doi.org/10.1016/S0008-6363(03)00319-5

178. Brouillette J, Trépanier-Boulay V, Fiset C. Effect of androgen deficiency on mouse ventricular repolarization. J Physiol. 2003 Jan;546(2):403–13.

179. Yusifov A, Chhatre VE, Koplin EK, Wilson CE, Schmitt EE, Woulfe KC, et al. Transcriptomic analysis of cardiac gene expression across the life course in male and female mice. Physiol Rep [Internet]. 2021 Jul 1 [cited 2022 Apr 8];9(13):e14940. Available from: https://onlinelibrary.wiley.com/doi/full/10.14814/phy2.14940

180. Brouillette J, Clark RB, Giles WR, Fiset C. Functional properties of K+ currents in adult mouse ventricular myocytes. J Physiol. 2004 Sep;559(3):777–98.

181. Chan FC, Cheng CP, Wu KH, Chen YC, Hsu CH, Gustafson-Wagner EA, et al. Intercalated Disc-Associated Protein, mXin-alpha, influences surface expression of ITO currents in ventricular myocytes. Front Biosci - Elit. 2011;3 E(4):1425–42.

182. Coppini R, Mazzoni L, Ferrantini C, Gentile F, Pioner JM, Laurino T, et al. Ranolazine prevents phenotype development in a mouse model of hypertrophic cardiomyopathy. Circ Hear Fail. 2017;10(3):1–17.

183. Ferrantini C, Coppini R, Scellini B, Ferrara C, Pioner JM, Mazzoni L, et al. R4496C RyR2 mutation impairs atrial and ventricular contractility. J Gen Physiol. 2016;147(1):39–52.

184. London B, Guo W, Pan XH, Lee JS, Shusterman V, Rocco CJ, et al. Targeted replacement of Kv1.5 in the mouse leads to loss of the 4-aminopyridine-sensitive component of IK,slow and resistance to drug-induced QT prolongation. Circ Res. 2001;88(9):940–6.

185. Saito T, Sato T, Miki T, Seino S, Nakaya H, Saito T, et al. Role of ATP-sensitive K channels in elec-trophysiological alterations during myocardial ischemia: a study using Kir6.2-null mic. Am J Physiol Hear Circ Physiol. 2005;288:352–7.

186. Lee A, Fakler B, Kaczmarek LK, Isom LL. More Than a Pore: Ion Channel Signaling Complexes. J Neurosci [Internet]. 2014 Nov 12 [cited 2023 Nov 14];34(46):15159–69. Available from: https://www.jneurosci.org/content/34/46/15159

187. Tapa S, Wang L, Francis Stuart SD, Wang Z, Jiang Y, Habecker BA, et al. Adrenergic supersensitivity and impaired neural control of cardiac electrophysiology following regional cardiac sympathetic nerve loss. Sci Reports 2020 101 [Internet]. 2020 Nov 2 [cited 2023 Nov 15];10(1):1–12. Available from: https://www.nature.com/articles/s41598-020-75903-y

188. Morotti S, Edwards AG, Mcculloch AD, Bers DM, Grandi E. A novel computational model of mouse myocyte electrophysiology to assess the synergy between Na+ loading and CaMKII. J Physiol [Internet]. 2014 Mar 15 [cited 2023 Nov 15];592(6):1181–97. Available from: https://onlinelibrary.wiley.com/doi/full/10.1113/jphysiol.2013.266676

189. Wemhöner K, Friedrich C, Stallmeyer B, Coffey AJ, Grace A, Zumhagen S, et al. Gain-of-function mutations in the calcium channel CACNA1C (Cav1.2) cause non-syndromic long-QT but not Timothy syndrome. J Mol Cell Cardiol [Internet]. 2015;80:186–95. Available from: http://dx.doi.org/10.1016/j.yjmcc.2015.01.002

190. Antoons G, Volders PGA, Stankovicova T, Bito V, Stengl M, Vos MA, et al. Window Ca2+ current and its modulation by Ca2+ release in hypertrophied cardiac myocytes from dogs with chronic atrioventricular block. J Physiol [Internet]. 2007 Feb 15 [cited 2023 Nov 15];579(1):147–60. Available from: https://onlinelibrary.wiley.com/doi/full/10.1113/jphysiol.2006.124222

191. Hennessey JA, Boczek NJ, Jiang YH, Miller JD, Patrick W, Pfeiffer R, et al. A CACNA1C Variant Associated with Reduced Voltage-Dependent Inactivation, Increased CaV1.2 Channel Window Current, and Arrhythmogenesis. PLoS One [Internet]. 2014 [cited 2023 Nov 15];9(9):e106982. Available from: https://journals.plos.org/plosone/article?id=10.1371/journal.pone.0106982

192. Song Z, Ko CY, Nivala M, Weiss JN, Qu Z. Calcium-Voltage Coupling in the Genesis of Early and Delayed Afterdepolarizations in Cardiac Myocytes. Biophys J. 2015 Apr 21;108(8):1908–21.

193. Vizgirda VM, Wahler GM, Sondgeroth KL, Ziolo MT, Schwertz DW. Mechanisms of sex differences in rat cardiac myocyte response to β-adrenergic stimulation. Am J Physiol - Hear Circ Physiol [Internet]. 2002 [cited 2022 Apr 8];282(1 51-1):256–63. Available from: https://journals.physiology.org/doi/full/10.1152/ajpheart.2002.282.1.H256

194. Xiao L, Zhang L, Han W, Wang Z, Nattel S. Sex-based transmural differences in cardiac repolarization and ionic-current properties in canine left ventricles. Am J Physiol - Hear Circ Physiol [Internet]. 2006 [cited 2022 Apr 8];291(2):570–80. Available from: https://journals.physiology.org/doi/full/10.1152/ajpheart.01288.2005

195. Johnson BD, Zheng W, Korach KS, Scheuer T, Catterall WA, Rubanyi GM. Increased Expression of the Cardiac L-type Calcium Channel in Estrogen Receptor–deficient

Mice. J Gen Physiol. 1997 Aug;110(2):135–40.

196. James AF, Choisy SCM, Hancox JC. Recent advances in understanding sex differences in cardiac repolarization. Prog Biophys Mol Biol [Internet]. 2007 Jul [cited 2022 Jul 1];94(3):265–319. Available from: https://pubmed.ncbi.nlm.nih.gov/15979693/

197. Yang PC, Clancy CE. In silico prediction of sex-based differences in human susceptibility to cardiac ventricular tachyarrhythmias. Front Physiol. 2012 Sep 14;3 SEP:33341.

198. Parks RJ, Howlett SE. Sex differences in mechanisms of cardiac excitation–contraction coupling. Pflügers Arch - Eur J Physiol 2013 4655 [Internet]. 2013 Feb 17 [cited 2023 Nov 15];465(5):747–63. Available from: https://link.springer.com/article/10.1007/s00424-013-1233-0

Acknowledgement

I extend my deepest gratitude to Prof. Dr. med. Nikolaj Klöcker, whose intellectual brilliance, invaluable guidance, and unwavering support were instrumental throughout this research journey. His keen insights and innovative ideas significantly shaped the course of this study.

I am indebted to Dr. Ehsan Amin, a mentor in the truest sense. His wealth of knowledge, kindness, and an easygoing yet focused approach created a conducive learning environment. I am thankful for the countless lessons and discussions that enriched my understanding and skills.

Special thanks to Dr. Andre Heinen for his expertise in performing the I/R procedure, and technical assistants, Julia Vedyashkin and Julia Gleich for their valuable contributions, alongside Stefan Schaetz and Thomas Becher for their technical support. A special appreciation goes to Esin Ongun, our secretary, for her vital role in keeping things organized and efficient. Your contributions were invaluable, and your dedication to the smooth functioning of our work did not go unnoticed.